Structure-property relationships in the search for superconductivity

by

Jessica R. Panella

A dissertation submitted to The Johns Hopkins University

in conformity with the requirements for the degree of

Doctor of Philosophy

Baltimore, Maryland

May, 2018

Abstract

Designing materials to fill a specific function or to have the requisite properties to test fundamental theory has been a consistent challenge in solid state chemistry and condensed matter physics. Material properties are almost always determined by the crystal structure, which imposes symmetry constraints on the bonding between atoms and determines the electronic and magnetic structure. Because of this, studying and understanding structure property relationships is crucial to the materials design process. The work presented in this dissertation investigates the structure, chemistry, and physical properties of oxyselenide compounds with a focus towards advancing the field of superconductivity.

In Chapter 2, the results of many targeted synthesis experiments are presented. The aim was to discover new superconducting materials using structural motifs common in superconductors as building blocks for a new material. The compounds, $Sr_2O_2Bi_2Se_3$, $Ba_2O_2Bi_2Se_3$, and $Sr_2O_2Sb_2Se_3$ discovered over the course of the project were shown to be quasi-one-dimensional analogues of bismuth sulfide superconductors. $Sr_2O_2Sb_2Se_3$ and $Ba_2O_2Bi_2Se_3$ show insulating resistivity behavior as a function of temperature. $Sr_2O_2Bi_2Se_3$ has more unique resistivity, sometimes showing a linear, decreasing resistivity with decreasing temperature,

and sometimes classic active transport behavior. This suggests that it lives on the border between insulator and metal, and that its electronic structure is strongly influence by composition, which changes from sample to sample due to the high vapor pressure of selenium.

Chapter 3 discusses the set-up of a diamond anvil cell and the work behind designing and assembling a magnetic susceptibility measurement system with a pair of solenoid coils capable of fitting inside the cell to measure the magnetic response of samples under pressure. The susceptibility instrument, BNK3R, uses a primary measurement coil set to apply a small magnetic field and detect the sample response in conjunction with a secondary, adjustable compensation coil set which cancels the inductive current generated by the applied field for a better signal-to-noise ratio. A pre-amplifier amplifies the nanovolt-scale signal by a factor of 1000 before the signal is filtered using a lock-in amplifier.

Susceptibility measurements on Pb using BNK3R at ambient pressure and under applied pressure demonstrated the capability of the system both to measure susceptibility and apply pressure. Subsequent measurements were performed on Tl_5Te_3 and $Sr_2O_2Bi_2Se_3$ using Pb as an internal manometer. Tl_5Te_3 showed a systematic decrease in T_C with increasing pressure, with the transition dropping below the lowest measurable temperature between P = 0.5 and 1 GPa. An unusual signal was observed in $Sr_2O_2Bi_2Se_3$ between P = 0.5 and 1.5 GPa, which requires further investigation.

Chapter 4 presents the method of seeded chemical vapor transport for growth of large, phase-pure single crystals of Cu_2OSeO_3. The seeded growth method was

shown to increase the mean size of the crystals by roughly a factor of two, in addition to improving quality and purity. The seed provided an ideal, stoichiometric nucleation site, which helped eliminate the deposition of off-stoichiometric material. The surface chemistry of Cu_2OSeO_3 was studied using the form of the crystals in comparison to a matched Wulff construction. Assuming that the growing crystal reached equilibrium before the growth was halted, the crystal form is a minimum surface energy conformation. Based on the form of the crystals and the location of the crystallographic planes in the unit cell, it was determined that breaking SeO_3 units likely raised the surface energy significantly, resulting in no representation of the closest-packed (1 1 1) face. Rather, the two lowest energy surfaces were the (1 1 0) and the (1 0 0), with the (1 1 0) substantially lower than the (1 0 0).

Thesis Committee

Primary Readers

Tyrel M. McQueen (Primary Advisor)
Professor
Department of Chemistry
Department of Physics and Astronomy
Department of Materials Science and Engineering
Johns Hopkins Kreiger School of Arts and Sciences

Kit Bowen
E. Emmett Reid Professor of Chemistry
Department of Chemistry
Johns Hopkins Kreiger School of Arts and Sciences

Harris Silverstone
Professor
Department of Chemistry
Johns Hopkins Kreiger School of Arts and Sciences

Acknowledgments

First, I would like to thank my advisor, Prof. Tyrel McQueen, who gave me the freedom to pursue my interests and was supportive of all of my efforts, even when the horizon seemed quite distant, and who took a personal interest in ensuring my future success. His teaching style produces independent, confident scientists, and my training as a doctoral student could not have been better.

I would also like to thank my fellow group members, with whom I have shared laughter and frustration in exactly the right proportion. In particular, thank you to Juan Chamorro for the many times we stared at the periodic table coming up with the craziest ideas (which Prof. McQueen usually let us try). Discussions of science and life with Thao Tran, Kate Arpino, and Zachary Kelly helped me develop as scientist and a person, which I greatly appreciate.

I owe special thanks to Kit Bowen for encouraging me to apply to Johns Hopkins University.

I am inexpressibly grateful to Zachary Hicks, who has provided endless support, encouragement, and fierce scientific discussion, and who made me laugh when I needed it most.

Finally, I would like to thank my dad for raising me to believe that I can do anything, and my mom for always being there.

Table of Contents

List of Tables

List of Figures

Chapter 1

Introduction

One of the most important aspects of any solid material is its ability to conduct electrical current. The highly conductive properties of metals make them ideal for transfer of energy and information through phone or power lines, while the high resistance of insulators makes them ideal to isolate conductive components to prevent undesired conduction to surrounding media. The intermediate resistance in semiconductors allows for tunable energy transfer, making transistor technology and solar conversion possible. There are numerous other technologies and fundamental phenomena that branch off of the three basic material categories, making electronic properties of solids one of the most well-researched areas of science.

While metals, semiconductors, and insulators span orders of magnitude in resistance, they all have finite resistance at all temperatures. A particularly interesting phenomenon arises in materials known as superconductors, which transition to the superconducting state below a critical temperature, T_C. In the superconducting state, they are able to pass current with zero resistance, allowing for potentially

lossless energy transfer over incredible distances. Interestingly, superconductors (SCs) belows T_C also exhibit perfect diamagnetism in what is known as the Meissner state, which has additional industrial applications, such as magnetic levitation. The limitation is that the superconducting state for most materials only exists at cryogenic temperatures. The highest recorded transition temperature (T_C) to date at ambient pressure is T_C = 133 K in $HgBa_2Ca_2Cu_3O_{8+\delta}$ and at T = 190 K under applied pressure of P = 150 GPa in H_2S [1, 2]. The need for cryogenic cooling puts severe limits on the commercial viability of superconductors for wide consumer use in electronics.

The search for new superconducting materials is hampered by the poor understanding of the material requirements to give rise to superconductivity. Phenomenological theories propose a phonon-mediated mechanism that drives the formation of superconducting pairs of electrons, but fail to link the mechanism to structural properties, and fall short of explaining the behavior of more recent high T_C SCs. However, many known superconductors share common structural motifs, guiding research towards materials with similar structures to known SCs. The use of structure to guide to discovery was the foundation for the work presented herein.

1.1 Superconductivity

Superconductors are frequently characterized by their magnetic response under applied magnetic fields, **H**, which can be used to categorize all SCs as either Type I or Type II. The two common measurements are temperature-dependent magnetic

susceptibility ($\chi(T)$) and field-dependent magnetization (M(H)). At the critical temperature under very small fields, all SCs enter the Meissner state, where the magnetic susceptibility drops to -$1/4\pi$ (which is dimensionless in SI units, but commonly is given the label "emu" for "electromagnetic units"), shown in Figure 1.1 (a). The expulsion of magnetic field from the inside of the sample is often referred to as perfect diamagnetism, due to the similarity to the field-repulsion response of a traditional diamagnet, but the origin of the response in an SC differs from that of a diamagnet. In SCs, effect arises as a result of eddy currents generated on the surface of the material.

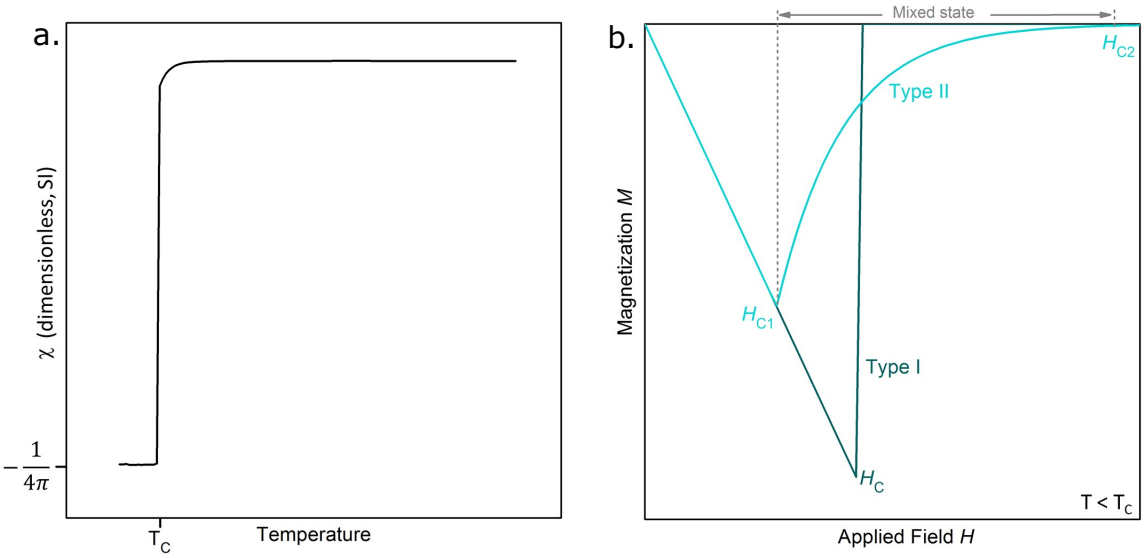

Figure 1.1: A simple example of adding more 1*s* orbitals to an MO diagram which begins to resemble a band structure for large numbers of orbitals.

At increasing field strengths, the response differs between Type I and Type II. Type I SCs above a certain critical field (H_C), magnetic field lines penetrate through the entire sample and bulk superconductivity is lost with the return to the

normal state. Type II SCs have two critical fields, H_{C1} and H_{C2}. Above H_{C1}, Type II SCs enter a state characterized by partial, quantized penetration of magnetic field lines in very narrow rods, called the mixed state (see Figure **??** (b)). The regions of field penetration represent a distinct, non-superconducting phase that is phase separated from the superconducting bulk material. The biphasic mixture of superconducting and non-superconducting regions persists up to a second critical field, H_{C2}, where the superconducting phase is entirely quenched [3].

This is fundamentally different from the classification of SCs as either conventional or unconventional, which are labels for materials that are or are not well described by the Bardeen-Cooper-Schrieffer (BCS) theory, discussed in Section 1.2 [3, 4]. Many unconventional SCs are also Type II, which leads to some colloquial mixing of the terms that obscures the true distinction. The BCS theory is based on the idea that under certain conditions, conduction electrons couple to lattice vibrations, resulting in a net *attractive* interaction between them, forming a bound pair of electrons called a Cooper pair.

1.2 Phonon-mediated electron interactions

In 1957, a theory proposed by John Bardeen, Leon Cooper, and John Schrieffer explained the observed physical properties of conventional superconductors [5]. The theory relies on the coupling of electron motion to lattice vibrations (phonons) in a metallic lattice. The starting point for BCS theory is summaraized below.

A crystal lattice can be approximated as a lattice of positive nuclei located on

equilibrium positions, and that the net background potential in between nuclei is neutral due to shielding provided by core and localized valence electrons, while conduction electrons are mobile, negative charges [6]. The neutral background potential only holds while nuclei maintain equilibrium positions. Displacement off of the equilibrium position changes the charge distribution of the lattice in that area and resulting in a δ^+ charge some distance away from the displaced nucleus. Displacement of the nucleus is common, as thermal energy always results in phonons.

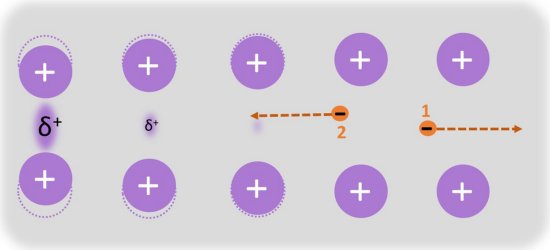

Figure 1.2: A diagram showing how a conduction electron (orange) pulling on the nuclei (purple) can generate local positive charge density which can interact with another electron. Electron 1 caused a lattice distortion, leaving a trail of positive charge in its wake. Electron 2, moving the opposite direction feels the effect of that positive charge. Under certain conditions the net interaction is attractive.

As a conduction electron moves through the lattice, it pulls on the positive nuclei it passes through Coulombic attraction, and the force of the attraction pulls each nucleus off site, generating a phonon and a local δ^+ charge. However, electrons are so much lighter and faster than heavy nuclei that the lattice response is delayed. By the time the δ^+ charge manifests above the equilibrium potential, the electron that caused the distortion has moved a significant distance from the site. Other conduction electrons in the vicinity feel the attraction to the δ^+

charge and repulsion from the initial electron simultaneously. This results in a net effective interaction potential, V_{eff} that is the sum of the phonon-mediated electron interaction (V_{el-ph}) and the Coulombic (photon-mediated) interaction (V_{Coul}) [3]. The phonon-mediated potential is given by

$$V_{el-ph} = \frac{2|M_{\mathbf{q}}|^2 \omega_{\mathbf{q}}}{\omega^2 - \omega_{\mathbf{q}}^2} \tag{1.1}$$

where $\mathbf{q}$ is the momentum transferred between two electrons via phonon creation and absorption, ω is the energy transfer term, $M_{\mathbf{q}}$ is the phonon-electron coupling matrix [3]. The Coulomb interaction (in terms of momentum rather than position) takes the form

$$V_{el-el} = \frac{1}{4\pi\epsilon_0} \frac{2\pi e^2}{q^2} \tag{1.2}$$

where e is the fundamental charge, ϵ_0 is the electric permittivity of free space, and q is the electron momentum.

The presence of frequency terms reflects the time-dependence of the phonon-mediated interaction. If the second electron is too fast, the first electron has not moved far enough away. If the second electron is too slow, then the δ^+ charge will begin to decay. For values of $\omega < \omega_{\mathbf{q}}$, the phonon term, V_{el-ph} is negative. If $\omega \lesssim \omega_{\mathbf{q}}$, the phonon term will be large and negative. In this case, $|-V_{el-ph}| >> V_{el-el}$ and V_{eff} is becomes asymptotically negative as ω approaches $\omega_{\mathbf{q}}$ from below, shown in the graph of V_eff in Figure 1.3. This results in a net attractive potential between the two electrons, and they form a bound Cooper pair.

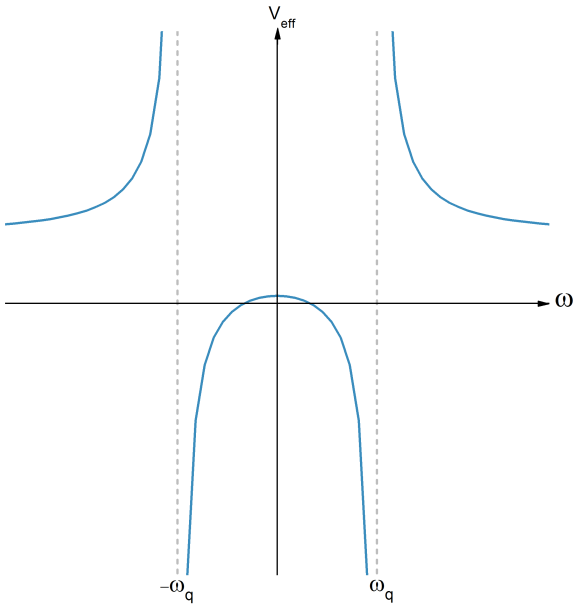

Figure 1.3: A graph of the total effective potential as a function of ω. At absolute values just slightly smaller than $|\omega_q|$, the potential is asymptotically negative.

This mechanism was the basis for BCS theory, which has shown good experimental agreement with many conventional superconductors [4]. However, unconventional SCs are not well-described by BCS theory. Phonon-electron coupling matrix $|M_{\mathbf{q}}|$ is weak, and it is possible a different, stronger type of coupling mechanism underlies unconventional superconductivity [3, 4]. However, since there is no solid theory for what material components are necessary to give rise to superconductivity, either in conventional or unconventional SCs, the search for new SCs is slow and largely serendipitous.

Many SCs seem to share similar structural motifs, namely two-dimensional structures where the layers alternate between those that contain orbitals with conduction electrons and those with filled, insulating orbitals, such as in the iron

arsenide, cuprate, and the bismuth sulfide SCs [4]. This similarity motivates exploration of superconductors from a structure-property relationship standpoint. One strategy is to investigate materials with structures resembling those of known SCs by subjecting them to high pressure or other external stimulus. Another strategy is to make new structural analogues in the hopes for finding superconductivity in a new material.

1.3 Crystal structures and x-ray diffraction

The structure of materials guides almost all of their physical properties, and an understanding of crystal structures is crucial to furthering the field of superconductivity and solid state chemistry in general. X-ray diffraction is often an essential first pass analysis tool, as x-rays can be generated in a laboratory setting without a specialized facility. Additionally, the x-ray wavelength of about 0.1 Å is optimal for studying crystal lattices since it is on the order of interatomic spacing.

The heart of x-ray diffraction relies on the Bragg condition for constructive interference [7].

$$n\lambda = 2d\sin\theta \tag{1.3}$$

A crystal structure can be described entirely by the unit cell combined, which is the smallest unit that repeats in three-dimensional space and contains all of the point symmetry elements that exist within the lattice, combined with translational symmetry operations. The unit cell has characteristic cell parameters that define its

shape and volume, the length of each edge and the angle between them. The three edge lengths are referred to as a, b, and c in real space, and h, k, and l in reciprocal space, where h = 1/a, k = 1/b, and l = 1/c. Crystallographic planes are denoted using the reciprocal space Miller indices [h k l]. Bragg's law expressed in reciprocal space relates directly to the Miller index notation

$$\vec{k'} - \vec{k} = H_{hkl} \tag{1.4}$$

Where $H_{hkl} = 1/d_{hkl}$, $\vec{k}$ is the wave vector for the incident photon, and $\vec{k'}$ is the wavevector for the scattered wave [7].

Analysis of the crystal structure relies on understanding both the angular position of the reflections and the intensity of the reflections. Structural symmetry determines the actual pattern, while the atomic number of diffracting elements determines the intensity. The effect of symmetry can be illustrated in 2D by examining the lattice planes in a square lattice versus a rectangular lattice. In a square lattice, the [1 0] and [0 1] have equal interplanar distances, so the diffraction peaks express at the same angle, while in a rectangular lattice, the breaking of four-fold rotational symmetry causes those planes to diffract at independent angles.

The diffraction intensity goes as the square of the structure factor, F_{hkl}

$$F_{hkl} = \sum_n f_n e^{2\pi i(hx_n + ky_n + lz_n)} \tag{1.5}$$

where f_n is the atomic form factor, and x_n, y_n, and z_n are fractional coordinates within the unit cell [7]. The atomic form factor is related proportionally to the

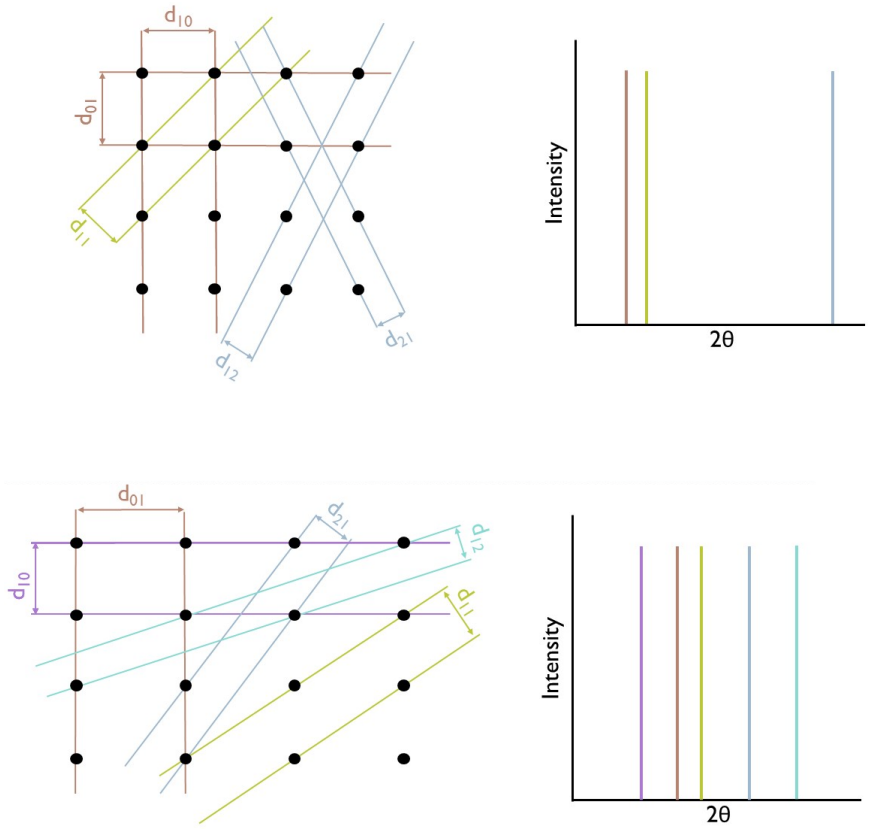

Figure 1.4: A diffraction pattern for a cubic square net (a) and a rectangular square net (b) demonstrating the change in pattern from the breaking for a four-fold rotational axis.

atomic number of the element, and decreases in magnitude as a function of angle [7]. The presence of centering operations force the structure factor to zero, resulting in systematic absences in the diffraction pattern [7]. All of these features can be used to distinguish or determine a crystal structure based solely on its diffraction signature.

1.4 Band Structure

A band structure diagram (BS) relates electron energy to the orbital bonding environment it occupies for an extended structure, the way that a molecular orbital (MO) diagram carries the same information for a single molecule. Figure 1.5 shows simple σ_s-only MO diagrams for cylindrical molecular rings containing 2, 4, 6, and many atoms. For increasing numbers of atoms, the MO energy levels become increasingly closely spaced. Even a gram of an extended solid contains roughly 10^{26} atoms, each with many orbitals. The spacing between orbitals becomes so small that it is negligible compared to thermal energy even as temperature approaches absolute zero, forming a veritable continuum of states that are best described by bands rather than individual MOs [8].

The wavefunction describing each electronic state can be given as a linear combination of atomic orbitals sitting on each lattice site, distance a apart.

$$\Psi_k = \sum_n e^{ikna} X_n \tag{1.6}$$

where X_n is the atomic orbital wavefunction for atom n, and k is the wavenumber which relates to the symmetry of wavefunction, the number of nodes, and is inversely proportional to the wavelength ($k = 2\pi/\lambda$) [8]. The periodicity of the lattice imposes boundary conditions on the wavefunction carried by the e^{ikna} term, so that the only unique solutions are for values of $|k| \leq \pi/a$. Plugging two end

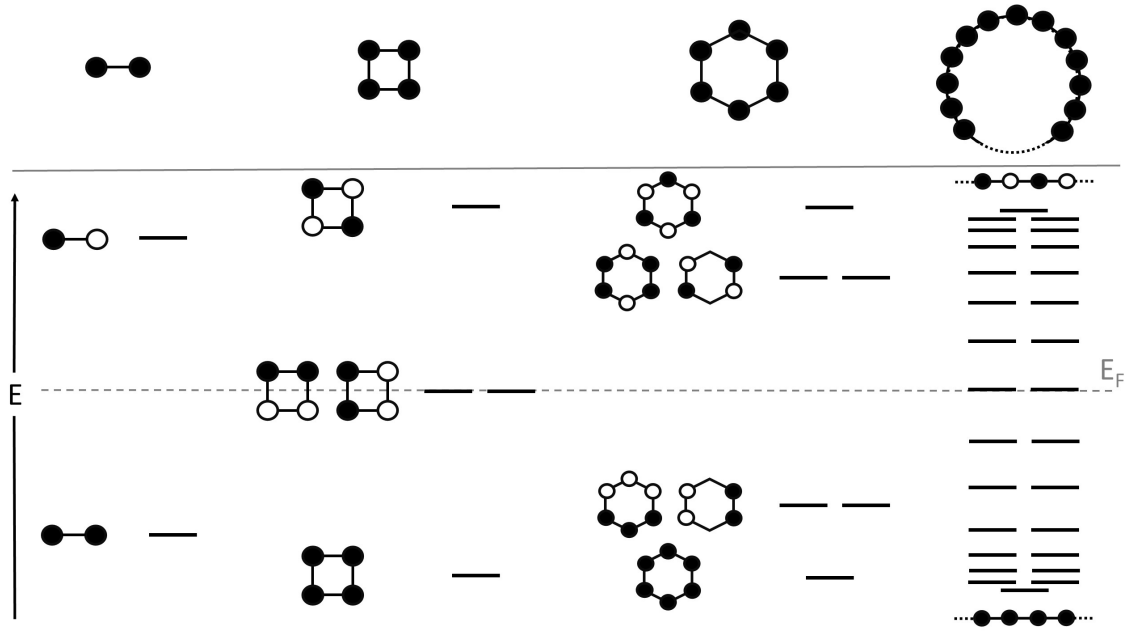

Figure 1.5: A simple example of adding more 1*s* orbitals to an MO diagram which begins to resemble a band structure for large numbers of orbitals.

members, $k = 0$ and $k = \pi/a$, into Equation 1.6 gives the following two solutions

$$\Psi_{k=0} = \sum_n X_n \tag{1.7}$$

$$\Psi_{k=\pi/a} = \sum_n (-1)^n X_n \tag{1.8}$$

For σ_s orbitals, $k = 0$ represents the most bonding-type interactions, where the wavefunction between sites does not change sign and the adjacent orbitals are of the same parity, which is the lowest energy state. The other end member, $k = \pi/a$, has the wavefunction changing sign and the orbitals changing parity at every lattice site, which yields the most antibonding-type interactions and the

highest energy state [8]. The states formed by σ_s interactions increase in energy from $k = 0$ to $k = \pi/a$ with the highest density of states closest to the end points, as shown in 1.6.

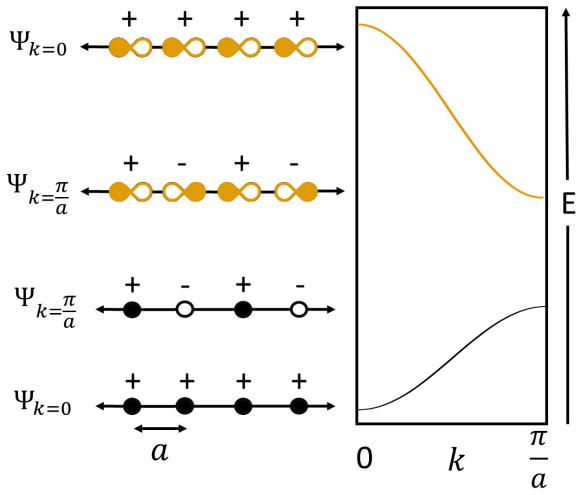

Figure 1.6: An example of how the atomic orbital affects the energy dispersion of the derived band in k-space.

The σ interactions between p-orbitals differ from the s-orbitals due to the node at the center of the p-orbitals. As shown in Figure 1.6, the $k = 0$ state has the most antibonding character, where even though the wavefunction has the same sign between sites, the adjacent orbital lobes are of opposite parity. This results in the $k = 0$ state having the highest energy and the $k = \pi/a$ state having the lowest energy, such that bands derived from σ_p interactions run the opposite direction of those derived from σ_s interactions.

The number of electrons filling the states is determined by the atoms involved in bonding. At absolute zero, the electrons are assumed to be in the lowest possible energy level still observing Pauli exclusion, called the Fermi level. At finite

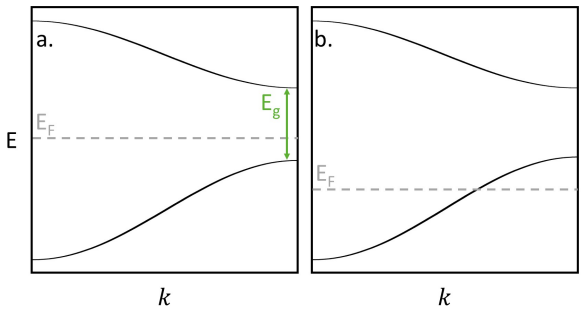

Figure 1.7: A simple example of changing the Fermi level relative to the valence band to induce metallicity in a band insulator with band gap E_g. An insulating band structure with the Fermi level located within the band gap shown in (a) and a metallic band structure with the Fermi level located within a band shown in (b).

temperature, where thermal energy has some probability of exciting electrons higher energy states, the distribution of occupied states can be shifted to energies higher than the Fermi energy if there are available states within that temperature range. Materials where the Fermi level lies within a band are metallic, since there are unoccupied states available for electrons to move into, allowing the mobility required for conduction. Insulators have a Fermi level that lies in a gap between bands, Figure 1.7 **a**, where the gap energy (E_g) is large relative to thermal energy, so there are no unoccupied states available to allow conduction. Insulator to metal transitions (and vice versa) can be induced by changing the electronic state or band structure to change the position of the bands relative to the Fermi level. A simple way to achieve this is by doping with electrons (moving the Fermi level up) or holes (moving the Fermi level down), as shown for holes in Figure 1.7 **b**.

In an MO diagram, the difference in energy between the bonding and antibonding molecular orbitals is small for weakly interacting atomic orbitals and large for strongly interacting orbitals. Similarly, strongly interacting atomic orbitals

in an extended structure give rise to a large energy dispersion in the band as a function of k. The band dispersion can be tuned by increasing the interaction strength between interacting orbitals, either chemically (by changing the elements) or by changing the lattice constant, shown in Figure 1.8. Chemical or mechanical pressure can be used to adjust the lattice constant while maintaining the same bonding environment. Chemical pressure involves either stuffing in a large atom into the structure either in a natural cavity between atoms or by substituting for a smaller atom with a similar electronic structure (i.e. a 4d metal for a 3d metal). This principle can be used to induce metallicity, or even superconductivity, in otherwise insulating materials.

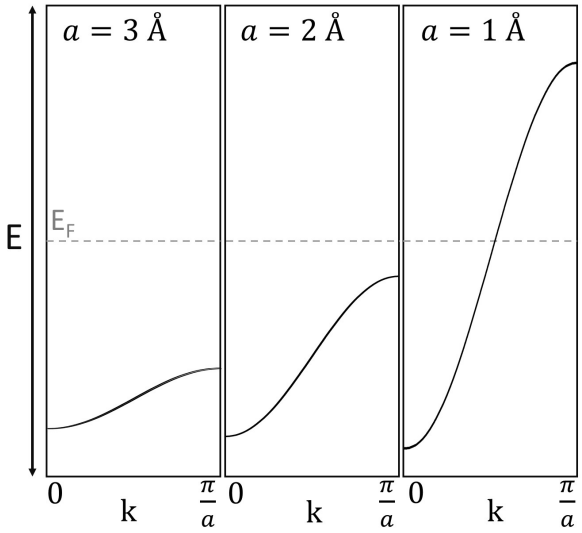

Figure 1.8: A schematic example of how band dispersion changes as a function of interatomic distance as a consequence of orbital overlap.

A calculated band structure combined with measured physical properties can often be instrumental in tying together structure property relationships towards understanding the physics of the material.

1.5 Physical properties characterization

1.5.1 Electronic transport

Measurement of electrical resistivity as a function of temperature ($\rho(T)$)is a convenient way to determine whether a material is an insulator, semiconductor, metal, or superconductor, as each broad class generally displays signature behavior, with exceptions.

Metallic $\rho(T)$ is usually linear starting at room temperature and decreasing in resistance down to the tens of Kelvin range, where it levels off to a flat T-independent region. Conductivity (σ), the inverse of resistivity, is given by

$$\sigma = ne^2\tau/m \tag{1.9}$$

Where n is the number of electrons, e is the charge, τ is the mean time between collisions, and m is the electron mass. The form of conductivity explains the trend observed in resistivity. The temperature trend is determined by τ, since the other terms are constant with temperature. At room temperature, electron-phonon collisions dominate. As temperature decreases, phonon modes depopulate as the thermal energy necessary to cause lattice vibrations vanishes. At low temperatures, when phonon modes have been almost entirely depopulated, conductivity is dominated by collisions of electrons with lattice defects. The onset of the T-independent region of metallic resistivity is directly related to the purity of the material.

Since superconductors are a special type of metal, they display a similar trend

in $\rho(T)$, with the important distinction that their resistivity drops to zero at T_C. While it is not possible to measure zero resistance directly, since the measurement electronics themselves are resistive, the sudden and dramatic drop in resistivity, particularly in conventional SCs, is telling in itself.

In semiconductors and insulators, the form of resistivity reflects the presence of a band gap. Electrons in the valence band are not mobile, so in order to conduct electricity, they must be excited to the conduction band, which requires the input of energy from an external source. The resistance of a gapped material increases exponentially with the size of the gap, as expected from statistical thermodynamics. At higher temperatures, the distribution of electrons with enough energy to overcome the band gap energy increases, resulting in higher conductivity at higher temperatures. Temperature-dependent resistivity in systems with largely non-interacting electrons takes the form of an Arrhenius-like activated transport model

$$\rho(T) = \rho_0 e^{-E_g/2k_BT} \tag{1.10}$$

Where ρ_0 is ideally the infinite temperature resistance, E_g is the band gap, and k_B is the Boltzmann constant. Practically, taking ρ_0 to be the resistance at the highest measured temperature is sufficient.

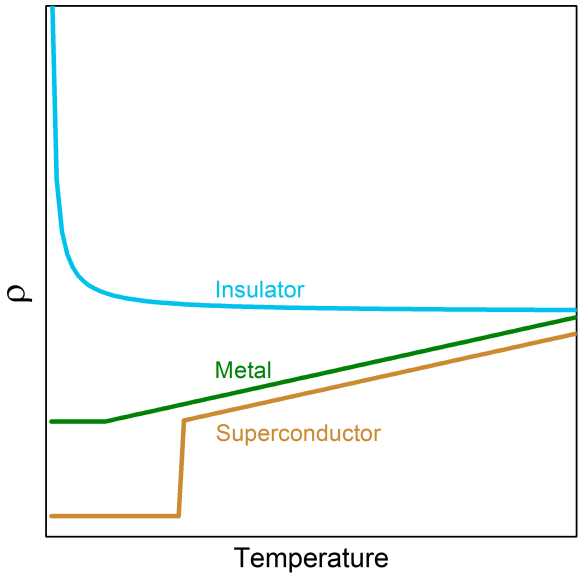

Figure 1.9: General form of resistance versus temperature behavior for gapped material, metal, and superconductor.

1.5.2 Magnetic susceptibility

The magnetic properties as a function of temperature reveal information about the number of unpaired electrons and the type of magnetic interactions present. In materials with unpaired electrons, the spin of each electron represents a small magnetic moment that can interact with the moments of nearby electrons to lower the overall energy of the system. There are four classical types of magnetism that materials typically show, diamagnetism, paramagnetism, antiferromagnetism, and ferromagnetism.

Magnetization is measured by applying a magnetic field to the sample and measuring the response of the sample. This can be done with either an AC or DC

magnetic field. An AC measurement directly probes the differential susceptibility

$$\chi = \partial \mathbf{M} / \partial \mathbf{H} \tag{1.11}$$

Whereas a DC measurement probes the static magnetization. Details of measuring magnetic susceptibility are discussed in depth in Chapter 3. The underlying physical state of the material and general features are discussed below.

Ferromagnetism and antiferromagnetism are both forms of magnetic ordering that exist below a material-dependent ordering temperature. In a ferromagnetic material, unpaired spins on adjacent sites align with each other. Ferromagnets typically have a large magnetization resulting from a large, position χ. Antiferromagnets have spins that counter align with each other and oppose an applied field. The net susceptibility is small and positive, with deviations from ideal alignment resulting in a positive contribution to the overall susceptibility. Above their ordering temperature, the spins in ferro- and antiferromagnetic materials are disordered and point at random directions due to thermal excitations. The disordered spins loosely align with an applied $\mathbf{H}$ due to a small, positive χ in the paramagnetic state [9].

Materials with no unpaired electrons exhibit diamagnetism. As an external field is applied, the paired electrons in filled shells counter the applied field very weakly, resulting in a very small, negative susceptibility. All materials have some diamagnetic contribution to their overall susceptibility due to core electrons. In some diamagnetic materials, edge states and lattice defects can result in a small

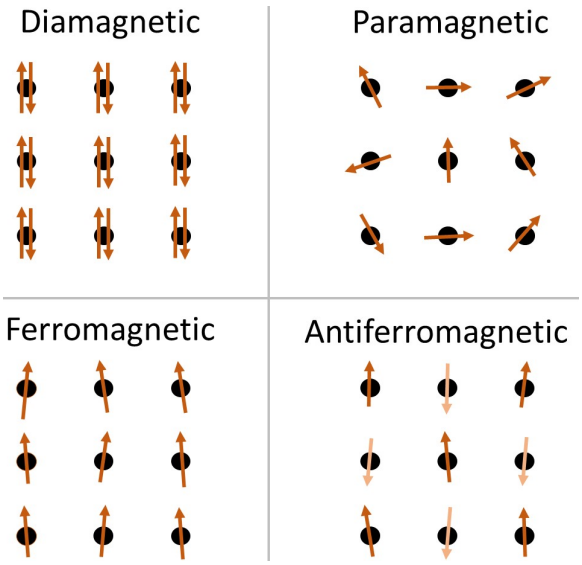

Figure 1.10: Graphic representation of the alignment of spins for a few common types of magnetic ordering

type	sign	magnitude (emu)
paramagnetism	+	10^{-3}–10^{-2}
ferromagnetism	+	~1–3
antiferromagnetism	+	10^{-4}
diamagnetism	-	10^{-6}–10^{-5}
superconductivity	-	$=\frac{1}{4\pi}$

Table 1.1: Magnetic susceptibility scales for different ordering types [10].

percentage of unpaired electrons, so that diamagnetic materials will also show behavior associated with paramagnetism, called Pauli paramagnetism. Superconductors below their transition temperature have a large, negative χ and are considered to be perfect diamagnets because their magnetization exactly cancels the applied field such that χ = -1, though the mechanism of their diamagnetism differs from simply having no unpaired electrons, as discussed in Section 3.1. The scale of χ for different types of magnetic ordering is shown in Table 1.1 [9].

1.5.3 Heat capacity

The temperature-dependent heat capacity can be used to look for subtle phase transitions that can be hard to see in other measurements. Analysis of heat capacity yields information about the lattice energy stored as vibrational modes, i.e. phonons, and energy stored in magnetic or electronic excitations. Heat capacity is usually measured under constant pressure conditions, but at low temperatures the constant pressure (C_P) and constant volume (C_V) heat capacities are approximately the same, because the isothermal expansion approaches zero with decreasing temperature [11].

Empirical fits to heat capacity data often take advantage of both the Einstein and Debye models for heat capacity, which each account for lattice vibrations differently. The Einstein model is purely quantum mechanical, and assumes that each atom vibrates independently of its neighbor. The model fits the high temperature portion of the data well, because it accounts for higher energy optical phonons which are excited at higher temperatures and have a wavelength on the scale of the interatomic distance. The form of C_V in the Einstein model is

$$C_V = 3Rs\frac{x_E^2 e^{x_E}}{(e^{x_E}-1)^2} \tag{1.12}$$

where s is the number of atoms, x_E is given by $(\hbar\omega_E)/(k_B T)$, and ω_E is the average frequency of the oscillating atoms. Since the Einstein model assumes independent oscillations, it describes some structural features very well. For example, atoms that sit in structural cavities and are loosely interacting through

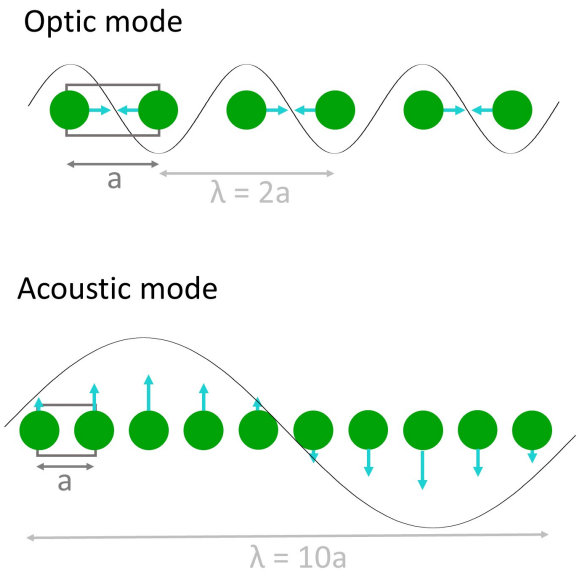

Figure 1.11: An example of each an optic and acoustic phonon mode in a 1D chain of atoms with interatomic spacing a. The unit cell is shown as a grey box.

van der Waals forces, or, as discussed later, atoms containing lone pairs that cause local oscillations along the axis of the lone pair[12].

However, the long range interactions of solids are best described by the Debye model, which is particularly well suited to the low temperature region. The Debye model assumes correlated motion of atoms, with vibrations that span the length of the material [11]. The wavelength of these phonons can be much longer than the average interatomic spacing, and are generally lower energy than optic phonons. The Debye model of heat capacity gives

$$C_V = 9Rs(T/\theta_D)\int_0^{x_D} \frac{x^4 e^x}{(e^x-1)^2} \tag{1.13}$$

where $\theta_D = \hbar\omega_E/k_B$, x is θ_D/T, and ω_D is the average frequency of the acoustic

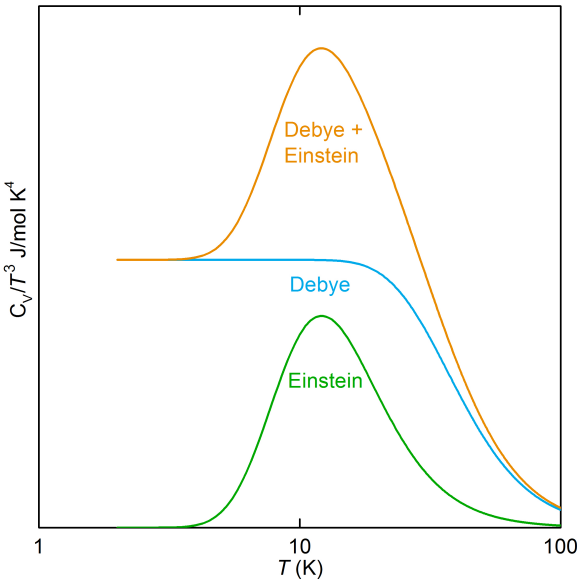

Figure 1.12: An example graph showing the general shape of Einstein and Debye modes in C_V/T^3 data versus temperature plotted on a log scale.

phonons.

The forms of the Debye and Einstein specific heat are very similar to one another when plotted as C_V versus T. The difference can be seen more dramatically in a plot of C_V/T^3, where an Einstein mode will appear as a large, broad feature overlaid on the Debye specific heat, which is approximately flat at low temperatures, shown in Figure 1.12 [11].

The presence of an Einstein mode can often be attributed to structural features, such as electron lone pairs or polyatomic cations that occupy large cavities in the lattice and have their own self-contained vibrational modes. Any electronic or free spin contribution to heat capacity, such as in a metal or paramagnet, is independent of temperature, and would dominate at low temperature when plotted as C/T^3

[11]. The information extracted from heat capacity data fit with a simple model can be used in support of other measurement techniques to demonstrate that the observed properties are representative of the bulk, rather than a result of the measurement technique, surface phases, or similar extrinsic effect.

Powder x-ray diffraction, resistivity, magnetization, and heat capacity measurements, combined with calculated band structure and chemical intuition form the basic toolbox for studying structure-property relationships.

References

[1] G. F. Sun, K. W. Wong, B. R. Xu, Y. Xin, and D. F. Lu. "Tc enhancement of $HgBa_2Ca_2Cu_3O_{8+\delta}$ by Tl substitution". In: *Physics Letters A* 192.1 (1994), pp. 122–124. ISSN: 0375-9601. DOI: 10.1016/0375-9601(94)91026-X.

[2] A. P. Drozdov, M. I. Eremets, and I. A. Troyan. "Conventional superconductivity at 190 K at high pressures". In: *arXiv:1412.0460 [cond-mat]* (2014).

[3] Kristian Fossheim and Asle Sudbo. *Superconductivity: Physics and Applications*. Wiley, 2005. ISBN: 978-0-470-84452-6.

[4] Roland Hott, Reinhold Kleiner, Thomas Wolf, and Gertrud Zwicknagl. "Review on Superconducting Materials". In: *arXiv:1306.0429 [cond-mat]* (2013).

[5] J. Bardeen, L. N. Cooper, and J. R. Schrieffer. "Theory of Superconductivity". In: *Phys. Rev.* 108.5 (1957), pp. 1175–1204. DOI: 10.1103/PhysRev.108.1175.

[6] Leon N. Cooper. "Bound Electron Pairs in a Degenerate Fermi Gas". In: *Phys. Rev.* 104.4 (1956), pp. 1189–1190. DOI: 10.1103/PhysRev.104.1189.

[7] B. E. Warren. *X-Ray Diffraction*. English. Reprint edition. New York: Dover Publications, 1990. ISBN: 978-0-486-66317-3.

[8] Roald Hoffman. *Solids and Surfaces: A Chemist's View of Bonding in Extended Structures*. PN, 1988.

[9] Neil Ashcroft and N. David Mermin. *Solid State Physics*. en. ISBN: 978-0-03-083993-1.

[10] "Magnetic Susceptibility of the Elements and Inorganic Compounds". In: *CRC Handbook of Chemistry and Physics (Internet Version)*. Ed. by John R. Rumble. 98th ed. Boca Raton, FL: CRC Press/Taylor & Francis, 2018.

[11] A Tari. *The Specific Heat of Matter at Low Temperatures*. en. Imperial College Press, 2003. ISBN: 978-1-86094-314-0 978-1-86094-939-5.

[12] Brent C. Melot, Ronald Tackett, Jim O'Brien, Andrew L. Hector, Gavin Lawes, Ram Seshadri, and Arthur P. Ramirez. "Large Low Temperature Specific Heat in Pyrochlore $Bi_2Ti_2O_7$". In: *Phys. Rev. B* 79.22 (2009). ISSN: 1098-0121, 1550-235X. DOI: 10.1103/PhysRevB.79.224111.

Chapter 2

Exploratory synthesis in the search for new superconductors

This chapter presents the results of two different synthetic approaches to the discovery of new materials with the ultimate goal of elucidating the structural and electronic components necessary for superconductivity. The goal of the first project was to manipulate electronic energy levels using strong-field ligands to attain Co^{2+}- or Ni^{3+}-based analogue to cuprate SCs. The second project sought to combine structural elements of the FeAs-based SCs with the BiS_2-based SCs. Both projects revealed interesting challenges of high temperature synthesis.

2.1 Searching for Co-based SC: Background and Motivation

The idea of electron-lattice coupling combined with the prevalence of layered structures formed the basis for the work discussed in this section. As mentioned in Chapter 1, the BCS theory for superconductivity relies on electrons forming

Cooper pairs through a net attractive, phonon-mediated interaction [1, 2]. In order to disrupt the conduction of one member of the Cooper pair, both must be disrupted, requiring a significant input of energy. Most collision events do not have the required energy, so lattice defects, which provide resistance in most materials, are not sufficient. However, since the pairing is formed through the phonon interactions, it can be disrupted with a phonon on the same energy scale. Even at very low temperatures, there are still phonons with the required energy to break the Cooper pair, pushing T_C down to cryogenic temperatures. The motivation behind the Co/CN^- project discussed in this chapter was to target a stronger lattice-coupling mechanism based on Jahn-Teller (J-T) distortion such that a higher energy phonon (and consequently higher temperature) is required to break the Cooper pair.

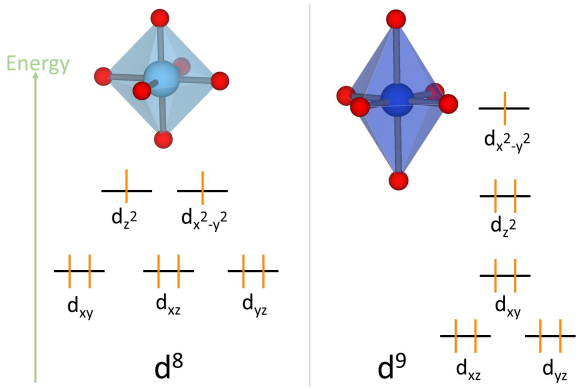

Figure 2.1: J-T distortion figure captions

J-T distortion is an effect most strongly observed in octahedral Cu^{2+} d^9 complexes, where the energy degeneracy of the two e_g orbitals with unequal occupancy is broken by elongating the octahedron along z-axis. In an extended structure

with a mixture of Cu^{2+} and Cu^{3+}, an electron conducting through the lattice will change the oxidation state of adjacent sites as it moves. This will cause a transition from ideal octahedral coordination in Cu^{3+} to an elongated octahedron in Cu^{2+}. The movement of the apical ligands is pronounced and can affect nearby atoms to propagate a phonon. The phonon may couple to another electron just as in the Coulombic-driven BCS theory, but through a much stronger mechanism, which is robust against thermal disruption up to much higher temperatures.

The highest T_C SCs currently known (at ambient pressure) are the family of copper oxide based (cuprate) SCs, of which one of the most widely studied is $La_{1-x}Sr_xCuO_4$ (LSCO). The structure of LSCO consists of planes of corner-sharing CuO_6 octahedra separated by gaps between the planes containing (La,Sr) ions. In this structure, the conduction electrons originate from Cu d-orbitals [2], and more specifically from $d_{x^2-y^2}$. In this structure, the $d_{x^2-y^2}$ orbital points directly at the bridging oxygens between two metal centers, putting the mobile electrons on a convenient conduction path from Cu to O to the next Cu. Each layer is isolated from adjacent layers, eliminating interference due to magnetic interactions between Cu atoms, which could break the cooper pairs or result in localization of the electrons.

There are many known Cu SCs, and the goal of this research project was to demonstrate that the J-T distortion combined with the convenient conduction path in a layered material are the special ingredients that give rise to the high temperature, unconventional superconductivity in the cuprates. The idea was to use Co^{2+} or Ni^{3+}, which are both d^7, in place of Cu to demonstrate the universality of this effect. J-T distortion in a d^7 system results in the single unpaired electron

sitting in the d_{z^2} orbital, which points towards the apical ligand, which in these layered materials does not bridge to the next metal center. This is a problem that may be addressed by manipulating the orbital energies through ligand substitution so that d_{z^2} is higher in energy than $d_{x^2-y^2}$.

2.2 Cyanide-based Substitution Reactions

Two different routes were investigated for making a J-T distorted Co compound with the right orbital splitting: (1) substitution of CN^- for Br^- in $Sr_2CoO_2Br_2$ via solid state reaction with KCN/NaCN and (2) reduction of $(La/Pr)_4Ni_{3-x}Co_xO_{10}$ using H_2 gas or solvothermally with NaH followed by subsequent oxidation with $(CN)_2$ gas. Ligand field theory predicts that a strong-field ligand like CN^- should form stronger bonds than a weak-field Br^-, increasing the energy of the anti-bonding d_{z^2} orbital with which the apical ligand strongly overlaps. The synthetic approaches are summarized in Tables 2.1 and 2.2.

The reduction of $La_4Ni_3O_{10}$ to $La_4Ni_3O_9$ and $La_4Ni_3O_8$ by a few methods has been reported in the literature [3], however the synthesis methods for making $La_4Ni_3O_{10}$ reported in the literature relied either on extremely high reaction temperatures, very long reaction times, or toxic reagents [4–7]. The two methods detailed below are based closely on the literature methods, but avoided toxic reagents and extremely high temperatures (T > 1100 °C), and shortened the reaction times to about one day. It should be noted that since the ultimate fate of $La_4Ni_3O_{10}$ was to be reduced, the oxygen stoichiometry was not critical, and products produced by these methods may be oxygen-deficient.

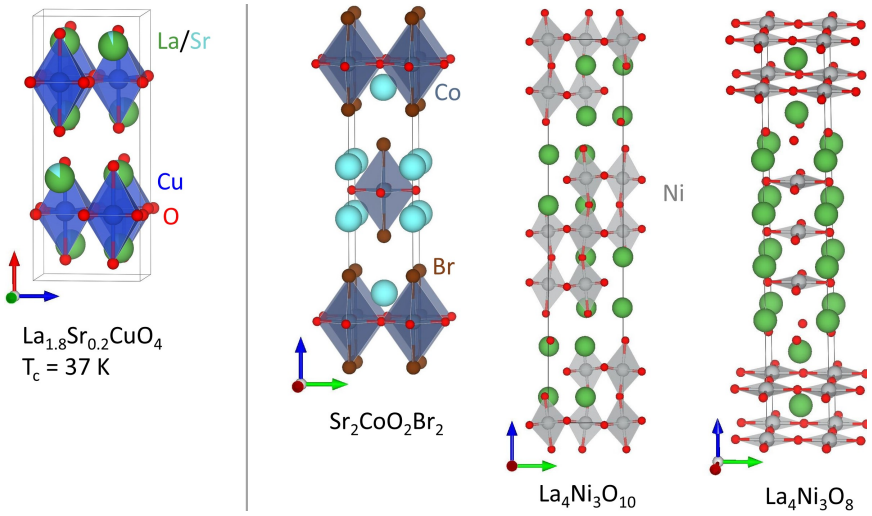

Figure 2.2: structures like LSCO

2.2.1 Modified citric acid method

The citric acid method in general is well-known [8], and is based on forming organic citrate linking units between the reactant species in solution, then burning off the organic linker at high temperatures, which collapses the network and brings the reactant species in for reaction. The advantage is that if citric acid is used in excess, the reactant species are essentially single atoms or molecules separated by citric acid linkers, and after burning off the organics, the single atoms react directly, circumventing the diffusion barrier.

La_2O_3 was dried at 1000 °C overnight, and weighed along with $NiCl_2(H_2O)_6$ in stoichiometric amounts, then dissolved in 3 M nitric acid. A large (10x) mass excess of citric acid was added to the solution. The solution was poured into a 20 mL alumina crucible and heated at 90 °C in a furnace for 1 hr to prevent boiling over, then heated at 450 °C for 4 hrs. The resultant crusty solid was ground, pressed

into a pellet, and sintered at 1100 °C for about 24 hrs.

2.2.2 Modified precursor method

The precursor method for synthesizing $La_4Ni_3O_{10}$ is based on that of Zhang and Greenblatt [5], but with the key substituion of NaOH for the toxic base tetramethylammonium hydroxide. La_2O_3 was dried at 1000 °C over night, then weighed along with $NiCl_2(H_2O)_6$ in stoichiometric ratio. The mixture was dissolved in 3 M HNO_3 and stirred. Using $NiCl_2(H_2O)_6$ instead of NiO greatly aided with dissolution so that boiling the nitric acid was not necessary. To this solution, 3 M NaOH was added dropwise until the precipitate remained and pH 11. The precipitate was too fine for standard filtration with either a frit or filter paper, so the mixture was centrifuged and the basic solution decanted. Water was added, the mixture centrifuged, and liquid decanted again, and this process was repeated until the pH tested neutral. The wet solid was placed in a boat crucible, and heated at 350 °C for four hours, then ground, pelletized, and fired at 1100 °C in air for 12 hrs with a ramp rate of 110 °C/hr. The product was pure by PXRD after one heating. For synthesis of $La_4Co_3O_{10}$ and $La_4Ni_{3-x}Co_xO_{10}$, the same method was used but with flowing N_2 during the 1100 °C firing step.

2.2.3 Reduction and CN-oxidation of $La_4Ni_3O_8$

$La_4Ni_3O_{10}$ can be reduced to either $La_4Ni_3O_9$ or $La_4Ni_3O_8$, depending on how reducing the synthesis environment is. $La_4Ni_3O_{10}$ cannot be reduced to $La_4Ni_3O_8$ using only a 5% H_2 mixture without significant measures to prevent even the

Target	Reactants	Conditions	Result
$Sr_2CoO_2Br_2$	SrO, CoO, $SrBr_2$	sealed tube, in crucible, 615°C, 12 hrs	$Sr_2CoO_2Br_2$, requires two heatings
$La_4Ni_{3-x}Co_xO_{10}$	$La(NO_3)_3$, $NiCl_2(H_2O)_6$, $CoCl_3(H_2O)_6$	Precursor method	$La_4Ni_{3-x}Co_xO_{10}$
$La_4Ni_3O_8$	$La_4Ni_3O_{10}$, 10x excess NaH	solvothermal in anhydrous pentane 200 °C [3]	$La_4Ni_3O_8$
$La_4Ni_3O_8$	$La_4Ni_3O_{10}$	under flowing 5% H_2, balance Ar at 325 °C, cooled quickly	$La_4Ni_3O_9$
$Pr_4Ni_3O_{10}$	Pr_6O_{11}, $Ni(NO_3)_2$	dissolved in 50% HNO_3, burned at 450 °C in air, then annealed at 1000°C under flowing O_2	$Pr_4Ni_3O_{10}$
$Pr_4Ni_3O_8$	$Pr_4Ni_3O_{10}$	under flowing 5% H_2, balance Ar at 325 °C	$Pr_4Ni_3O_8$
$(CN)_2$	NaCN, $CuSO_4$ (dry)	Sealed tube, 300°C	Na_2SO_4, CuCN, $(CN)_2$

Table 2.1: Table summarizing synthesis of the precursor materials used for subsequent ion exchange reactions.

smallest amount of oxygen contamination, which leaves an environment that is only reducing enough to form $La_4Ni_3O_9$. $La_4Ni_3O_9$ is air stable, containing only Ni^{2+}, while $La_4Ni_3O_8$ is extremely oxygen-sensitive due to the unstable mixture of Ni^{1+} and Ni^{2+}. The oxygen-sensitivity of $La_4Ni_3O_8$ makes it appealing for these reactions, because it should be very susceptible to reaction with the mild oxidant $(CN)_2$. However, work with $La_4Ni_3O_8$ is complicated by the fact that even the smallest air exposure will oxidize it in a way that is not measurable with PXRD but has a clear effect on M(T) measurements. It is possible that air exposure oxidizes the surface to form a non-reactive passivation layer of $La_4Ni_3O_9$, which is too thin or disordered to be seen with PXRD, but changes the magnetic response and prevents further oxidation with $(CN)_2$.

Oxidation of $La_4Ni_3O_8$ using cyanogen gas was carried out by *in situ* cyanogen generation and by flowing a 1% $(CN)_2$ in balance N_2 mixture over the reduced material. The *in situ* method was set up as in Figure 2.3. The crucibles containing reactants were both made out of quartz to allow viewing of reaction progress. The crucibles were either kept together for the same reaction temperature, or separated by a neck in the tube to allow some independent control of the reaction temperatures. Reactions were done with the tube upright in a box furnace, and the top opening of the furnace was used to achieve lower temperatures by placing the top of the tube, containing the $La_4Ni_3O_8$ crucible, just inside of the opening with the cyanogen reaction materials in the furnace center.

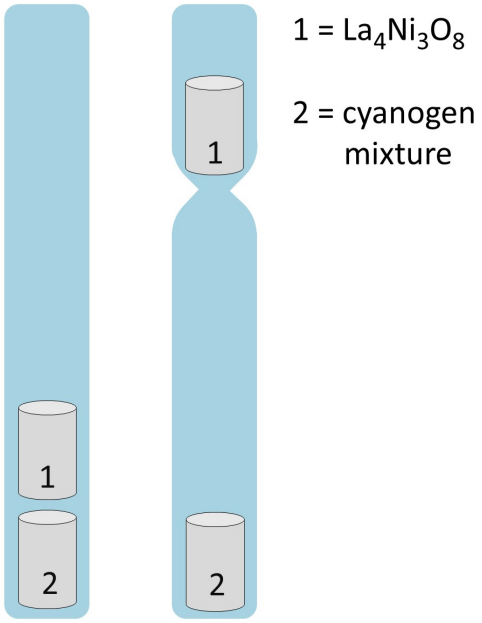

Figure 2.3: Reaction set up for *in situ* cyanogen generation and oxidation

Cyanogen gas was generated by the following two reactions:

$$FeCl_3 + CuCN \rightarrow FeCl_2 + CuCl + (CN)_2 \tag{2.1}$$

$$CuSO_4 + 2NaCN \rightarrow Cu(CN)_2 + Na_2SO_4$$

$$Cu(CN)_2 \rightarrow CuCN + \frac{1}{2}(CN)_2 \tag{2.2}$$

Interestingly, $Pr_4Ni_3O_{10}$ is reported to reduce straight to $Pr_4Ni_3O_8$ in one step, without the formation of $Pr_4Ni_3O_9$ and $Pr_4Ni_3O_8$ is purportedly air stable. The stability in air likely stems from the fact that it is metallic, so electrons are shared,

Target	Reactants	Conditions	Result
$La_4Ni_3O_8(CN)_2$	$La_4Ni_3O_8$ from solvothermal, *in situ* $(CN)_2$	300°C, sealed tube (Fig. 2.3)	products of NaH side reaction, some La438 phases, maybe target material
$La_4Ni_3O_8(CN)_2$	$La_4Ni_3O_8$, $(CN)_2$ from tank	300°C	products from NaH side reaction
$Pr_4Ni_3O_8(CN)_x$	$Pr_4Ni_3O_8$, $(CN)_2$ from tank	300°C	70% $Pr_4Ni_3O_8$, 30% possible target material

Table 2.2: Summary of reaction conditions and results for reaction of $(CN)_2$ gas with $La_4Ni_3O_8$ and $Pr_4Ni_3O_8$.

and Pr has more flexible oxidation states than La. Reduction in a 5% H_2 mixture in balance argon seemed to confirm this according to PXRD of the product. However, for the entire family of compounds, the difference in PXRD pattern is subtle, as they all maintain tetragonal symmetry. Reaction of $Pr_4Ni_3O_8$ with pure $(CN)_2$ gas from a 1% mixture in balance nitrogen showed promising results. The PXRD pattern showed some peaks resembling the $Pr_4Ni_3O_{10}$ structure, but others were absent, as shown in Figure 2.4. The pattern clearly shows some unreacted $Pr_4Ni_3O_8$, but the cluster of three peaks at $30° < 2\theta < 35°$ as opposed to two well-separated peaks suggests a second phase growing in. While the middle peak could simple be more $Pr_4Ni_3O_{10}$, the absence of the prominent $Pr_4Ni_3O_{10}$ peaks at $2\theta = 47.5°$ and 23° suggests that this phase is not simply the unmodified parent.

Attempts to make $Sr_2CoO_2(CN)_2$ resulted in the decomposition of $Sr_2CoO_2Br_2$ into CoO, KBr, and SrNCN, and presumably amorphous carbon which cannot be seen in PXRD patterns. The starting cyanide salt KCN is stable up to at least its melting point of 630 °C, but the sample decomposed even at synthesis temperatures as low as 300 °C, determined via PXRD, Figure 2.5. The presence of SrNCN

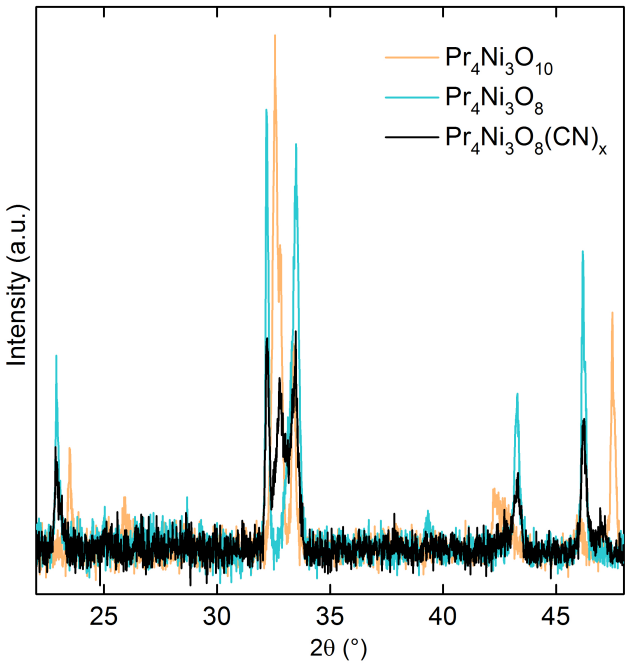

Figure 2.4: The PXRD pattern of $Pr_4Ni_3O_{10}$ parent phase in light orange, $Pr_4Ni_3O_8$ in light blue, and reaction product in black. There are extra peaks in the product pattern in addition to peaks corresponding to $Pr_4Ni_3O_8$, though the additional peaks do not seem to be $Pr_4Ni_3O_{10}$.

and decomposition at such low temperatures implies that the KCN reacted with $Sr_2CoO_2Br_2$ prior to its decomposition. The subsequent decomposition can be explained in terms of π-backbonding, as Co^{2+} has electrons capable of filling $\pi*$-antibonding orbitals of CN, destabilizing the C-N triple bond.

The difficulty in replacing oxygen with cyanide raises interesting chemical questions. From a simple crystal field splitting persepective, a strong-field ligand should be able to replace a weak-field ligand under the right synthetic conditions fairly easily, due to the energetic gain advantage of forming strong covalent bonds. It is possible that the change in structure required to accommodate a dramatic

Sample ID	Conditions	Product
110-1	615°C	KBr, SrO, amorphous other
110-1-1		KBr, SrO, amorphous other
110-2	400°C, 16 hrs	KBr, SrO, some $Sr_2CoO_2Br_2$
110-3	400°C, 72 hrs	KBr, SrO, some $Sr_2CoO_2Br_2$, sm. amt. SrNCN, sm. amt. $SrCO_3$
110-4	350°C, 16 hrs	$Sr_2CoO_2Br_2$, SrO, KBr, KCN, v. sm. amt. $SrCO_3$, SrNCN, Sr_4OBr_6
110-4-1	350°C, 24 hrs, reheat of 110-4	$Sr_2CoO_2Br_2$, SrO, KBr, KCN, $SrCO_3$, SrNCN, Sr_4OBr_6
110-5	300°C, 16 hrs	$Sr_2CoO_2Br_2$, SrO, KBr and KCN (1:5), SrNCN, Sr_4OBr_6, $rBr_2(H_2O)_6$
110-5-1	300°C, 72 hrs, reheat of 110-5	$Sr_2CoO_2Br_2$, SrO, KBr and KCN (1:3), SrNCN, sm. amt. $SrCO_3$, Sr_4OBr_6, $rBr_2(H_2O)_6$
110-5-2	330°C, 16 hrs, reheat of 110-5-1	$Sr_2CoO_2Br_2$, SrO, KBr and KCN (1:1), SrNCN, $SrCO_3$, Sr_4OBr_6, $rBr_2(H_2O)_6$
110-6	330°C, 16 hrs	$Sr_2CoO_2Br_2$, SrO, KBr and KCN (1:1), $SrCO_3$, SrNCN, $SrBr_2(H_2O)_6$
110-6-1	330°C, 16 hrs, reheat of 110-6	$Sr_2CoO_2Br_2$, SrO, KBr and KCN (1:1), $SrCO_3$, SrNCN, $SrBr_2(H_2O)_6$

Table 2.3: The most prominent identifiable products are listed. Products that showed up in only small amounts are denoted by "sm. amt" and very is expressed as "v.". In cases where the products did not represent all of the elements in the starting materials, decomposition into amorphous products is assumed. Co is generally under-represented, likely due to its fluorescence under Cu K_α radiation preventing strong diffraction.

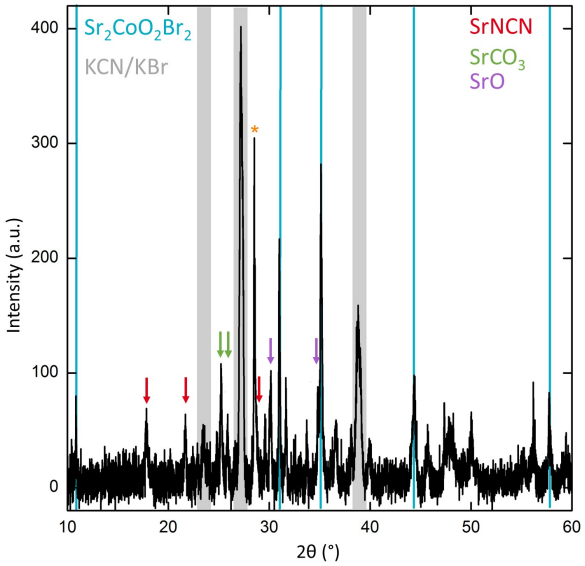

Figure 2.5: PXRD pattern of sample 110-4-1, showing the presence of SrNCN (red arrows), SrO (purple arrows), and $SrCO_3$ (green arrows). KBr and KCN have nearly the same lattice parameters, and overlap as broad peaks highlighted by grey bars. The parent phase $Sr_2CoO_2Br_2$ is still present, as noted by blue lines.

change in crystal field splitting presents a high energetic barrier to the formation of the product, which is not achievable through low-temperature solid-gas interface reactions. High temperature solid state reactions were shown to result in decomposition. This leaves solution-based chemistry as the most likely route to success.

Other experiments run alongside the cyanide-based substitution reactions, which sought to expand phase diagram of BiS_2-based superconductors, did turn up some interesting compounds. The background of those experiments was based on observation of structural motifs in iron arsenides and bismuth sulfides. Both families consist of layered structures, but the iron arsenides have more variety in structure than the bismuth sulfides. Attempting to synthesize new bismuth

selenides based on the structures of known sulfides and iron arsenides revealed three previously undiscovered compounds, which were shown to be 1D-analogues of BiS_2 superconductors, as described in the section to follow.

2.3 Motivation for BiS_2-based Exploration

In layered SCs, the structure can be divided into superconducting layers and non-superconducting blocking layers. Superconductivity is a 3D phenomenon, so the whole structure exhibits superconductivity. The distinction is that the SC layers contain the orbitals from which the superconducting electrons originate, and the blocking layers act as charge reservoirs [2]. Systematic change in blocking layer thickness has been correlated with change in Tc within a family SCs.

The family of FeAs-based SCs exhibit three different blocking layer motifs. One of those is also observed in the BiS_2-based superconductors, but compounds containing the other motifs have not been synthesized. This was used as the basis for exploratory synthesis to discover new BiS_2-based superconductors with different blocking layer motifs, in the hopes that a trend would shed light on the role of the blocking layer in superconductivity. Se was used instead of S due to the complications with S forming sulfur oxides by side reaction with other starting materials, and Se can often be substituted for Se without deleterious effects on the chemistry.

All reactions produced the same major phase (largest phase fraction based on PXRD peak intensities) with an assortment of minor phases according to the actual

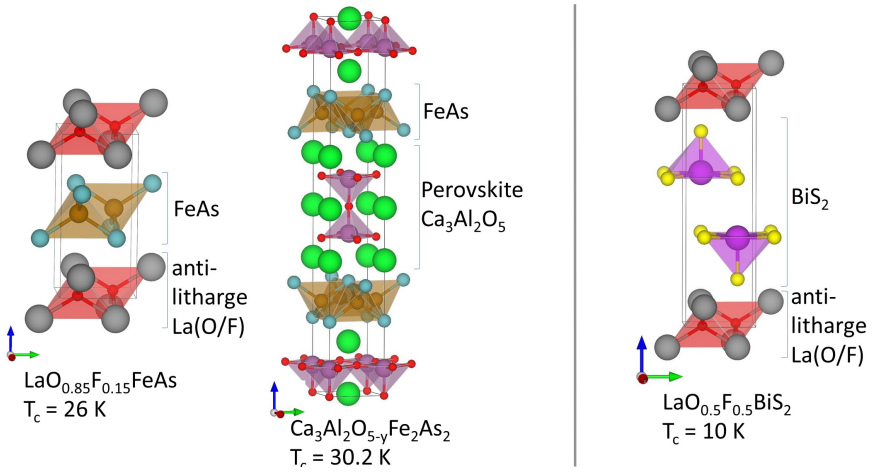

Figure 2.6: Model FeAs- and BiS_2-based superconductor structures

target stoichiometry. The main phase did not match any pattern in the diffraction database, which sparked interest. A quick magnetic susceptibility test for superconductivity determined that this material was not an SC, but the color suggested a small band gap semiconductor. This was promising given that the elements involved, namely Bi and Se, were present in many compounds with interesting physical properties, such as topological surface states and superconductivity. To understand the new material and plan further investigation, it was necessary to determine the actual composition and then solve the crystal structure from PXRD data.

All of reaction contained CoSe as an impurity, with the amount directly proportional to the amount of Co starting materials. This indicated that Co was not incorporated into the main phase, leaving just for elements to work with. It was assumed that Sr would remain bound to O, leaving a tertiary phase diagram of SrO, Bi, and Se to explore instead of a quarternary phase diagram, which is much

more complicated. A series of reactions with different ratios of SrO:Bi:Se were run in parallel under the same conditions as the original reaction, and phase purity was checked with PXRD. The formula for the new material was determined to be $Sr_2O_2Bi_2Se_3$.

With the formula in hand, Bruker TOPAS software was used to determine the structure from a PXRD pattern of the pure material. This was done in two steps: (1) determining the unit cell using the indexing function and (2) determining the atomic coordinates using simulated annealing.

The unit cell indexing function in TOPAS ignores peak intensity (and as a result, atoms), and only compares peak locations to the peak locations that are allowed by the space groups in the broad symmetry class chosen for indexing (i.e. monoclinic, body-centered tetragonal, etc). Using the data as a reference, the program will generate an output that consists of a wide range of unit cells that all produce a pattern that matches the data. It is important to note that the absence of a peak in the data where one is predicted to be from the model unit cell does not preclude that unit cell. Absence of a peak could result from a number of other effects, including poor incident intensity on the sample or preferred orientation of powder particles.

The output invariably contains many unrealistic unit cells, because the only considerations taken by the program are mathematical, not physical. It is left to the scientist to discern which of the many cells are feasible. For this material, a good starting point was to examine the unit cell volume of SrO and Bi_2Se_3 separately, then add those unit cell volumes in the right ratio (2:1 SrO:Bi_2Se_3) to get an estimate

Species	Formula Units/Cell	Cell Volume (Å^3)	Volume/Formula Unit (Å^3)
SrO	4	137.51	34.38
Bi_2Se_3	3	423.82	141.27
4SrO + 2Bi_2Se_3	2	420.06	210.03
$Sr_2O_2Bi_2Se_3$ (predicted)	2	437.98	218.99

Table 2.4: change predicted cell volume to actual predicted cell volume....

of the cell volume for $Sr_2O_2Bi_2Se_3$, with appropriate adjustments for the number of formula units per cell. Unit cells with lattice parameters of 3 Åor less were immediately excluded, as that is shorter than a typical Bi-O or Bi-Se bond (and also rare in general).

The output cells are plotted as goodness of fit versus cell volume. A monoclinic cell with a volume of about 440 Å^3 had a goodness of fit that was about two orders of magnitude better than any other cell. This volume compared well to the rough approximation using SrO and Bi_2Se_3 formula unit volumes, which is shown in 2.4. Refinement of the cell parameters put the statistical parameter R_{wp} well within the range of a feasible unit cell. R_{wp} is a compares the difference in calculated intensity to the observed intensity, as shown in equation 2.3.

$$R_{wp} = \sqrt{\frac{\sum w_m (Y_{o,m} - Y_{c,m})^2}{\sum w_m Y_{o,m}^2}} \tag{2.3}$$

Where $Y_{o,m}$ is the observed data at point m, $Y_{c,m}$ is the calculated data at point m, and w_m is a weighting factor which takes into account the error in observed intensity at m.

After refining the cell lattice parameters and instrument parameters to get

the best possible statistics, simulated annealing was used to determine atomic coordinates for the larger atoms, Bi, Sr, and Se. Oxygen was not included in simulated annealing, because its contribution to the overall intensity was so small compared to the other elements since intensity is proportional to the square of the atomic number (Z_O^2 = 64, Z_{Bi}^2 = 6889).

Simulated annealing (SA) works by throwing atoms into the unit cell and calculating diffraction intensity for that arbitrary configuration of atoms, then allowing them to "walk" into positions with the motion guided by fit statistics and preserving the symmetry of the lattice. Once they have walked into a minimum in R_{wp}, they will be scattered to new arbitrary positions and the process begins again, shown graphically as a plot of R_{wp} versus iteration in figure 2.7. This method will produce many local minima in R_{wp}, depending on the number of iterations set in the input file, and the output is a set of adjusted atomic positions that correspond to the lowest minimum calculated by the software for all iterations.

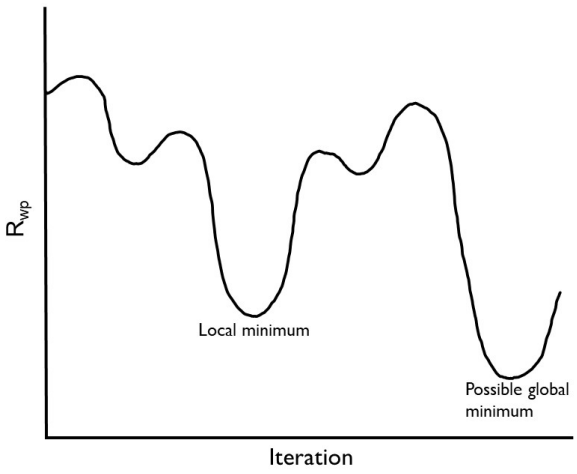

Figure 2.7: Simulated annealing graphic

As with unit cell indexing, this method does not take into account physics or chemistry at all. Some constraints can be added manual, such as minimum interatomic distances to avoid collisions, but it is also possible for the user to simply observed the (commonly unphysical) structural output and determine a realistic configuration that produces the same result. For example, the SA algorithm may increase the diffraction intensity in a particular plane by piling up multiple Se atoms to get the right electron density. Seeing this, the scientist can replace the pile of Se atoms with a single Bi atom. Upon re-running the SA input, the walk will begin with more electron density on that site. This will guide the refinement towards a more realistic result by changing its starting point on the R_{wp} versus atomic position curve.

Once the output structure began to show reasonable bond lengths and a recognizable coordination, the atomic positions were adjusted to be on the nearest Wyckhoff position with a multiplicity that gives the correct ratio of elements to reproduce the chemical formula. The structure was imported into TOPAS for full Rietveld refinement, still excluding oxygen. Rietveld refinement adjusts lattice parameters, atomic coordinates, and certain variable instrument parameters simultaneously to better match the calculated pattern to the experimental.

After refining the calculated pattern, the input file was adjusted to output a Fourier difference map. The difference map contains the same information as that included in the difference curve, which comes from subtracting the intensity of the calculated fit from the intensity of the data. Where the fit has excess intensity, the difference curve will have a troph, and where the fit underfits the pattern, the

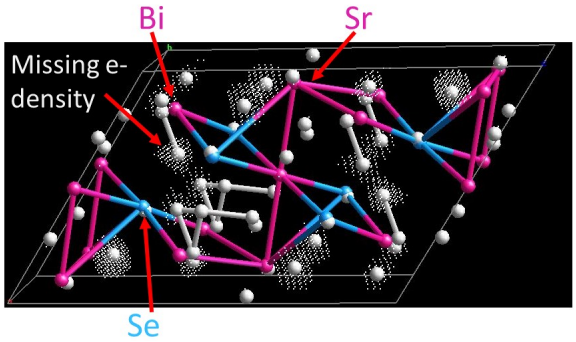

Figure 2.8: Fourier difference map of $Sr_2O_2Bi_2Se_3$ refinement using only Sr, Bi, and Se. The cations, Bi and Sr, are shown in pink, the anion Se in blue, and regions of the pattern that are electron-rich compared to the model are shown as white spheres at the center of white density clouds.

difference curve will have a peak. The peaks and trophs correspond to excess electron density and missing electron density, respectively, in the structural model. The Fourier difference map plots the electron density from the model and the difference curve in 3D according to the symmetry of the model, allowing for visualization of where the model diverges from the data.

The Fourier difference map of $Sr_2O_2Bi_2Se_3$ after refinement of lattice parameters and atomic positions for Sr, Bi, and Se without oxygen. White clouds correspond to regions of excess electron density that is not fit by the model, and white spheres are the suggested atomic positions according to the electron density. The white spheres and clouds in the vicinity of Sr were taken to be likely oxygen positions, on the basis of stoichiometry, size, related crystal structures, and the oxophilicity of Sr. Rietveld refinement of the crystal structure including oxygen improved the quality of the fit, and the oxygen position refined to a reasonable location near Sr. Attempts to add and refine oxygen position in other locations in the cell resulted

in oxygen collapsing onto another atom. The white spheres that overlap with Se likely result from Se vacancies in the structure, which would present as electron deficiency in the pattern.

Concurrent searches for compounds with the same general formula containing similar elements (other alkaline earths, chalcogenides) produced two additional compounds: $Ba_2O_2Bi_2Se_3$ and $Sr_2O_2Sb_2Se_3$. The PXRD patterns showed $Ba_2O_2Bi_2Se_3$ and $Sr_2O_2Sb_2Se_3$ to have the same structure as $Sr_2O_2Bi_2Se_3$ and the structure parameters were extracted through Rietveld refinement. Essential to the study of structure-property relationships is, naturally, the characterization of physical properties. While none of the three new compounds showed signs of superconductivity, their properties showed them to be small band gap semiconductors with, at least in the case of $Sr_2O_2Bi_2Se_3$, tunable band gaps, making them potentially useful in photovoltaics.

2.4 Physical Properties of $Sr_2O_2Bi_2Se_3$

Physical properties of the series of $A_2O_2B_2Se_3$ compounds were reported in Chemistry of Materials, but $Sr_2O_2Bi_2Se_3$ in particular showed dramatically different resistance behavior from sample to sample, which was worthy of further investigation [9]. Doping as a result of the high solid state synthesis temperature is expected in selenides, given the high vapor pressure of Se. Interestingly, some samples displayed an R(T) trend that was metallic in nature, linearly decreasing with decreasing temperature, but with a relatively high resistance.

Label	Sample Name	Date Collected	Synthesis Conditions
28-1	JP3-28-1-1	01/13/2015	75C/h to 800, dwell 40 hrs (Synth A), pellet cleaned, ground and sintered at 800 24 hrs after 75C/h ramp (Sinter A), surface shaved
28-2	JP3-28-1-1	01/13/2015	reran measurement
28-3	JP3-28-1-1	01/21/2015	Synth A, Sinter A, surface shaved
28-4	JP3-28-1-1	01/22/2015	Same pellet, leads scraped off and re-attached
38-1	JP3-38-1	01/30/2015	100C/h to 800, dwell 40 hrs, Sinter A, surface shaved, cut to rectangle
38-2	JP3-38-1	02/02/2015	same pellet, rerun to double check
60	JP3-60At	06/12/2015	Synth A, sample divided in two (t and b), both Sinter A
77-1	JP3-77SP	08/15/2015	Synth A, Sinter A, surface shaved
77-2	JP3-77SP	08/15/2015	restarted measurement
77-3	JP3-77SP	08/20/2015	restarted measurement
77-4	JP3-77SP	08/20/2015	reattached leads
77-5	JP3-77SP	08/21/2015	restarted measurement
85-1	JP3-85SP	09/13/2015	Synth A, Sinter A
85-2	JP3-85SP	09/14/2015	reran measurement
104	JP3-104A	12/20/2015	Synth A, Sinter A

Table 2.5: $Sr_2O_2Bi_2Se_3$ samples used for resistance measurements shown in Figure 2.9. Experimental conditions and measurement preparation steps are listed for each sample. Resistance is plotted on a log scale to allow comparison between the different samples, which cover a wide range of resistances.

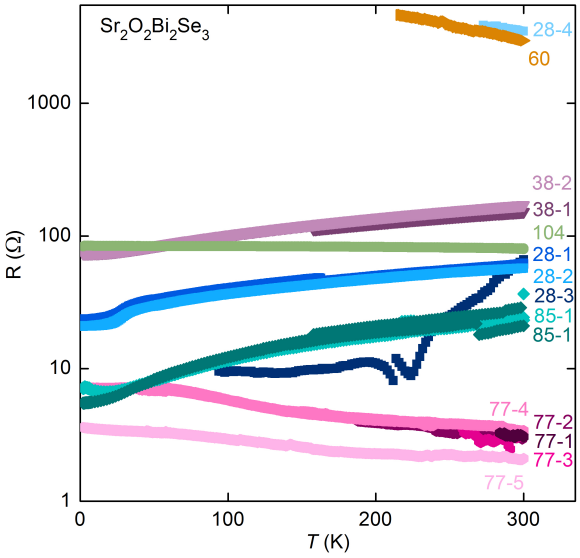

Figure 2.9: Temperature-dependent resistance for a variety of $Sr_2O_2Bi_2Se_3$ samples, some of which were measured multiple times. The sample labels are described more in table 2.5

As shown in Figure 2.9, some of the samples, such as JP3-38-1 and JP3-28-1-1 showed metallic character in their R(T). Early samples may have been more heavily doped, since the synthesis procedure had not been optimized, however JP3-85 also shows a metallic trend even though it succeeded the insulating JP3-77. Interestingly, JP3-77 shows insulating behavior, but has the lowest overall resistance of all of the samples. Since all of the samples are sintered pellets, they have a significant temperature-independent contribution to resistance from grain boundary scattering. Differences in magnitude may come from small details of the synthesis (such as how long it took the furnace to cool) which may change the particle size and the size of the grains. Additionally, the structure of $Sr_2O_2Bi_2Se_3$ almost causes anisotropic behavior, which could mean that more metallic-samples have a different orientation of crystallites due to the pressure used when pressing

the pellet (or other extrinsic factor).

Resistance measurements on crystals would allow for measurement along the direction of the bismuth oxiselenide chains (in the *b* direction) and perpendicular to the chains (along *a* or *c*) to determine if the resistance is truly anisotropic. The band gap calculated from the samples displaying insulating behavior is only about 0.1 eV.

Since the bismuth sulfide superconductors require doping, typically with fluorine, fluorine doping of $Sr_2O_2Bi_2Se_3$ was attempted using a small amount of PTFE tape sealed in the reaction tube, which should release reactive fluorides upon decomposition at elevated temperatures. This only resulted in decomposition of $Sr_2O_2Bi_2Se_3$ without noticeable change in lattice parameters of the remaining material. Similarly, attempts at sulfur doping resulted in the appearance of impurities without a change in the $Sr_2O_2Bi_2Se_3$ structure, even with doping levels as small as 5%. Substitution of Pb for Bi failed due to the formation of PbSe with no incorporation into the parent structure. Finally, other syntheses were tried to target compounds with the same stoichiometry using elements that adopt the same coordination environment, generally without success, though $Sr_2O_2Sb_2S_3$ showed promise and fine-tuning of the reaction conditions may yield another compound. Details of these doping attempts and synthesis of related materials can be found in Samantha Donaldson's lab notebook.

Resistivity data collected on $Ba_2O_2Bi_2Se_3$ and $Sr_2O_2Sb_2Se_3$ showed them both to be insulating for all measured samples. The absolute resistance varied between

samples, likely also due to Se vaporization, but there was no observed insulator-to-metal transition. Heat capacity data on all three compounds was analyzed and used in support of the structure solution. The compounds were compared to structurally related bismuth chalcogenides, and the work published in Chemistry of Materials [9]. The publication is presented below with the inclusion of additional thermal conductivity data collected on $Sr_2O_2Bi_2Se_3$, which was analyzed in conjunction with heat capacity data to determine the phonon velocity.

2.5 Synthesis and Structure of Three New Oxychalcogenides: $A_2O_2Bi_2Se_3$ (A = Sr, Ba) and $Sr_2O_2Sb_2Se_3$

The following section reports the key findings of studies on the $Sr_2O_2Bi_2Se_3$, $Ba_2O_2Bi_2Se_3$, and $Sr_2O_2Sb_2Se_3$. This work was co-written by the following authors and published under the following citation:

Chemistry of Materials, **2016**, 28 (3), pp 890-895

DOI: 10.1021/acs.chemmater.5b04536

Jessica R. Panella[1], Juan Chamorro[1], Tyrel M. McQueen[1,2,3,*]

[1]Department of Chemistry, The Johns Hopkins University, Baltimore, MD 21218, USA

[2]Institute for Quantum Matter, Department of Physics, The Johns Hopkins University, Baltimore, MD 21218, USA

[3]Department of Materials Science and Engineering, The Johns Hopkins University, Baltimore, MD 21218, USA

[*]Corresponding author

2.5.1 Abstract

Three new compounds have been added to the alkali chalcogenide and oxychalcogenide families: $Sr_2O_2Bi_2Se_3$, $Ba_2O_2Bi_2Se_3$, and $Sr_2O_2Sb_2Se_3$ were synthesized by direct combination of SrO or BaO with Bi_2Se_3 or Sb_2Se_3. The structure, determined from laboratory X-ray powder diffraction data, consists of double chains of edge-sharing $BiSe_4O$ square pyramids. Temperature-dependent resistance data reveal all three compounds to be insulators, while heat capacity data of $Ba_2O_2Bi_2Se_3$ and $Sr_2O_2Bi_2Se_3$, in conjunction with the literature reports, reveal low energy phonon modes due to bismuth lone pair effects. We propose a specific materials design principle connecting electron count to structural dimensionality by comparison to related chalcogenides, including the BiS_2 superconductors.

2.5.2 Introduction

Oxychalcogenides and alkali chalcogenides have rich and diverse chemistry and have recently come into the spotlight in the field of superconductivity. Compounds with nominal stoichiometry LnOBiS_2 (Ln = La, Nd, Ce, Pr, Yb), LaOBiSe_2, and SrFBiS_2 have been shown to superconduct upon doping the blocking layer, reaching critical temperatures (T_c) as high as T_c ~10 K for Ln = La[10–16]. Superconductivity has also been shown to arise in the $Bi_3O_2S_3$ system with a T_c ~5 K[11, 17]. In all of these compounds the superconductivity is thought to originate from low-dimensional BiX_2 (X = S,Se) layers, separated by blocking layers[10].

We report a new family of compounds: $Sr_2O_2Bi_2Se_3$, $Ba_2O_2Bi_2Se_3$, and $Sr_2O_2Sb_2Se_3$

($A_2O_2B_2Se_3$, A = Sr, Ba; B = Bi, Sb), which bears strong resemblance to the LnOBiX_2 superconductors (SCs). The $A_2O_2B_2Se_3$ structure consists of electronically active quasi-one dimensional bismuth or antimony selenide ribbons isolated from one another by strontium oxide units. Because of the structural and electronic similarity between $A_2O_2B_2Se_3$ and the LnOBiX_2 superconductors, this new family provides a unique opportunity to study the effect of dimensionality on superconductivity. Similar investigations have proven fruitful in quasi-one dimensional analogues of other superconductors, which, while not intrinsically superconductive, have been made to superconduct under pressure with controlled doping [18–21].

Further, the structure of $A_2O_2B_2Se_3$ compounds also shares structural features with many other bismuth and antimony chalcogenides, in particular those with AB_2X_4 (A = Sr, Ba; B = Bi, Sb; X = S, Se) stoichiometry. Close examination of the relationship between structure and composition reveals a connection between electron count and resulting structure progressing from AB_2X_4 to $A_2O_2B_2Se_3$ to LnOBiX_2, providing a new materials design principle for mixed oxide-chalcogenide materials.

2.5.3 Experimental

Reagents. SrO (Strem, 99.9%), BaO (Sigma Aldrich, 99.99%), and Sb (Alfa Aesar, 99.999%) were used as received. Bi (Alfa Aesar 99.998%) was purified by heating to 500°C with a physically separated carbon pellet to act as an oxygen getter. Se (Puratronic 99.999%) was purified by vapor transport at 400°C.

Synthesis. All manipulations were carried out under argon atmosphere in a

glovebox. Stoichiometric ratios of SrO or BaO, Sb or Bi, and Se were combined and ground in an agate mortar and pestle, pelletized, placed in an alumina crucible, and sealed in individual evacuated silica ampoules. For $Sr_2O_2Bi_2Se_3$ and $Ba_2O_2Bi_2Se_3$, the reaction mixtures were ramped to 800°C at 50°C/hr, kept at that temperature for 24 hrs, then furnace cooled to room temperature. The same heating cycle was used for $Sr_2O_2Sb_2Se_3$ but with a max temperature of 700°C. On grinding, all products were dark gray, air stable powders. Samples for resistance and heat capacity measurements underwent additional sintering at their respective annealing temperatures for 24 hours with a 100°C ramp rate on heating and furnace cooling to room temperature. The surfaces of the pellets were evenly shaved off with a razor.

Structural analysis. X-ray powder diffraction (XRPD) data was collected on a laboratory Bruker D8 Focus diffractometer (40 kV, 40 mA, sealed Cu X-ray tube, $K_{\alpha 1}$ 1.540596 Å, $K_{\alpha 2}$ 1.544493 Å) with a Ni filter and LynxEye position sensitive detector at room temperature (*RT*). The scattering range was 2θ = 5–120° with a step size of 0.02° over 4 hrs set using DIFFRAC plus XRD Commander software.

Physical properties measurements. Physical properties measurements were conducted on sintered pellets. Resistance was measured *via* the four probe ac method using the resistivity option of a 9-T Quantum Design Physical Properties Measurement System (PPMS) over the temperature range of T = 300 K to 2 K. Pt leads were attached using two-part silver epoxy (H20E, Epoxy Technology). Heat capacity was measured using the PPMS semiadiabatic heat pulse technique with a temperature range of T = 2 K to 50 K.

2.5.4 Results and discussion

2.5.4.1 Structure solution

The XRPD data and calculated fit for $Sr_2O_2Bi_2Se_3$, which are representative of the series, are shown in Figure 2.10. The unit cell of $Sr_2O_2Bi_2Se_3$ was determined from laboratory XRPD data using the peak indexing feature in the commercial version of the Bruker TOPAS software suite followed by rough LeBail fits to the proposed cells with the highest goodness of fit. The positions of the Bi, Se, and Sr were determined using simulated annealing also in TOPAS. Oxygen was placed in a gap in the structure such that it would be bonded to Sr, and its position was refined using Rietveld profile analysis. Once the oxygen atomic coordinates no longer deviated significantly from initially assigned positions during refinement, all atomic positions as well as unit cell parameters were refined simultaneously, followed by refinement of thermal displacement parameters with the oxygen parameter set equal to the Se2 parameter. Site occupancies were refined, but did not deviate more than 5% from nominal values or affect the goodness of fit and were constrained to 1 in the final refinement. The structure parameters were modified and refined to the XRPD patterns of the isostructural $Ba_2O_2Bi_2Se_3$ and $Sr_2O_2Sb_2Se_3$. Bond valence sums (BVS) including all nearest neighbor interactions were used to check the validity of the structure solutions. The refined parameters and bond valence sums are summarized in Table 1. Attempts to use the alternate choice of spacegroups $A2/a$ (c = 18.99914(7), R_{wp} = 5.25) and $C2/m$ (a = 13.43734(5), c = 9.49955(3), R_{wp} = 5.05) resulted in no visual or statistical improvement over $P2_1/c$. Crystallographic information files with the alternate space groups used for refinement were generated

using ISODISTORT[22]. Optimal samples of $Sr_2O_2Bi_2Se_3$ contain no detectable impurities, though $Ba_2O_2Bi_2Se_3$ samples frequently had a small Bi_3Se_4 impurity, and $Sr_2O_2Sb_2Se_3$ contained very small amounts of Sr_5Sb_3, SrSe, and $SrSe_2O_5$.

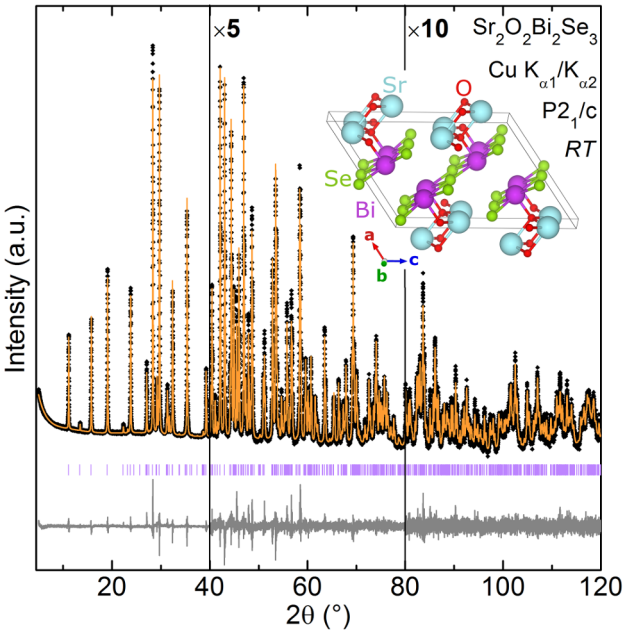

Figure 2.10: Rietveld refinement to XRPD data collected on $Sr_2O_2Bi_2Se_3$ using spacegroup $P2_1/c$. Black diamonds show the collected data, the orange line is the calculated fit, the gray line is the difference, and the lavender ticks show allowed peak positions. Full page width figure provided in supporting information.

The structure of the new compounds, Figure 2.10 inset, consists of edge sharing $BiSe_4O$ square pyramids, which exist in quasi-one dimensional ribbons that extend in the b direction and are truncated to two pyramidal units, approximately 8.5 Å wide, in the transverse direction. Within a strip of square pyramids, one row of $BiSe_4O$ units points up, and the neighboring row points down. The bismuth selenide ribbons are connected to each other by apically bonded oxygen atoms in SrO units creating a step-like structure in the $(\bar{1}\ 0\ 2)$ direction. Each set of

	Parameter	$Sr_2O_2Bi_2Se_3$	$Ba_2O_2Bi_2Se_3$	$Sr_2O_2Sb_2Se_3$
	a (Å)	9.49953(3)	9.82047(6)	9.42425(12)
	b (Å)	4.084794(16)	4.19033(3)	4.05708(5)
	c (Å)	13.43734(5)	13.90441(8)	13.34148(18)
	β (°)	122.8613(3)	123.6919(3)	121.9549(7)
A	x	0.10335(11)	0.10553(10)	0.10423(16)
	y	0.9955(18)	0.008(3)	0.0125(17)
	z	0.89461(6)	0.90206(6)	0.89433(9)
	B (Å^2)	0.74(3)	0.64(3)	1.08(4)
	BVS	2.03	2.28	1.99
B	x	0.63518(7)	0.6338(2)	0.64276(17)
	y	0.0071(7)	0.997(2)	0.9953(15)
	z	0.69183(4)	0.68721(5)	0.69853(11)
	B (Å^2)	0.834(18)	1.16(2)	2.72(4)
	BVS	3.18	3.00	2.60
O	x	0.1448(6)	0.1511(9)	0.1657(10)
	y	0.021(6)	0.983(10)	0.955(4)
	z	0.3138(4)	0.3158(5)	0.3196(6)
	BVS	-2.08	-2.19	-2.21
Se1	B (Å^2)	1.47(5)	1.40	4.27(8)
	BVS	-2.50	-2.41	-1.69
Se2	x	0.20942(14)	0.2205(2)	0.2000(2)
	y	0.004(2)	0.009(4)	0.0222(17)
	z	0.62571(9)	0.63641(12)	0.62414(12)
	B (Å^2)	1.12(3)	1.40(5)	2.09(5)
	BVS	-1.88	-1.88	-1.62
	R_P (%)	3.88	4.10	3.86
	R_{wp} (%)	5.04	5.35	5.00
	χ^2	1.70	1.78	1.67

Table 2.6: Structural parameters for $A_2O_2B_2Se_3$. Space group $P2_1/c$ (#14). Atomic positions: A, B, O, Se2: 4e (x, y, z), Se1: 2b $(1/2, 0, 0)$. All atomic displacement parameters were refined except for oxygen, which was constrained to be equal to the that of Se2. All sites were fixed to full occupancy. Errors are statistical only.

$BiSe_4O(SrO)$ steps is entirely disconnected from the neighboring set. The oxygen atoms occupy the center of edge-sharing tetrahedra with Sr atoms at three of the corners and a Bi at the fourth, which resembles the PbO-type oxygen environment seen in $LnOBiX_2$[23].

2.5.4.2 Physical properties

The normalized resistivity of all $A_2O_2B_2Se_3$ compounds showed an exponential increase with decreasing temperature consistent with activated transport, as expected on the basis of the electron count within the bismuth selenide planes: each selenium has filled s- and p-orbitals, and the remaining valence electrons of bismuth are localized in the non-bonding lone pair, as discussed below. The data is plotted as the natural log of normalized resistivity versus inverse temperature in Figure 2.11 along with linear fits that were used to calculate the band gap of each material.

The slope of the line given by the plot of $\ln(\rho/\rho_{300})$ versus T^{-1} is given by $E_g/(2k_B \cdot T)$, where E_g is the band gap energy and k_B is the Boltzmann constant. The band gap for each compound was calculated by multiplying the slope of the respective fit line by $2k_B$, and the results are shown in Table 2.7. The room temperature resistivities ($\pm$50%) are given in Table 2.7, the magnitude of which mirrors the slope of the respective fit line. Linear fits using the variable range hopping model for $T^{-1/n}$ (where n = 2 – 4) showed no improvement over the standard T^{-1} fit. The small size of the measured band gaps is probably a result of carrier doping via uncontrolled selenium vaporization during synthesis and

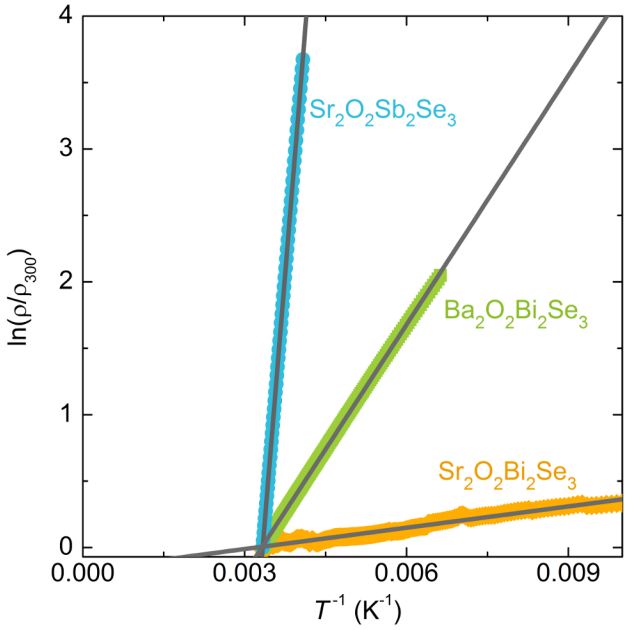

Figure 2.11: Temperature-dependent resistivity of $Sr_2O_2Bi_2Se_3$, $Ba_2O_2Bi_2Se_3$, and $Sr_2O_2Sb_2Se_3$ shown as the natural log of the resistivity normalized by their respective values at T = 300 K ($\rho_{300\ K}$) plotted against inverse temperature. Data for $Sr_2O_2Bi_2Se_3$, $Ba_2O_2Bi_2Se_3$, and $Sr_2O_2Sb_2Se_3$ are shown as orange diamonds, green squares, and blue circles, respectively. Gray lines are the linear fits to each data set used to calculate a nominal band gap for each compound. Errors are represented by the size of the points.

sintering of the pellet.

There is a relationship between the normalized resistivity of each compound and its structure. $Sr_2O_2Bi_2Se_3$ has the lowest apparent band gap (E_g), and the most uniformity in *B*-Se bond lengths in that there is little variation in length among the four distinct *B*-Se bonds. The $Sr_2O_2Sb_2Se_3$ structure has both the shortest and the longest *B*-Se bonds of all three compounds while the average is comparable to that of $Sr_2O_2Bi_2Se_3$, resulting in a higher standard deviation and correspondingly larger band gap. This observation indicates that the majority of the electronic properties of these materials originate from the bismuth and antimony selenide, which aligns

	$Sr_2O_2Bi_2Se_3$	$Ba_2O_2Bi_2Se_3$	$Sr_2O_2Sb_2Se_3$
ρ_{300} (Ω cm)	5.002(2)	304.213(14)	258180(40)
E_g (eV)	0.0092(1)	0.11(1)	0.85(1)
$\bar{x}_{BL}$ (Å)	2.94	2.97	2.95
σ_{BL} (Å)	0.05	0.06	0.11

Table 2.7: The resistivity at T = 300 K, measured band gap (E_g), average B-Se bond length ($\bar{x}_{BL}$), and the standard deviation of the B-Se bond lengths (σ_{BL}) for each of the $A_2O_2B_2Se_3$ compounds. The standard deviations in this table do not represent error of $\bar{x}_{BL}$ but the amount of variation among the bond lengths.

Parameter	$Sr_2O_2Bi_2Se_3$	$Ba_2O_2Bi_2Se_3$	$Bi_2Ti_2O_7$*	Bi_2NbInO_7*
θ_D (K)	182(1)	168(1)	280	–
s	5.61(4)	5.64(5)	–	–
p_1	0.116(19)	0.17(3)	0.32(8)	0.27(7)
E_1 (meV)	2.63(10)	2.60(9)	2.3(2)	2.8(2)
p_2	1.71(6)	1.65(7)	2.0(5)	1.8(5)
E_2 (meV)	5.15(7)	4.83(8)	5.5(5)	6(1)

*from ref. [24]

Table 2.8: Fit parameters for the heat capacity data on $Sr_2O_2Bi_2Se_3$ are shown in the first column. The second and third columns show oscillator strengths and energies for $Bi_2Ti_2O_7$ and Bi_2NbInO_7 for comparison.

with claims that the superconductivity in LnOBiX_2 compounds exists within the BiS_2 planes[10]. This reinforces the suitability of $A_2O_2B_2Se_3$ for investigation of the role of dimensionality in superconductivity.

Heat capacity for $Sr_2O_2Bi_2Se_3$ is plotted as C/T^3 versus T on a log scale in Figure 2.12. A fit to this data calculated using one Debye mode and two Einstein modes is shown. The fit equation for the Einstein modes was that used by Melot *et al.*, reflecting oscillation of bismuth due to its lone pair[24] . The Debye temperature (θ_D) and spectral weight (s) for the Debye mode, oscillator strengths (p_1,p_2) and energies (E_1, E_2) for each of the two Einstein modes, and the electronic

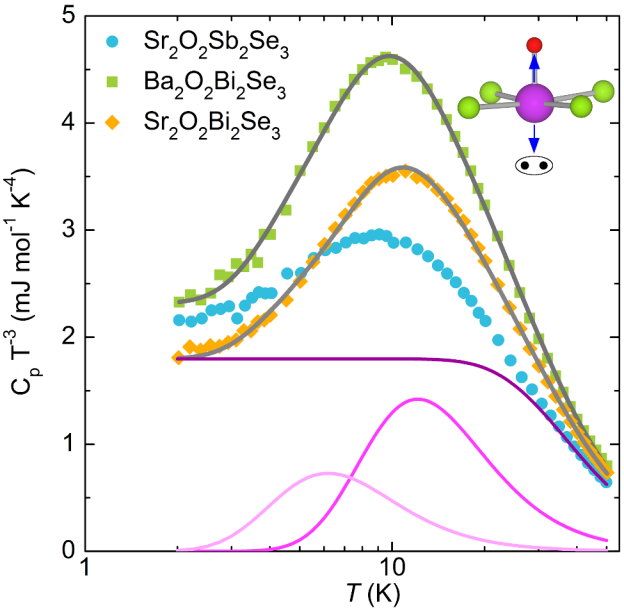

Figure 2.12: Heat capacity of $Sr_2O_2Bi_2Se_3$ (orange diamonds), $Ba_2O_2Bi_2Se_3$ (green squares), and $Sr_2O_2Sb_2Se_3$ (blue circles) as a function of temperature, plotted as C_p/T^3 vs T on a log scale. The gray lines overlayed on the $Sr_2O_2Bi_2Se_3$ and $Ba_2O_2Bi_2Se_3$ data sets represent the fits of one Debye mode and two Einstein modes to those data sets. The contributions to the total fit for $Sr_2O_2Bi_2Se_3$ are shown as lines in shades of purple, with the lighter two being the Einstein modes and the darkest the Debye mode. The inset shows the proposed bismuth motion that results in the Einstein modes in the heat capacity.

coefficient γ were calculated. The electronic coefficient approached zero, indicating that there is no electronic contribution to the low temperature heat capacity. This is supported by the activated transport behavior seen in the resistivity measurements. The calculated fit parameters for the Debye and Einstein modes are shown in Table 2.8 and values for similar compounds as reported by Melot *et al.* are provided for comparison[24]. A peak in the low temperature C/T^3 versus log T data is observed in almost all bismuth-containing compounds, such as $Bi_2Ti_2O_7$ and Bi_2NbInO_7, and is usually attributed to local displacements as a result of

the Bi lone pair effect[24]. The two Einstein modes that fit the peak at around T = 11 K in the present data have a combined spectral weight that is roughly equal to the number of Bi atoms in the formula unit, in agreement with this interpretation.

2.5.5 Calculation of mean phonon velocity

The mean phonon velocity, v, was calculated using the constants determined from fits to heat capacity and thermal conductivity data in the following way. The coefficient of the phonon contribution to heat capacity, β_C, is given by

$$\beta_C = \frac{9Rs}{\theta_D^3} \int_0^{\theta_D/T} \frac{x^2 e^x}{(e^x - 1)^2} dx \tag{2.4}$$

where T is temperature, R is the ideal gas constant, s is the number of Debye oscillators, θ_D is the Debye temperature, and x is given by $\hbar\omega/k_B T$ where ω is the angular frequency of the phonons[25].

The coefficient of the phonon contribution to thermal conductivity, β_κ, is given by

$$\beta_\kappa = (\frac{k_B}{2\pi^2 v})(\frac{k_B}{\hbar})^3 \int_0^{\theta_D/T} \tau(x,T) \frac{x^2 e^x}{(e^x - 1)^2} dx \tag{2.5}$$

where k_B is the Boltzmann constant, v is the mean phonon velocity, and $\tau(x,T)$ is the combined relaxation time for all scattering processes[26, 27]. In the general

case, the total relaxation time $\tau(x,T)$ has the form

$$\tau(x,T) = (\tau_B^{-1} + \tau_I^{-1} + \tau_N^{-1} + \tau_U^{-1})^{-1} \tag{2.6}$$

where τ_B^{-1} is the temperature-independent boundary scattering relaxation time and has the form v/L where L is the grain size; τ_I^{-1} is the impurity scattering relaxation time and has the form ax^4T^4; τ_N^{-1} is the scattering due to normal three-phonon processes and has the form $B_1x^2T^5$; and τ_U^{-1} is the relaxation time due to Umklapp scattering and has the form $B_2x^2T^5$[26, 28]. It is assumed that in the low temperature limit, the only process that contributes significantly to the overall relaxation time is boundary scattering, so that $\tau(x,T) = L/v$.

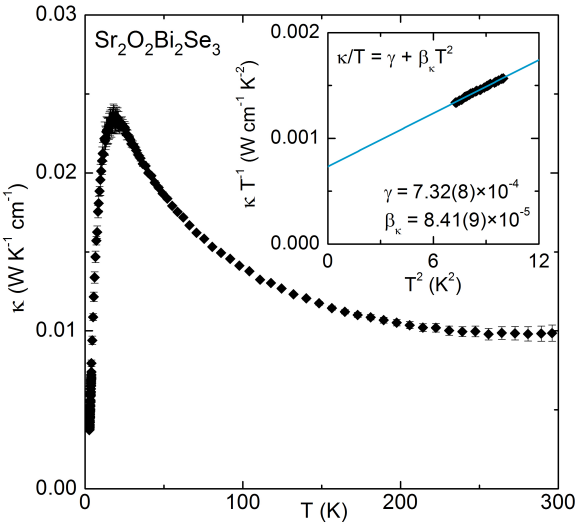

Figure 2.13: Temperature-dependent thermal conductivity for $Sr_2O_2Bi_2Se_3$. Inset shows a linear fit to the κ/T plotted against T^2 in the low temperature region.

In order to extract the mean phonon velocity, β_C and β_κ were taken from the slope of a fit to the linear portion of the C/T vs T^2 and κ/T vs T^2 plots, respectively.

The Debye temperature θ_D and number of Debye oscillators, s, were taken from the fit to the C/T^3 vs log T data. The size of the grains, L, was determined from the Rietveld refinement to the XRPD data for the sample on which heat capacity and thermal conductivity measurements were done. The ratio, β_C/β_κ, from the calculated values was set equal to the ratio of the form of the β coefficients as given above:

$$\frac{\beta_C}{\beta_\kappa} = (\frac{9Rs}{\theta_D^3})(\frac{2\pi^2\hbar^3}{k_B^4})(\frac{v^2}{L}). \tag{2.7}$$

The integral conveniently cancels, leaving only constants and the mean phonon velocity. Solving this equation for c with values for constants plugged in gives a mean phonon velocity of $v \approx 1100$ m/s. The value for v calculated in this way is comparable to that which has been calculated or measured in similar compounds, such as in Bi_2Se_3 and Sb_2Te_3, where the respective average phonon velocities are 2900 m/s and 2888 m/s.[29, 30]

2.5.5.1 Materials Design Principles

Many bismuth and antimony chalcogenides contain common structural features, particularly bismuth- or antimony-centered square pyramids, which leave room to accommodate the lone pair. With an understanding of the structural relationship between different compounds it is possible to develop a guide for designing new materials with desired structural features. Compounds with the generic formula AB_2X_4 (A = Sr, Ba; B = Bi, Sb; X = S, Se), along with the family of LnOBiX_2 SCs and $A_2O_2B_2Se_3$ share common building blocks and a connection between stoichiometry

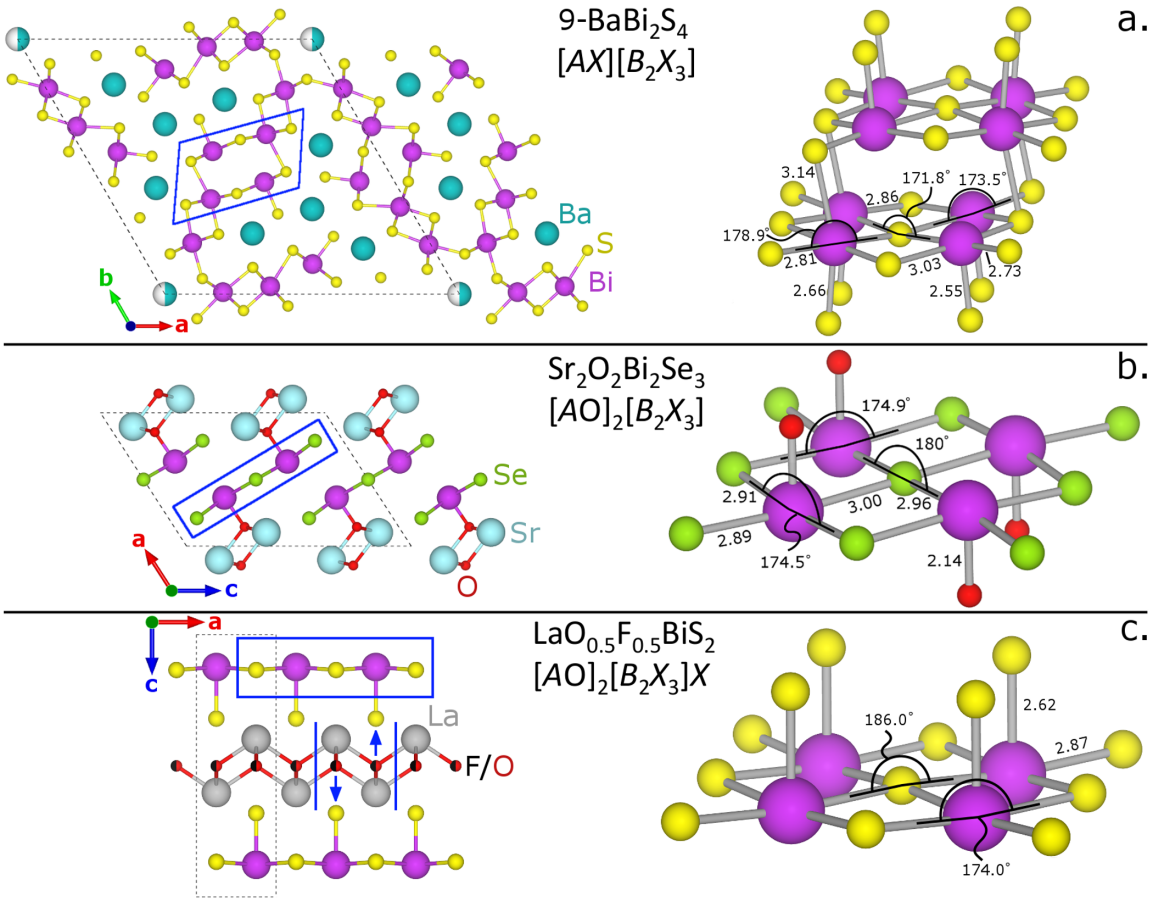

Figure 2.14: The structures of **a.** 9-$BaBi_2S_4$[31], **b.** $Sr_2O_2Bi_2Se_3$, and **c.** $LaO_{0.5}F_{0.5}BiS_2$[10]. Blue boxes highlight similar structural units, and arrows indicate distortions that relate the structures. All error bars are less than or equal to three in the last digit and are not shown to aid in clarity of the figure.

and structure can be inferred [11–13, 31–37].

AB_2X_4 compounds typically consist of such square pyramids in varying orientations with charge-balancing alkali metal ions filling gaps between, though the overall structure is dependent on the precise composition of the sample. A clear connection between $A_2O_2B_2Se_3$ and AB_2X_4 compounds can be drawn using

9-$BaBi_2S_4$ as an example[31]. 9-$BaBi_2S_4$ and $A_2O_2B_2Se_3$ share the same structural feature: quasi-one dimensional strips of edge sharing square pyramids with A-cations filling gaps between adjacent strips. The difference between these two structures in terms of the repeating units is that 9-$BaBi_2S_4$ is built of two pairs of pyramidal units separated by one A-cation, while $A_2O_2B_2Se_3$ consists of one pair of pyramidal units separated by one A-cation. There is no equivalent in $A_2O_2B_2Se_3$ to the Bi-S bond adjoining adjacent square pyramidal pairs. In $Sr_2O_2Bi_2Se_3$, the distance between bismuth in one ribbon and the nearest selenium in the neighboring ribbon is 3.6398(14) Å, lending itself only to long range interactions. The relationship between the two structures can be seen from the formulas of 9-$BaBi_2S_4$ and $A_2O_2B_2Se_3$ by writing them more suggestively as $[AX][B_2X_3]$ and $[AO]_2[B_2X_3]$, respectively. The difference between the stoichiometry and corresponding structure is then the addition of an extra alkali metal-anion unit in $A_2O_2B_2Se_3$. This unit is inserted between two of the pairs of edge sharing pyramids, creating the separated single pairs of square pyramids.

Similarly, the bismuth sulfide SCs also consist of edge sharing square pyramidal units and metal oxide units, however both of these exist in two-dimensional planes in the $LnOBiX_2$ compounds. Rewriting the formula for the bismuth sulfide SCs as $[LnO]_2[B_2X_3]X$ highlights the stoichiometric contrast to $A_2O_2B_2Se_3$, which is the additional chalcogenide anion present in $LnOBiX_2$ compounds[11–13, 37]. The substitution of a trivalent rare earth in $LnOBiX_2$ for the divalent alkali metal in $A_2O_2B_2Se_3$ maintains charge balance, while the apical bond to the additional sulfur replaces the inter-plane bond to oxygen seen in $A_2O_2B_2Se_3$ to satisfy the

bismuth coordination sphere. Without the Bi-O bond, the oxygen atoms form bonds with neighboring *Ln* ions, resulting in the continuous PbO-type plane seen in *Ln*OBiX_2[38].

The distortion in the bismuth selenide ribbons is reminiscent of that seen in the BiX_2 plane in *Ln*OBiX_2 SCs. Systematic structural investigations on $LaO_{1-x}F_xBiS_2$ revealed a composition-dependent buckling of the BiS_2 planes.[39–42]. In $Sr_2O_2Bi_2Se_3$, the Bi-Se1-Bi bonds within the ribbon are constrained by symmetry to have a bond angle of 180°. The dangling Bi-Se bonds at the edge of the bismuth selenide ribbons in $Sr_2O_2Bi_2Se_3$ bend slightly out of the plane of the ribbon, with a Se1-Bi-Se2 bond angles of 174.5° and 174.9°. The bonds between Bi and Se2, at 2.91 and 2.89 Å, are shorter than the interior Bi-Se1 bonds, at 2.96 and 3.00 Å. Similar to the *Ln*OBiX_2 compounds, the apical bond, which in this compound is to O rather than a chalcogenide, is short compared to expectations, with a bond length of only 2.23 Å (versus 2.4 Å from ionic radii)[43]. Figure 2.14 summarizes the bond lengths and angles in $Sr_2O_2Bi_2Se_3$ and compares them to those of the as-grown superconductor $LaO_{0.5}F_{0.5}BiS_2$. The average Se1-Bi-Se1 bond angle, 174.7° in $Sr_2O_2Bi_2Se_3$, is very similar to the S1-Bi-S1 angle of 175.2° in $LaO_{0.5}F_{0.5}BiS_2$[40]. The bond lengths and angles reinforce the similarity between BiS_2 planes in $LaO_{0.5}F_{0.5}BiS_2$ and the bismuth selenide ribbons in $Sr_2O_2Bi_2Se_3$ and highlight the potential to use $A_2O_2B_2Se_3$ compounds as quasi-one-dimensional analogues of *Ln*OBiX_2 SCs.

2.5.6 Conclusion

The new compounds $Sr_2O_2Bi_2Se_3$, $Ba_2O_2Bi_2Se_3$, and $Sr_2O_2Sb_2Se_3$ were synthesized and their structures determined, adding to known oxychalcogenides and low-dimensional materials. The heat capacity data for $Sr_2O_2Bi_2Se_3$ displays a feature commonly associated with the bismuth lone pair effect, which corroborates the coordination of bismuth in the reported structure. Resistance data for the $A_2O_2B_2Se_3$ series displays the insulating behavior expected given the electron count.

The structures of the new compounds were compared with those of known chalcogenides, demonstrating a new materials design rule in oxide chalcogenide materials. Given their similarity to known SCs, it will be worthwhile to investigate the effects of controlled doping and pressure to learn about the role of dimensionality in superconductivity. Manipulation of the chemical formulae on the basis of the structural relationships outlined in this work will also lead to an increased understanding of structure-property relationships in these systems.

2.5.7 Acknowledgement

This research was supported by the Research Corporation for Science Advancement Cottrell Scholar award.

2.5.8 Table of contents figure

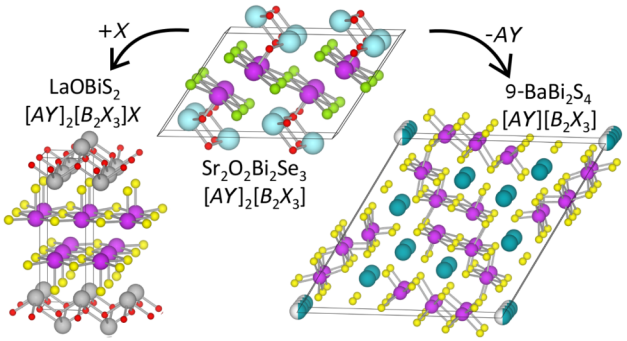

For Table of Contents Only

2.6 Supporting information

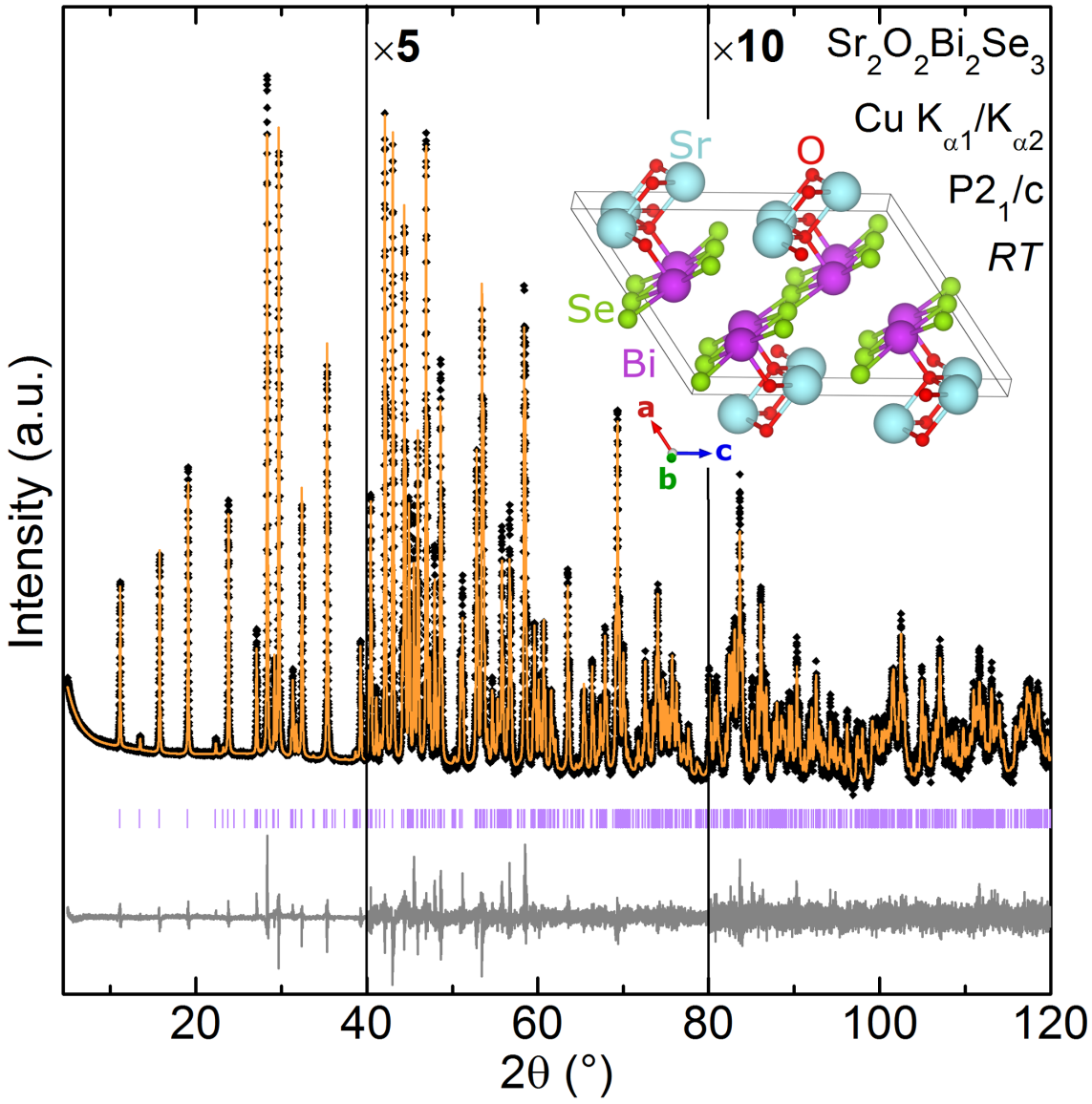

Figure 2.15: Rietveld refinement to XRPD data for $Sr_2O_2Bi_2Se_3$, with expanded regions to highlight the quality of the fit. The data is shown as black diamonds, the fit is shown in orange, the expected peak positions are shown in lavender, and the difference curve is shown in gray.

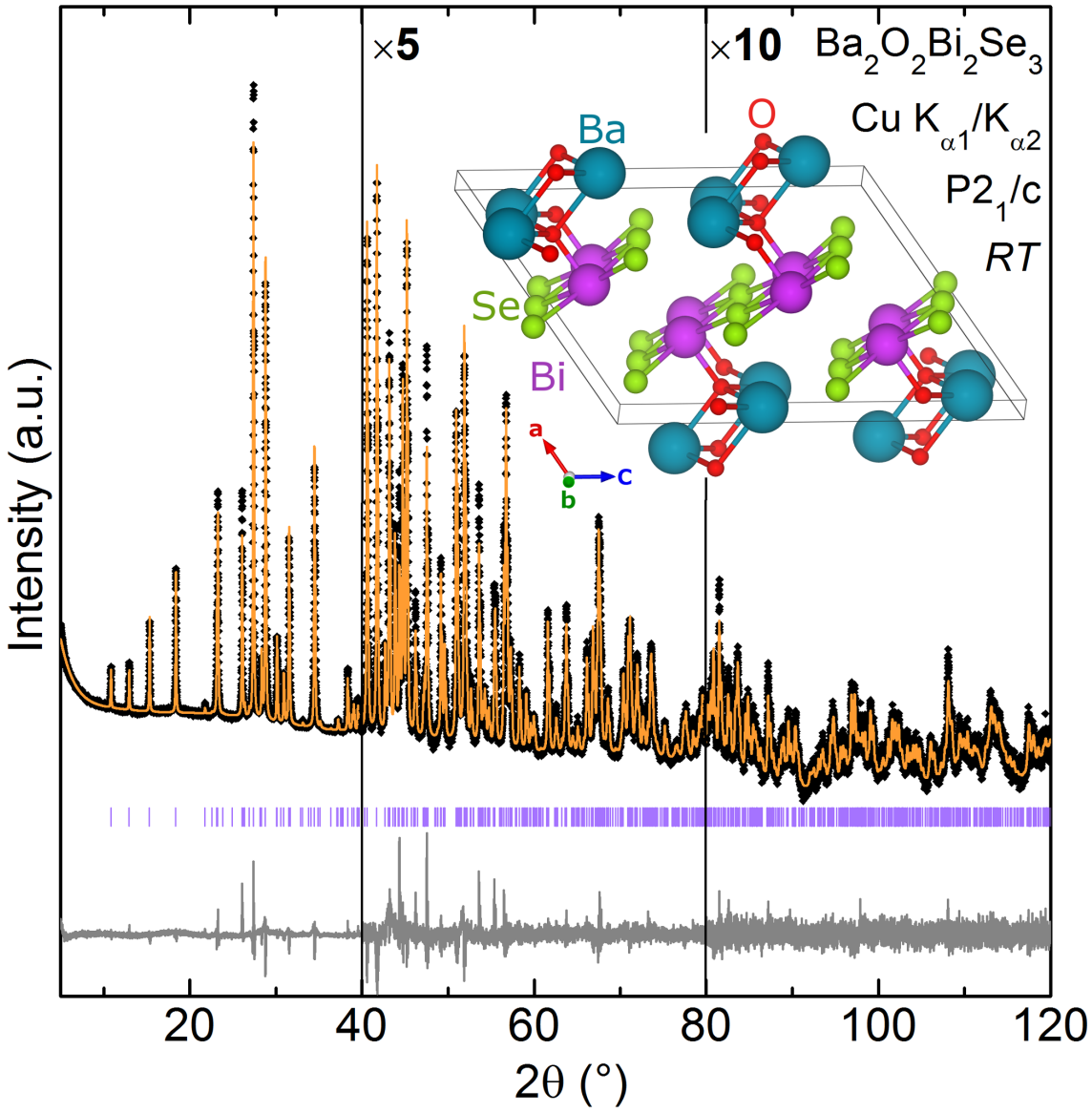

Figure 2.16: Rietveld refinement to XRPD data for $Ba_2O_2Bi_2Se_3$, with expanded regions to highlight the quality of the fit. The data is shown as black diamonds, the fit is shown in orange, the expected peak positions are shown in lavender, and the difference curve is shown in gray.

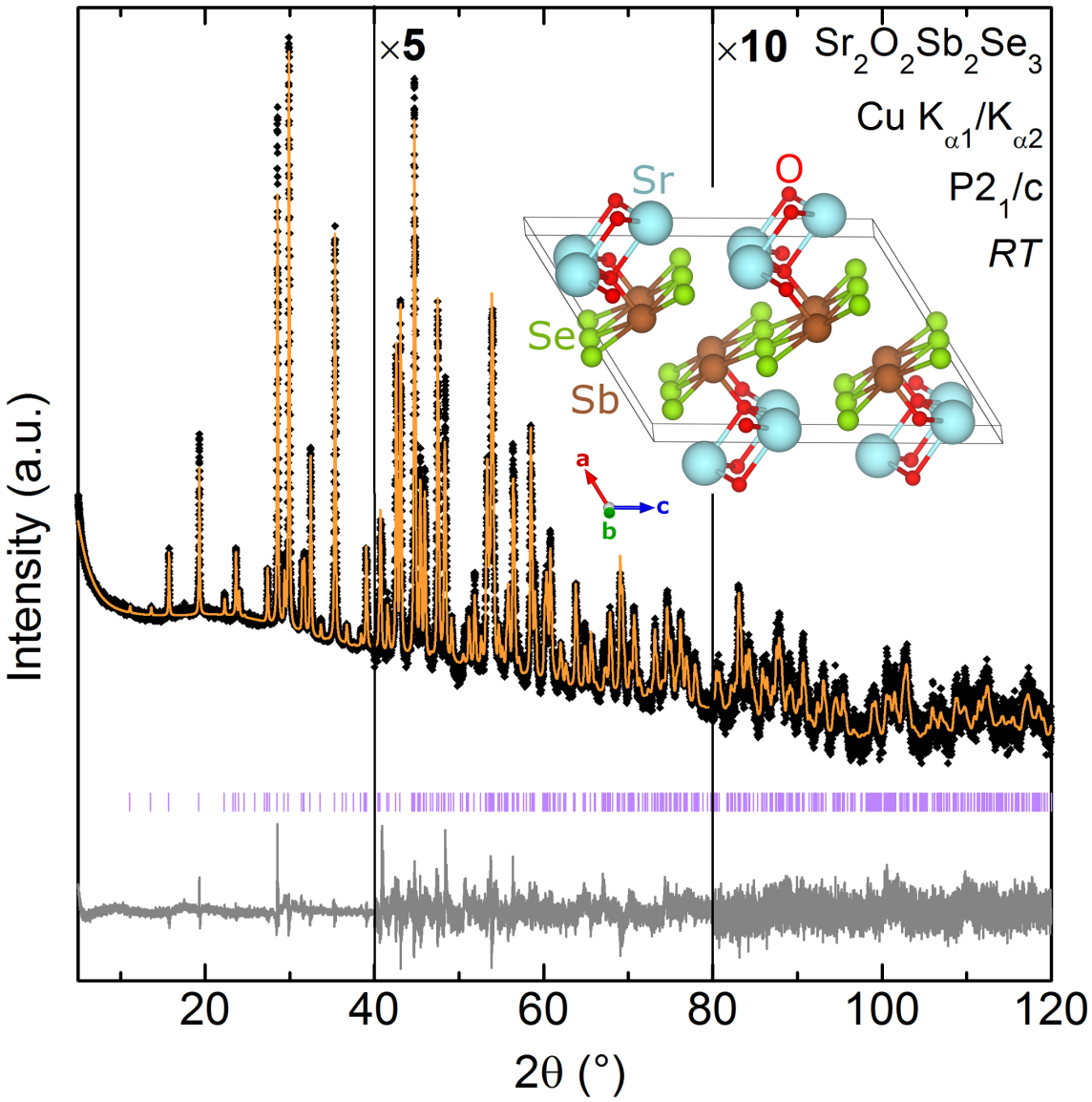

Figure 2.17: Rietveld refinement to XRPD data for $Sr_2O_2Sb_2Se_3$, with expanded regions to highlight the quality of the fit. The data is shown as black diamonds, the fit is shown in orange, the expected peak positions are shown in lavender, and the difference curve is shown in gray.

References

[1] Kristian Fossheim and Asle Sudbo. *Superconductivity: Physics and Applications*. Wiley, 2005. ISBN: 978-0-470-84452-6.

[2] Roland Hott, Reinhold Kleiner, Thomas Wolf, and Gertrud Zwicknagl. "Review on Superconducting Materials". In: *arXiv:1306.0429 [cond-mat]* (2013).

[3] Colin K. Blakely, Shaun R. Bruno, and Viktor V. Poltavets. "Low-Temperature Solvothermal Approach to the Synthesis of $La_4Ni_3O_8$ by Topotactic Oxygen Deintercalation". In: *Inorg. Chem.* 50.14 (2011), pp. 6696–6700. ISSN: 0020-1669. DOI: 10.1021/ic200677p.

[4] Cesare Brisi, Mario Vallino, and Fedele Abbattista. "Composition and structure of two hitherto unidentified phases in the system La_2O_3-NiO-O". In: *Journal of the Less Common Metals* 79.2 (1981), pp. 215–219. ISSN: 0022-5088. DOI: 10.1016/0022-5088(81)90070-9.

[5] Z. Zhang and M. Greenblatt. "Synthesis, Structure, and Properties of $Ln_4Ni_3O_{10-\delta}$ (Ln= La, Pr, and Nd)". In: *Journal of Solid State Chemistry* 117.2 (1995), pp. 236–246. ISSN: 0022-4596. DOI: 10.1006/jssc.1995.1269.

[6] Maria Deus Carvalho, Fernanda Madalena A. Costa, Isabel da Silva Pereira, Alain Wattiaux, Jean Marc Bassat, Jean Claude Grenier, and Michel Pouchard. "New preparation method of $La_{n+1}Ni_nO_{3n+1--\delta}$ (n=2,3)". en. In: *Journal of Materials Chemistry* 7.10 (1997), pp. 2107–2111. DOI: 10.1039/A702424J.

[7] M. D. Carvalho, M. M. Cruz, A. Wattiaux, J. M. Bassat, F. M. A. Costa, and M. Godinho. "Influence of oxygen stoichiometry on the electronic properties of $La_4Ni_3O_{10\pm\delta}$". In: *Journal of Applied Physics* 88.1 (2000), pp. 544–549. ISSN: 0021-8979. DOI: 10.1063/1.373693.

[8] A. E. Danks, S. R. Hall, and Z. Schnepp. "The evolution of 'sol–gel' chemistry as a technique for materials synthesis". en. In: *Materials Horizons* 3.2 (2016), pp. 91–112. DOI: 10.1039/C5MH00260E.

[9] Jessica R. Panella, Juan Chamorro, and Tyrel M. McQueen. "Synthesis and Structure of Three New Oxychalcogenides: $A_2O_2Bi_2Se3$ (A = Sr, Ba) and $Sr_2O_2Sb_2Se_3$". In: *Chem. Mater.* 28.3 (2016), pp. 890–895. ISSN: 0897-4756. DOI: 10.1021/acs.chemmater.5b04536.

[10] Yoshikazu Mizuguchi, Satoshi Demura, Keita Deguchi, Yoshihiko Takano, Hiroshi Fujihisa, Yoshito Gotoh, Hiroki Izawa, and Osuke Miura. "Superconductivity in Novel BiS_2-Based Layered Superconductor $LaO_{1-x}F_xBiS_2$". In: *J. Phys. Soc. Jpn.* 81.11 (2012), p. 114725. ISSN: 0031-9015, 1347-4073. DOI: 10.1143/JPSJ.81.114725.

[11] Yoshikazu Mizuguchi, Hiroshi Fujihisa, Yoshito Gotoh, Katsuhiro Suzuki, Hidetomo Usui, Kazuhiko Kuroki, Satoshi Demura, Yoshihiko Takano, Hiroki Izawa, and Osuke Miura. "BiS_2-based layered superconductor $Bi_4O_4S_3$". In: *Phys. Rev. B* 86.22 (2012), p. 220510. DOI: 10.1103/PhysRevB.86.220510.

[12] Satoshi Demura, Keita Deguchi, Yoshihiko Takano, Hiroshi Fujihisa, Yoshito Gotoh, Hiroki Izawa, Osuke Miura, and Yoshikazu Mizuguchi. "Superconductivity in novel BiS_2-based layered superconductor $LaO_{1-x}F_xBiS_2$". In: *J. Phys. Soc. Jpn.* 81 (2012), p. 114725.

[13] D. Yazici, K. Huang, B.D. White, A.H. Chang, A.J. Friedman, and M.B. Maple. "Superconductivity of F-substituted $LnOBiS_2$ (Ln=La, Ce, Pr, Nd, Yb) compounds". In: *Philos. Mag. B* 93.6 (2013), pp. 673–680. ISSN: 1478-6435. DOI: 10.1080/14786435.2012.724185.

[14] A. Krzton-Maziopa, Z. Guguchia, E. Pomjakushina, V. Pomjakushin, R. Khasanov, H. Luetkens, P. K. Biswas, A. Amato, H Keller, and K. Conder. "Superconductivity in a new layered bismuth oxyselenide: $LaO_{0.5}F_{0.5}BiSe_2$". en. In: *J. Phys.: Condens. Matter* 26.21 (2014), p. 215702. ISSN: 0953-8984. DOI: 10.1088/0953-8984/26/21/215702.

[15] Hechang Lei, Kefeng Wang, Milinda Abeykoon, Emil S. Bozin, and Cedomir Petrovic. "New Layered Fluorosulfide $SrFBiS_2$". In: *Inorg. Chem.* 52.18 (2013), pp. 10685–10689. ISSN: 0020-1669. DOI: 10.1021/ic4018135.

[16] Xi Lin, Xinxin Ni, Bin Chen, Xiaofeng Xu, Xuxin Yang, Jianhui Dai, Yuke Li, Xiaojun Yang, Yongkang Luo, Qian Tao, Guanghan Cao, and Zhuan Xu. "Superconductivity induced by La doping in $Sr_{1-x}La_xFBiS_2$". In: *Phys. Rev. B* 87.2 (2013), p. 020504.

[17] W. Adam Phelan, David C. Wallace, Kathryn E. Arpino, James R. Neilson, Kenneth J. Livi, Che R. Seabourne, Andrew J. Scott, and Tyrel M. McQueen. "Stacking Variants and Superconductivity in the Bi-O-S System". In: *J. Am. Chem. Soc.* 135.14 (2013), pp. 5372–5374. ISSN: 0002-7863. DOI: 10.1021/ja4011767.

[18] J. M. Caron, J. R. Neilson, D. C. Miller, A. Llobet, and T. M. McQueen. "Iron displacements and magnetoelastic coupling in the antiferromagnetic spin-ladder compound $BaFe_2Se_3$". In: *Phys. Rev. B* 84.18 (2011), p. 180409. DOI: 10.1103/PhysRevB.84.180409.

[19] J. M. Caron, J. R. Neilson, D. C. Miller, K. Arpino, A. Llobet, and T. M. McQueen. "Orbital-selective magnetism in the spin-ladder iron selenides $Ba_{1-x}K_xFe_2Se_3$". In: *Physical Review B* 85.18 (2012), p. 180405. DOI: 10.1103/PhysRevB.85.180405.

[20] Hiroki Takahashi, Akira Sugimoto, Yusuke Nambu, Touru Yamauchi, Yasuyuki Hirata, Takateru Kawakami, Maxim Avdeev, Kazuyuki Matsubayashi, Fei Du, Chizuru Kawashima, Hideto Soeda, Satoshi Nakano, Yoshiya Uwatoko, Yutaka Ueda, Taku J. Sato, and Kenya Ohgushi. "Pressure-induced superconductivity in the iron-based ladder material $BaFe_2S_3$". en. In: *Nat. Mater.* 14.10 (2015), pp. 1008–1012. ISSN: 1476-1122. DOI: 10.1038/nmat4351.

[21] Masatomo Uehara, Takashi Nagata, Jun Akimitsu, Hiroki Takahashi, Nobuo Môri, and Kyoichi Kinoshita. "Superconductivity in the Ladder Material $Sr_{0.4}Ca_{13.6}Cu_{24}O_{41.84}$". In: *J. Phys. Soc. Jpn.* 65.9 (1996), pp. 2764–2767. ISSN: 0031-9015. DOI: 10.1143/JPSJ.65.2764.

[22] Branton J. Campbell, Harold T. Stokes, David E. Tanner, and Dorian M. Hatch. "ISODISPLACE: a web-based tool for exploring structural distortions". In: *J. Appl. Crystallogr.* 39.4 (2006), pp. 607–614. ISSN: 0021-8898. DOI: 10.1107/S0021889806014075.

[23] P. Boher, P. Garnier, J. R. Gavarri, and A. W. Hewat. "Monoxyde quadratique PbOα (I): Description de la transition structurale ferroelastique". In: *J. Solid*

State Chem. 57.3 (1985), pp. 343–350. ISSN: 0022-4596. DOI: 10.1016/0022-4596(85)90197-5.

[24] Brent C. Melot, Ronald Tackett, Jim O'Brien, Andrew L. Hector, Gavin Lawes, Ram Seshadri, and Arthur P. Ramirez. "Large Low Temperature Specific Heat in Pyrochlore $Bi_2Ti_2O_7$". In: *Phys. Rev. B* 79.22 (2009). ISSN: 1098-0121, 1550-235X. DOI: 10.1103/PhysRevB.79.224111.

[25] A Tari. *The Specific Heat of Matter at Low Temperatures*. en. Imperial College Press, 2003. ISBN: 978-1-86094-314-0 978-1-86094-939-5.

[26] M. G. Holland. "Analysis of Lattice Thermal Conductivity". In: *Phys. Rev.* 132.6 (1963), pp. 2461–2471. DOI: 10.1103/PhysRev.132.2461.

[27] Joseph Callaway. "Model for Lattice Thermal Conductivity at Low Temperatures". In: *Phys. Rev.* 113.4 (1959), pp. 1046–1051. DOI: 10.1103/PhysRev.113.1046.

[28] Bal Krishna Agrawal and G. S. Verma. "Lattice Thermal Conductivity at Low Temperatures". In: *Phys. Rev.* 126.1 (1962), pp. 24–29. DOI: 10.1103/PhysRev.126.24.

[29] Dohun Kim, Qiuzi Li, Paul Syers, Nicholas P. Butch, Johnpierre Paglione, S. Das Sarma, and Michael S. Fuhrer. "Intrinsic Electron-Phonon Resistivity in Bi2Se3 in the Topological Regime". In: *Phys. Rev. Lett.* 109.16 (2012). ISSN: 0031-9007, 1079-7114. DOI: 10.1103/PhysRevLett.109.166801.

[30] Luciana W. da Silva and Massoud Kaviany. "Micro-thermoelectric cooler: interfacial effects on thermal and electrical transport". In: *Int. J. Heat Mass Transfer* 47.10–11 (2004), pp. 2417–2435. ISSN: 0017-9310. DOI: 10.1016/j.ijheatmasstransfer.2003.11.024.

[31] Bengt Aurivillius. "The crystal structures of two forms of barium bismuth sulfide $BaBi_2S_4$". In: *Acta Chem. Scand.* 37.5 (1983), pp. 399–407.

[32] Lykourgos Iordanidis, Paul W. Brazis, Theodora Kyratsi, John Ireland, Melissa Lane, Carl R. Kannewurf, Wei Chen, Jeffrey S. Dyck, Ctirad Uher, Nishant A. Ghelani, Tim Hogan, and Mercouri G. Kanatzidis. "$A_2Bi_8Se_{13}$ (A = Rb, Cs), $CsBi_{3.67}Se_6$, and $BaBi_2Se_4$: New Ternary Semiconducting Bismuth Selenides". In: *Chem. Mater.* 13.2 (2001), pp. 622–633. ISSN: 0897-4756. DOI: 10.1021/cm000734a.

[33] C. Ecrepont, P. Lemoine, and M. Guittard. "Diagramme de phase du système SrS-Sb_2S_3". fre. In: *CR Acad. Sci. II B* 302.20 (1986), pp. 1227–1230. ISSN: 0764-4450.

[34] Ying C. Wang, Roald Hoffmann, and Francis J. DiSalvo. "Synthesis and Characterization of $SrBi_2Se_4$". In: *J. Solid State Chem.* 156.1 (2001), pp. 230–236. ISSN: 0022-4596. DOI: 10.1006/jssc.2000.8993.

[35] Gerhard Cordier, Christoph Schwidetzky, and Herbert Schäfer. "New SbS_2 strings in the $BaSb_2S_4$ structure". In: *J. Solid State Chem.* 54.1 (1984), pp. 84–88. ISSN: 0022-4596. DOI: 10.1016/0022-4596(84)90134-8.

[36] Gerhard Cordier and Herbert Schäfer. "Zur Darstellung und Kristallstruktur von $BaSb_2Se_4$". In: *Z. Naturforsch. Pt. B* 34.8 (1979), pp. 1053–1056.

[37] Jifeng Shao, Zhongheng Liu, Xiong Yao, Lei Zhang, Li Pi, Shun Tan, Changjin Zhang, and Yuheng Zhang. "Superconducting properties of $BiSe_2$-based $LaO_{1-x}F_xBiSe_2$ single crystals". en. In: *Europhys. Lett.* 107.3 (2014), p. 37006. ISSN: 0295-5075. DOI: 10.1209/0295-5075/107/37006.

[38] B. Dickens. "The bonding in red PbO". In: *Journal of Inorganic and Nuclear Chemistry* 27.7 (1965), pp. 1503–1507. ISSN: 0022-1902. DOI: 10.1016/0022-1902(65)80010-0.

[39] Anushika Athauda, Junjie Yang, Bing Li, Yoshikazu Mizuguchi, Seunghun Lee, and Despina Louca. "The Crystal Structure of Superconducting $LaO_{1-x}F_xBiS_2$". en. In: *J. Supercond. Nov. Magn.* 28.4 (2014), pp. 1255–1259. ISSN: 1557-1939, 1557-1947. DOI: 10.1007/s10948-014-2918-0.

[40] Anushika Athauda, Junjie Yang, Seunghun Lee, Yoshikazu Mizuguchi, Keita Deguchi, Yoshihiko Takano, Osuke Miura, and Despina Louca. "In-plane charge fluctuations in bismuth-sulfide superconductors". In: *Phys. Rev. B* 91.14 (2015), p. 144112. DOI: 10.1103/PhysRevB.91.144112.

[41] J. Kajitani, K. Deguchi, A. Omachi, T. Hiroi, Y. Takano, H. Takatsu, H. Kadowaki, O. Miura, and Y. Mizuguchi. "Correlation between crystal structure and superconductivity in $LaO_{0.5}F_{0.5}BiS_2$". In: *Solid State Commun.* 181 (2014), pp. 1–4. ISSN: 0038-1098. DOI: 10.1016/j.ssc.2013.11.027.

[42] Akira Miura, Masanori Nagao, Takahiro Takei, Satoshi Watauchi, Isao Tanaka, and Nobuhiro Kumada. "Crystal structures of $LaO_{1-x}F_xBiS_2$ (x 0.23, 0.46): Effect of F doping on distortion of Bi-S plane". In: *J. Solid State Chem.* 212 (2014), pp. 213–217. ISSN: 0022-4596. DOI: 10.1016/j.jssc.2014.01.035.

[43] R. D. Shannon and C. T. Prewitt. “Effective ionic radii in oxides and fluorides”. In: *Acta Crystallogr., Sect. B: Struct. Sci* 25.5 (1969), pp. 925–946. ISSN: 05677408. DOI: 10.1107/S0567740869003220.

Chapter 3

High Pressure Magnetic Susceptibility

A diamond anvil cell (DAC) is one of many varieties of devices that can apply high pressure to a sample stored within its pressure chamber. The basic operating principle is that a sample is set in a hole drilled in a small gasket in between the flat surfaces (culets) of a high quality diamonds (anvils). This forms a sample chamber with walls defined by the inner edge of the hole in the gasket, and the top and bottom are diamond culets. As the anvils advance towards each other, the gasket is compressed. The gasket material will spread as it is compressed, and slowly decrease the size of the hole. This causes the overall volume of the sample chamber to decrease, resulting in an increase in pressure.

There are many varieties of pressure cells, and can they can apply pressures up to hundreds of GPa, which is on the scale of the pressure in the outer core of the earth. The ChicagoDAC, used for the work herein, can apply pressure up to about 10 GPa using 0.8 mm culets or up to 20 GPa using 0.4 mm culets. Within

the ChicagoDAC, one of the diamonds, set in the cell body, is stationary, while the second anvil, set in the piston, moves inwards along the axis of the cell body. The advance of the piston and its anvil is achieved using a He-gas-filled bellows, or membrane, which expands to push against the piston, driving it in towards the cell body anvil.

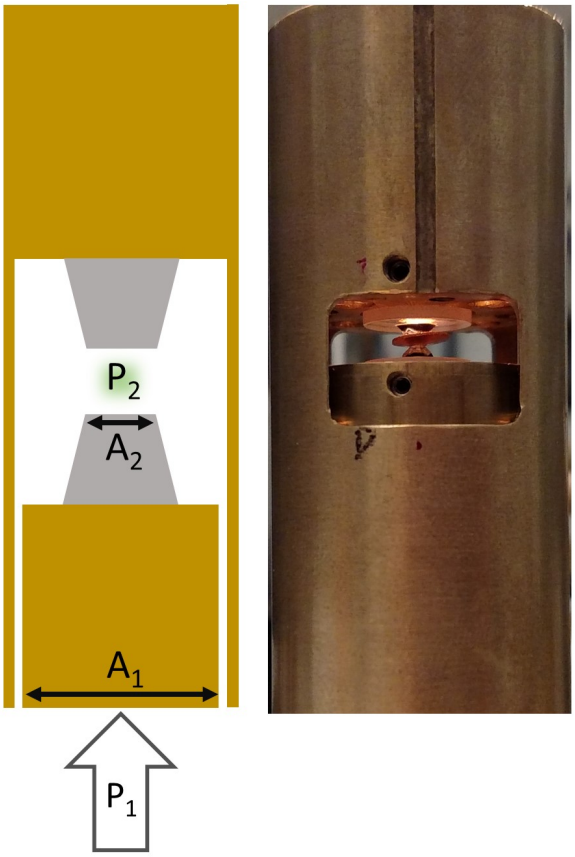

Figure 3.1: A side view of the diamond anvil cell showing a gasket pressed between two diamond anvils alongside a schematic of the pressure region of the cell. The maximum pressure increase factor is the ratio of surface area between where pressure is applied to the cell and the surface area of the sample area (culet face).

While the pressure at the sample may be extreme, the applied He gas pressure

used to expand the membrane is a few hundred times lower, usually in the range 40-140 bar gas pressure (10^{-3}-10^{-2} GPa solid pressure). The large increase can be understood from the definition of pressure, which is a force per unit area. The force applied to the piston is the same as the force applied where the culets meet, but the area of the culet face is much smaller than the area of the bottom of the piston. The maximum pressure achievable at the culet face, P_2, is given by the equation

$$P_2 = (A_1/A_2) \times P_1 \tag{3.1}$$

where A_1 and A_2 are the piston bottom area and the culet area, respectively, and P_1 is the applied pressure, as shown in Figure 3.1. The maximum scale factor (excluding external influences, A_1/A_2), from plugging in the real values of the ChicagoDAC is about 720x. In a real system, other factors, such as friction, the type of transmitting medium, and the malleability of the gasket, influence the sample pressure such that the pressure increase factor for the cell used for this work is actually closer to about 450x, based on the Pb T_C data in section 3.4.1.

The pressure cell alone does not contain the components necessary to measure any physical properties. The ChicagoDAC is designed to fit within commercially available cryostats, such as the Physical Properties Measurement System from Quantum Design, which allows for temperature control from T = 2-300 K [1]. It also has a hermetically sealed 10-pin connector with solder pins near the end of the probe, allowing for implementation of custom instrumentation. Optionally, one could use anvils with lithographically printed gold leads to perform a four-probe resistivity. Here, the DAC was adapted to measure magnetic susceptibility at high

pressures by designing a custom magnetic pick-up coil set.

3.1 Measuring Magnetic Susceptibility

When a material is subjected to an applied external magnetic field, **H**, it responds with an internal magnetization, **M** which adds to the applied field for a net internal magnetic field, **B**.

$$\mathbf{B} = \mu_0 \mathbf{H} + \mathbf{M} \tag{3.2}$$

where μ_0 is the magnetic permeability of free space. The magnetization, **M** is related to the applied field by the magnetic susceptibility, χ

$$\mathbf{M} = \chi \mathbf{H} \tag{3.3}$$

The sign and magnitude of χ is material-dependent and spans orders of magnitude between the weak response of a traditional diamagnet and the strong response of a ferromagnet, which is discussed in Chapter 1. For a superconductor below its transition temperature, $\chi = -1$ in dimensionless CGS units so that $\mathbf{M} = -\mathbf{H}$, with the important consequence that the internal magnetic field $\mathbf{B} = 0$. The value of χ in SI units carries a 4π conversion factor from CGS units so that $\chi^{SI} = 4\pi\chi^{CGS}$. The physical shape of the sample can introduce demagnetization effects that force χ to deviate from the ideal value. This is because the magnetic field lines must bend around the sample, which becomes impossible when the sample has sharp angles or a similar feature [2].

The excitation field for a typical magnetization or susceptibility measurement ($\mathbf{B}_{exc}$) is applied using a solenoid (drive coil). The small response field ($\mathbf{B}_s$) produced by the sample can be measured using a second solenoid (pick-up coil) located very close to the sample. The sample's response field will result in an electrical signal within the pick up coil according to Faraday's law

$$\epsilon = -\frac{\partial \phi}{\partial t} \tag{3.4}$$

where ϵ is the electromotive force, ϕ is magnetic flux, and t is time. By assuming a constant area, the magnetic flux can be assumed equivalent to B and the ϵ equivalent to voltage V, which results in a voltage across the pick-up coil

$$V = -\frac{\partial B}{\partial t} \tag{3.5}$$

that is easily measurable as long as the magnetic field is changing with time. This can be accomplished by providing an alternating current (AC) through the drive coil to generate an AC excitation field and an AC sample response. For ambient pressure measurements, a DC field can be applied, and the sample can be moved within the pick-up coil to produce a time-varying response. The magnitude of the current generated by the voltage across the pick-up coil is dependent on the coil properties, according to the equation

$$B = \mu_0 \frac{N}{l} I \tag{3.6}$$

where N is the number of turns of wire in the coil, l is the length of coil along

its axis, and I is the current through the wire. This equation also describes the field applied by the drive coil, which is controlled through the current.

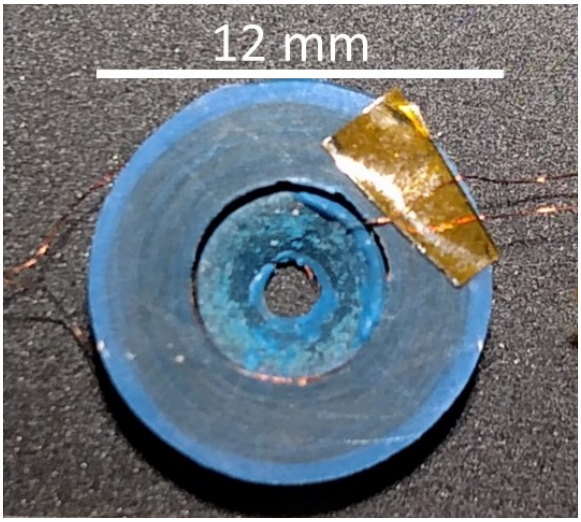

Figure 3.2: The measurement coil set, with the pick-up coil nested inside of the roughly 12 mm drive coil.

The measurement coil set is shown in Figure 3.2. The sample lies in the center of the pick-up coil, which is in turn nested in the center of the drive coil. This set-up puts the sample at the center of the drive coil's field, where the magnetic field lines are most uniform and the field is the strongest. The pick-up coil is designed to be as closed to the sample as possible, to maximize the signal it receives from the magnetic field of the sample.

While this is optimal to measure the sample response, a secondary effect of this set-up is that the excitation field is also producing a response in the pick-up coil. The signal from the excitation field is about 10 million times stronger than the signal from most samples, making it impossible to detect the sample signal at all without very specialized equipment. The simple solution is to use a compensating

coil set, where the two drive coils are wired in series within the same circuit, and the two pick-up coils are in series in their own circuit separate from the drive circuit. The compensation field should be oriented opposite the excitation field across the compensating pick-up coil to produce a negative current. Since the pick-up coils are wound in series, if the current from the compensating field is equal to the current from the excitation field, then the total current in the pick-up circuit should be entirely produced by the sample, as shown in equation 3.7.

$$I_{pick-up} = I_{sample} + I_{excitation} - I_{compensation} \tag{3.7}$$

Ideally, the compensating coil set would be identical to the measurement coil set and located as close as possible to the measurement set, to eliminate environmental difference. Due to the size constraints within the DAC, this is not possible. Instead, the compensating coil set is external to the system, and is designed to be able to overcompensate for the background field. To achieve optimal compensation, the compensating pick-up coil can be moved in and out of the compensating drive coil to find the best field-match (since the field density varies in space). This technique has been used for a variety of systems, and is known as gradiometric mutual inductance [1, 3].

3.1.1 Winding small solenoids

The two coil sets (measurement and compensation) required four different coil types. The measurement set needed to be small enough to fit inside the DAC, but it was more practical to make the compensation set larger and encased in

PTFE for ease of handling. The measurement coils were wound into molds that were designed to come apart, so that the coil could be removed from the mold. To maintain the structure of these coils, industrial epoxy (Stycast 2850, Catalyst 11) was applied to the wire as it was fed into the mold, after it passed through an alignment nozzle. The molds for the measurement coil set were designed to fit into the 1/4" collet on the lathe spindle. The compensation coils were wound into permanent coil forms which were machined out of PTFE. The dimensions of the forms and molds are given in Figure 3.3. The measurement coil molds were machined out of Delrin by professional machinists. The compensation coil forms were first machined out of PTFE stock, then later 3D printed out of ABS-M30.

Both sets of coils were initially wound using the lathe. The lathe set-up is shown in Figure 3.4. The spool mount was bolted into the tool holder on the lathe, the alignment nozzle was secured in the tool mount, and the coil mold was tightened into the spindle using a collet. The wire was fed through the alignment nozzle, then wound twice into the coil mold by hand, by looping over the top of the inner cylinder, then secured to the outside body of the mold using tape. The lathe was run in reverse mode at a rate of about 60-75 rpm. The rate was chosen so that the force from acceleration was not sufficient to break the 25 μm wire. The number of turns can be measured using a turn counter with a rubber stopper that fits into the back opening of the spindle, or calculated from the time spent winding multiplied by the turn rate. Coils for the compensation set were wound into the PTFE forms without epoxy using the same method.

Later compensation coils were wound using the 200 mm CNC Coil Winding

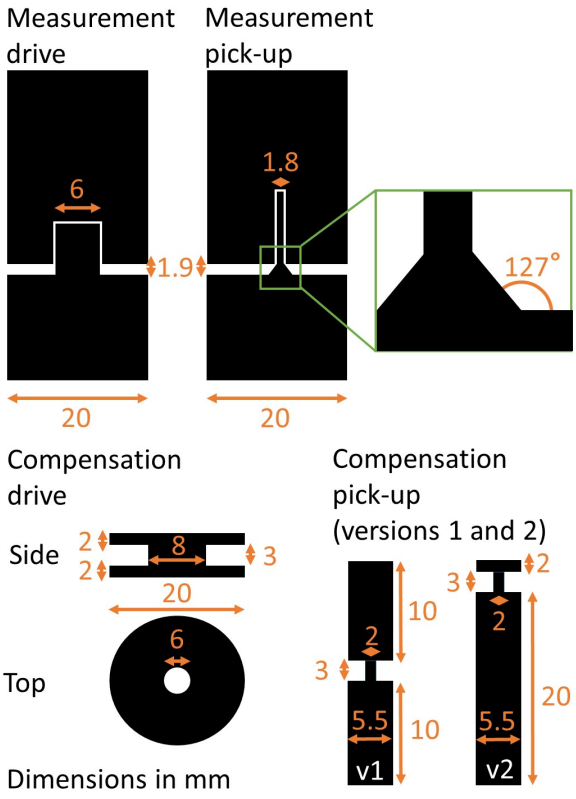

Figure 3.3: The dimensions of the measurement coil set molds and compensation coil set forms given in mm.

Machine. The compensation pick-up coils were designed to fit inside the CNC winder's 6 mm collet. The larger compensation drive coils were wound by securing a 1/4-20 threaded rod in the collet, then sandwiching the drive coil between two 1/4-20 nuts with washers. The turn rate was still 60-75 rpm. The CNC winder has the capability to set winding pitch for close, even wire packing, though this has not yet been adjusted for truly even coils.

After the coils have cured, the molds can be pulled apart for access to the coil. Removing the epoxied coils from the mold without damaging the sensitive wire

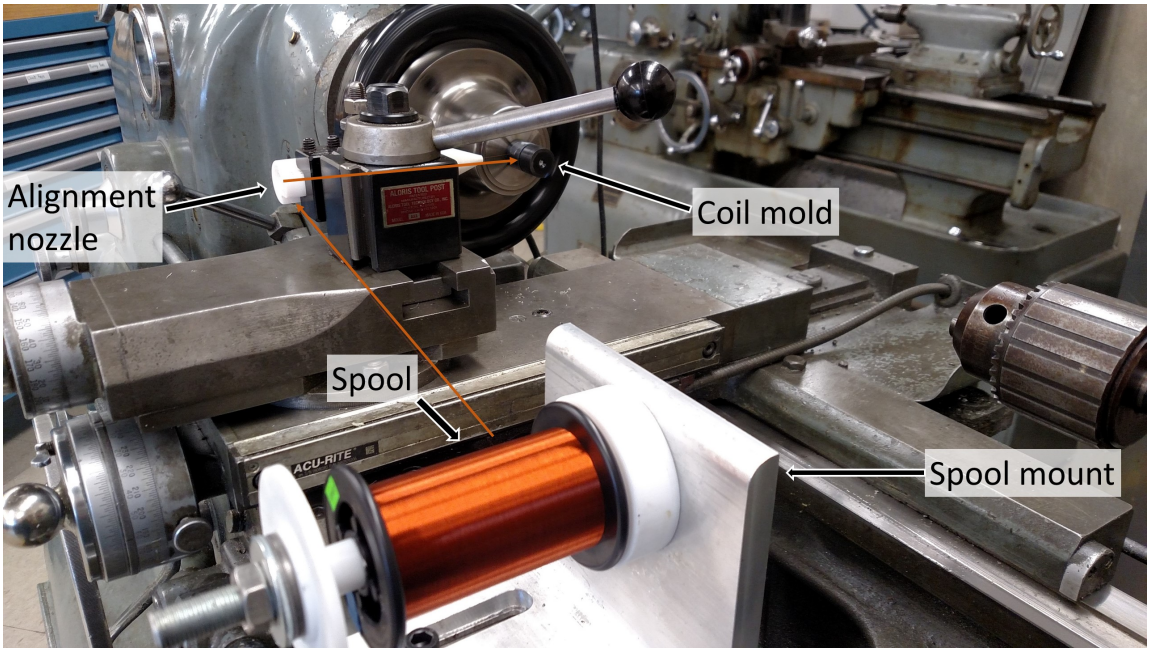

Figure 3.4: The coil winding set-up in the lathe, shown here with the mold for a measurement drive coil. Black and white arrows point to individual parts of the set up, and the orange arrows follow the path of the copper wire from the spool into the coil mold.

was particularly challenging. The molds were designed to pull apart easily, which they do with a gentle twist, but this leaves the coil adhered to one side without anything to grip it by. Care must be taken during this stage to ensure the wire is not broken. The coil can be salvaged if outer turns are damaged by attaching a lead to the exposed, broken wire which will likely result in at most the loss of 20 turns of wire (roughly the number of turns in one layer). Damage to the inner turns renders the coil useless.

Using a very thin layer of mounting wax to the flat surfaces of the mold helped keep the epoxy loose, though if too much was applied, it embedded in the epoxy and weakened the coils. For this reason, it should not be used on the inner peg

of the mold. Rather, a piece of straw cut to size and stretched to fit over the peg keeps the inner surface of the coil loose from the mold, and the straw piece can be removed (if desired) easily with tweezers.

A possible alternative to the use of the two-part coil molds is to use a 3D printed coil forms with thin support walls. The printing material is soluble in acetone, so the coils can be wound using epoxy, cured, then the forms dissolved.

3.2 BNK3R Description and Set-up

The magnetic susceptibility measurement instrument, lovingly named BNK3R, consists of a lock-in amplifier (SR830), an FET-based pre-amplifier (SR560), and three aluminum boxes that provide electric shielding to external components and provide a junction between small wires and BNC-type coaxial cables. The reference signal generator on the lock-in serves as a voltage-controlled, AC power supply that generates the current in the drive coil set. The PPMS resistivity option is used to collect 4-probe resistance data on a calibrated Cernox thermometer.

Solder pins at the bottom of the DAC insert connect to wires that are fed to atmosphere through a hermetic feedthrough. The pins on the atmospheric side of the feedthrough are soldered to the individual wires of a standard CAT 6 network cable, which consists of four twisted pairs inside of grounded metal shielding. The two measurement coils are connected to the pins at the bottom of the DAC insert through small two-connection plugs that are soldered onto the insert pins and the coil wires separately to allow easy connection and disconnection. The four Cernox

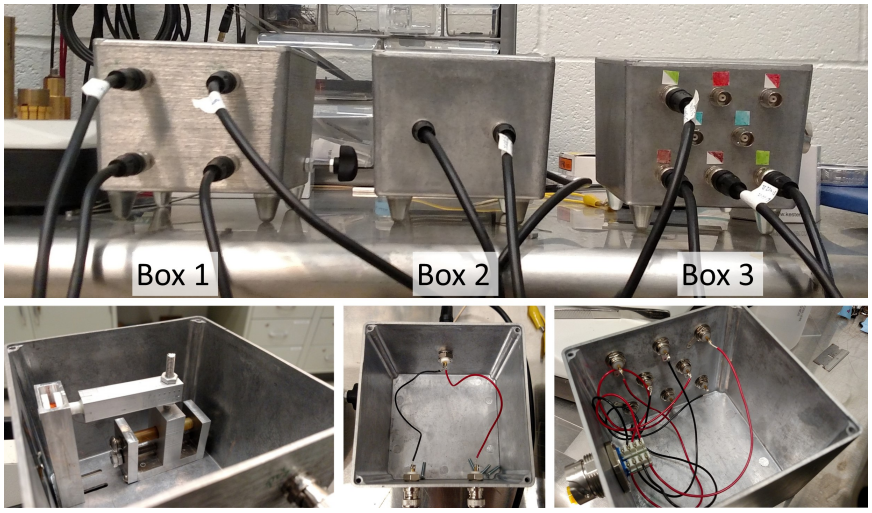

Figure 3.5: The box components of BNK3R. Box 1 contains the compensating coil set, Box 2 splits the single-ended output from the lock-in amplifier into an input for each end of the drive circuit, and Box 3 takes the network cable from the DAC insert and splits its component wires into 8 BNC jacks.

thermometer lead wires are soldered to extension wires for extra length, and those are soldered directly to the insert pins.

The network cable is connected to Box 3 via an RJ45 adapter that leads to a printed circuit board with a solder port for each of the eight composite wires and one for ground. The eight solder ports are wired to eight labeled BNC jacks, which can then be connected to whichever device they need.

Measurement across the pick-up coil circuit is done as a differential measurement without reference to ground. The typical filter and gain settings for a measurement of T_c are shown in Table 3.1.

SR560 pre-amplifier	
High pass	300 Hz, 6 dB/oct
Low pass	1000 Hz, 6 dB/oct
Gain	1000 x
Gain mode	low noise
Coupling	AC, A
SR830 Lock-in amplifier	
Time constant	10 s
Sensitivity	50 mV
Slope	12 dB/oct
Signal input	A/I, AC, GRND
Reserve	Normal
Filters	Line, 2x Line
Channel 1	X
Channel 2	Y
SR830 Signal Generator	
Signal form	Sine
Reference	Internal
Amplitude	800 mV
Frequency	750 Hz
Phase shift	0

Table 3.1: SR830 and SR560 measurement settings

3.2.1 Interpreting Data

A brief discussion of AC current and voltage relationships is necessary in order to understand the data output from BNK3R, which is the measured voltage in Channel 2 (Y component) of the lock-in. In a DC circuit, the voltage is directly related to the current through resistance. In an AC circuit, pure resistance has the same affect as in a DC circuit, but capacitance and inductance have a time-dependence, causing a lag or lead in the voltage response to current. The voltage relates to the current through complex impedance

$$V(t) = I(t)Z \tag{3.8}$$

where the impedance Z in Cartesian form is given by

$$Z = R + j(X_L + X_C) \tag{3.9}$$

X_C and X_L are the capacitive and inductive reactance, respectively, and j is the imaginary number. Both the capacitive and inductive reactance have a frequency component

$$X_L = 2\pi f L \tag{3.10}$$

$$X_C = \frac{-1}{2\pi f C} \tag{3.11}$$

where f is the frequency, and L and C are the total inductance and capacitance,

respectively. Because of the form of impedance, if the voltage current relationship is expressed in Cartesian form as above, the real component of the voltage vector lies along x and the imaginary component lies along y, which are directly output by the lock-in amplifier in Channel 1 (x) and Channel 2 (y). For measuring magnetic susceptibility, the Channel 1 output can be largely ignored (although phase shifts in the voltage may put some portion of the imaginary component in x), and the Channel 2 data are taken to be the sum of capacitance and inductance, but dominated by inductance because the the circuit is primarily composed of two series inductors. The frequency used for measurement is relatively high - 750 Hz - to minimize the capacitive contribution to the signal. If the exact values of C and L were known, and optimal frequency could be caluclated. It is worth noting that while the BNC coaxial cables provide excellent shielding against stray signals, they introduce a capacitive component that is proportional to the cable length and acts as a capacitance to ground. However, the use of differential measurement at the pre-amp should reduce any deleterious effect.

3.3 General Measurement Procedure

Before a measurement begins, the cell must be made ready. The manual for the ChicagoDAC has general guidelines for how to assemble the cell without real detail. The specific procedure for preparing the cell itself, adding the sample and coils, and then running a measurement at cryogenic temperatures under pressure are described in this section along with a few problems and their solutions.

The sample was loaded in the cell in stages: (1) preparing the diamond anvils,

(2) stabilizing the gasket, (3) preparing and adding the sample, (4) placing the coils and sealing the cell. It took many attempts to get the process working correctly. Some of the major obstacles are described below, along with the solutions and overall process that works consistently.

3.3.1 Preparing the Diamond Anvils

The culets of the diamond anvils must be cleaned thoroughly to ensure the success of the experiment. Debris on the culet may interfere with the signal, break the seal between culet and gasket to allow the transmitting medium out, or mar the culet surface. Cleaning can be done with a Kim-wipe or cotton tipped applicator and ethanol until there are no smudges or debris visible under a microscope.

The inner walls of the cell body and the sides of the piston need to be cleaned to the same level. The piston will only move freely in the body if there is nothing providing undue friction, including oils from skin and small bits of dust. Once the piston has been cleaned, it should be handled only with gloves. Touching of the sides should be minimized (or avoided entirely if possible). The bolts can be threaded in to the two 4-40 threaded holes in the bottom of the piston, and these can be used to handle the piston as needed. While greasing the piston does make loading the cell easier, at cryogenic temperatures, the viscosity of the grease prevents the bellows from moving the piston, which makes it impossible to change the sample pressure.

At this stage, once the culets are free of foreign objects, it can be helpful to add a very thin layer of mounting wax to the cell body diamond, which will help

secure the sample during later stages of the process. There should not be so much wax as to occupy any significant volume of the gasket opening, which would change the pressure of the cell in uncharacterized ways. This step just provides the smallest adhesion necessary to keep the tiny sample in place, particularly when the transmitting medium is added.

3.3.2 Stabilizing the Gasket

The indentation in the gasket allows it to rest centered on the culet without any advanced centering procedure, but it is still vulnerable to small bumps and disturbances. Two very small beads of tacky putty placed on either side of the diamond base, where it is pasted to the sapphire seat, can help fortify the gasket. Without the putty, it is incredibly difficult or impossible to place the coil set in the cell without toppling the gasket (indeed, if the gasket is not perfectly symmetric, it may not hold itself up even without the coils). The beads of putty should be as small as possible, so that they do not lift the gasket up above the culet, which would cause the transmitting medium to leak out before the cell is sealed.

3.3.3 Preparing and Adding the sample

The sample size should be no more than 50% of the volume of the chamber formed by the gasket hole and the culets. For 800 μm culets, the gasket hole diameter is between 300 and 400 μm and the depth is about around 100 μm. The sample volume should be around 0.013 mm^3, which necessitates the use of a microscope.

Any surface oxidation or impurity should be removed, then the sample should

be cut to size using a razor blade. To check the size, a second gasket can be placed on the cutting surface with the sample, and the size can be check visually using the gasket hole as a reference. The ideal sample will have enough room on either side that there will still be a ring of space between the sample and the gasket even after the gasket hole has contracted under applied pressure.

Once the sample is cut to size, it can be placed inside the cavity in the mounted gasket in the cell carefully. It should be pressed gently into the wax on the culet (if it was used), centered in the cavity as much as possible.

For samples with an unknown pressure dependence, it may be necessary to add Pb as an internal standard along with the sample itself. The pressure dependence of the superconducting transition temperature of lead is linear and well-studied, allowing it to act as a manometer for cell pressure. In this case, the combined volume of sample and lead should be less than or equal to 50% the chamber volume. Empirically, the volume ratio between the two should be about 2:1 sample to Pb. Any smaller and one or the other, and the signal will be too small to distinguish with certainty. Since the behavior of Pb is so well-known, even a small signal is distinguishable, so it is acceptable for Pb to be only half the size of the sample.

3.3.4 Placing the Coils and Sealing the Cell

With the sample and gasket in place, two of the coil set lead wires (one pair from one coil) should be fed in carefully to avoid tipping the gasket with the wires. Once the wires are through, the coil set can be placed gently on the gasket. The putty

under the gasket should keep everything in place as long as the lead wires sticking out of the cell are not jostled.

At this stage, the sample area is finished, and the piston should be inserted and aligned. Alignment in this stage is critical. The diamonds should have been centered with each other previously using the set screws, and they will only be centered for the right orientation of the piston, which should be marked. With the piston bottom flush with the cell body opening, the 4-40 screws can be used to rotate the piston as needed for alignment, then a metal cylinder just a little smaller in diameter than the piston can be used to push the piston further into the cell. When the piston diamond is visible through the window about 5 mm above the coil set, the pressure transmitting medium can be added using a syringe.

The pressure transmitting medium for the experiments discussed in this thesis was a 4:1 mixture of methanol to ethanol. About one drop of it was added to the indentation of the gasket, which was more than enough to fill the chamber. The sample may be lifted out of the chamber at this stage due to the forces exerted by the medium. This can be mitigated with a small bit of wax as discussed, but the medium should still be added gently, and a minimal amount should be used.

With the medium in place, the piston can be pressed, gently, all the way until it makes contact with the gasket. The four 6-32 by 32 mm bolts with compression washers should be threaded in loosely, careful to avoid the lead wires. When all four are in place, they should be tightened each a little bit at a time working in a cross pattern so that there is no dramatic pressure differently across the culets. The should be tightened enough that there is resistance to turning further, but not

wrenched in place. Too tight will apply a significant pressure to the sample, as will be discussed in the analysis of the Pb measurement. Too little pressure will not seal the transmitting medium in the cell.

3.3.5 Other Preparation Steps and Experimental Procedure

Before the system is cooled for a measurement, the capillary should be connected to the pressure controller and purged. This should be done even for calibration experiments without the application of pressure. The capillary feeding into the membrane is not capped, so air will condense in the membrane if it is left unconnected during cooling. Purging can be done by simply applying a small pressure (i.e. 2 atm), then releasing the pressure by setting the applied pressure to 0 atm, then repeating *ad nauseam* (i.e. 20 times).

Between pressure measurements, it may be necessary to re-align the diamonds. If the diamonds are already adhered to the seats, then the piston diamond should be centered over the viewport that runs through the piston first. This is done by adjusting each of the four set screws that hold the seat in place in small amounts until the diamond looks visually centered when looking from above with a uniaxial microscope. The cell body diamond and seat should be loosely secured with the set screws, then the piston (with diamond and seat) should be lowered until the two diamonds are almost touching. The cell body seat set screws should be adjusted until the two diamonds are perfectly concentric, which can be judged from the small eclipse-shaped ring that appears if they are not aligned.

For best results, and to extend the lifetime of the diamonds, the piston and

body diamonds should also be perfectly parallel along the face with respect to each other. This should happen naturally since the seat face and diamond bottom are both cut to precision, but small deviations arise if the epoxy material wicks up under the diamond when it is being adhered to the seat. The angle between culets can be checked visually by bringing the two diamonds together in the cell until they are just touching, but with no force applied. This should be done very carefully to avoid damaging the diamonds or the seats. If they are perfectly flat, white light should transmit straight through. If there is a small angle, the light will interfere with itself as it passed through the angled gap, producing a gentle rainbow across the diamond face. If the angle is larger, it will produce a striped pattern of rainbows.

3.4 Measurements

Data was collected first on Pb as proof that BNK3R was capable of measuring T_c and that the cell was set up correctly for the application of pressure. The next set of experiments was on a Tl_5Te_3, which had been heavily characterized at ambient pressure by a previous graduate student, Kathryn Arpino. The final measurement was on $Sr_2O_2Bi_2Se_3$, which was discovered, characterized, and reported as discussed in Chapter 2. Data for the following measurements was collected by manually recording the digital output from the lock-in amplifier's Channel 1 and Channel 2 display. Testing of a control program written in LabView is underway, and the program front panel and block diagram are shown in Appendix A.

3.4.1 Cell Test with Pb

The data for the first successful pressure measurement on lead is shown in 3.6. The data shown is only for the Y component of the AC voltage. There are several features of the data which are due to the experimental set up and are informative for optimizing future measurements. First is the prominent sloped background present in the 2 bar data set, which is less apparent at higher pressures. This feature is not actually related to the pressure within the cell, but is actually representative of the thermal equilibration of the cell and the warm-up period of the measurement electronics. It is difficult to disentangle the two effects, but in all measurements it has been observed the the background slope and overall noise decreases as a function of how long the cell has been cryogenic.

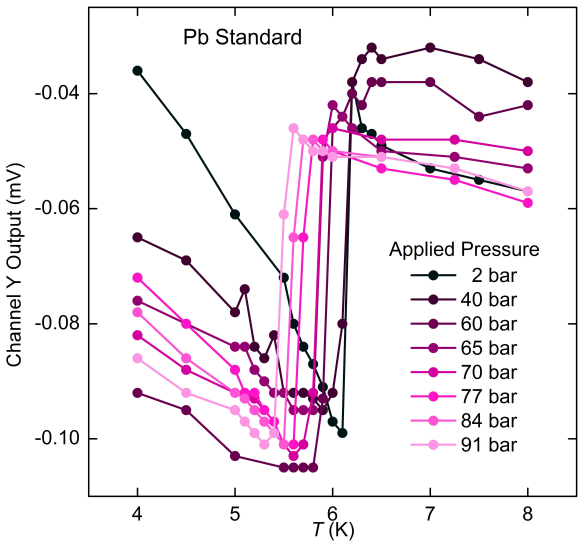

Figure 3.6: Magnetic susceptibility of Pb measured as a function of temperature using BNK3R collected at several different applied gas pressures in the diamond anvil cell, clearly showing the expected change in T_C.

At both 2 bar and 40 bar, the transition occured at 6.1 K as opposed to the true ambient pressure T_c of pure lead, which is 7.2 K. The three most reasonable causes for this were that (1) the sample was impure, (2) the PPMS thermometer was not representative of the cell temperature due to limitations of thermal conductivity, and (3) that the cell was under pressure before changing the applied He gas pressure.

To test the purity of the Pb, a small piece was cut from the same boule and prepared in the same way (surface shaved until shiny) and measured using the PPMS's AC measurement system (ACMS) option, which showed the transition at the expected 7.2 K. To test whether the PPMS thermometer matched the cell temperature and eliminate the possibility of pressure from sample preparation, a measurement of Pb was taken using BNK3R and the cell fully assembled but without the gasket. The piston was brought close enough to hold the coils in place, and a small (but much larger than a pressure sample) piece of Pb was held in place on the culet using a piece of putty. The results are plotted together in Figure 3.7.

The results of the ambient pressure test in BNK3R demonstrate that it is capable of reproducing the data collected on a commercial instrument, even without digitalized data collection. The large background is far less noticeable in this data because the size of the transition is so much larger in comparison, though a slight upturn with decreasing temperature is visible between 6 K and 4 K, which is likely the paramagnetic contribution of the cell components. Further, the tests show that the Pb sample is pure and that it is possible to apply up to about 2.5 GPa using just the screws with compression washers. This is not unexpected, given that there are

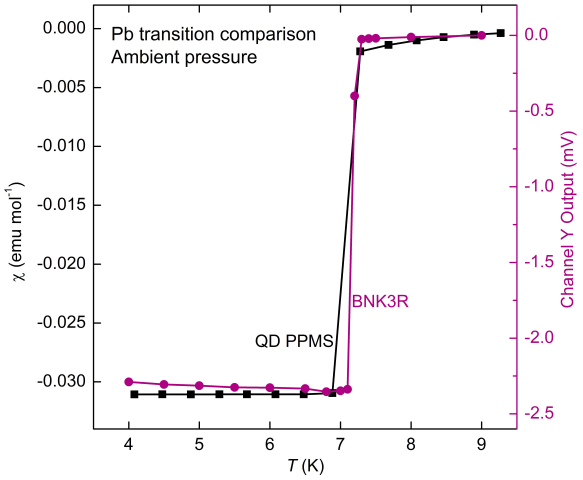

Figure 3.7: Ambient pressure susceptiblity test using BNK3R, data in pink, as compared to data collected on a piece cut from the same sample measured using the commercial ACMS option of the PPMS.

a variety of diamond anvil cells that use only screws rather than a gas member to apply pressure.

Plotting the transition temperature against the applied gas pressure from figure 3.6 gives the plot shown in figure 3.8. From 2 to 40 K, the pressure in the cell had not begun to respond to the pressure applied by the membrane, which reflects the factory test results of the cell. Between 60 and 90 bar applied pressure, the trend is approximately linear with the exceptation that the cell pressure apparently did not change between 65 and 70 bar applied pressure. For the data collected between 2 and 70 bar in this experiment, the pressure was changed after the cell had been left at 30 K for half an hour, to reduce the viscosity of helium in the capillary. It is suspected that at 65 bar and 30 K, helium is too sluggish to change the pressure on the timescale of the experiment. Moving forward, the pressure was changed after a 30 min dwell at 40 K instead of the 30 K.

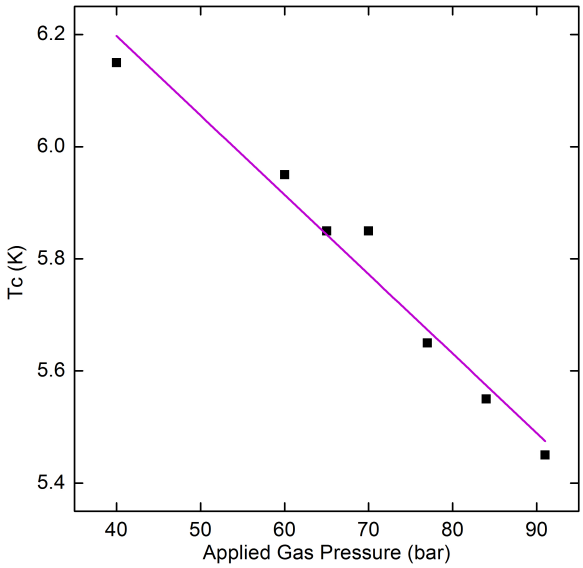

Figure 3.8: Pb T_C versus applied gas pressure for the pressure range 40 to 92 bar, where the change in gas pressure was observed to result in a change in cell pressure. The purple line is a linear fit to the data to highlight the trend.

3.4.2 Tl_5Te_3

Tl_5Te_3 is a candidate topological superconductor that was thoroughly characterized by a former McQueen lab student in Refs [4, 5]. The coincidence of topological surface states and superconductivity posed an interesting platform to study the effects of pressure.

For this measurement, Pb was included along with the Tl_5Te_3 sample to act as an internal manometer. The pressure could not be changed using the membrane, which can be seen in Figure 3.9 as a lack of response from Pb with increasing applied gas pressure up to 85 bar. While the reason for this was not apparent at the time, after further investigation, the likely cause was the use of N-grease on the piston. Thorough cleaning of the cell allowed for use of the bellows in the next

experiment, discussed in Section 3.5. For the present experiment, the pressure was changed by warming the cell up to room temperature and tightening the screws that secure the piston in the cell body, which had the effect discussed in Section 3.4.1.

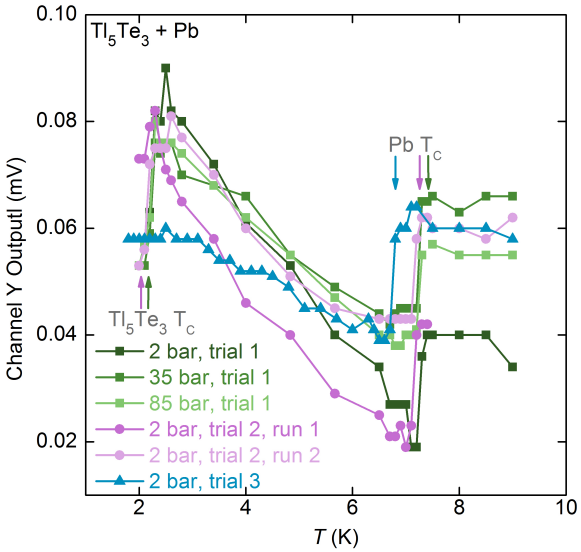

Figure 3.9: The magnetic susceptibility data as a function of temperature in the pressure range 0–1.5 GPa. Data from the first trial is in shades of green, data from the second trial shown in shades of purple, and the third trial shown in blue. The superconducting transitions for Pb and Tl_5Te_3, separately, are marked with arrows colored to match the trial number. Trial 3 data showed no transtion for Tl_5Te_3.

The rough method of changing pressure, which prevented fine tuning of the pressure, combined with the low ambient pressure T_c of Tl_5Te_3 of 2.3 K made it difficult to capture enough data points for a really thorough trend. However, it is apparent as pressure increases, T_c decreases at approximately 0.2 K/GPa.

Band structure calculations using Elk were done including spin orbit coupling and a U of -5 eV for pure Tl_5Te_3 using the ambient pressure cell parameters

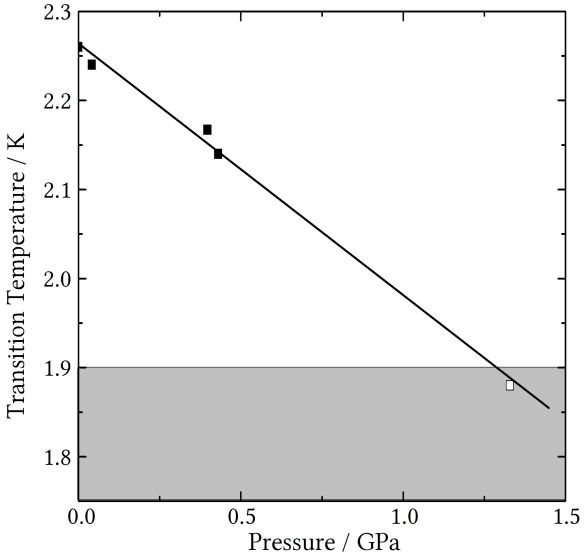

Figure 3.10: Plot showing the decrease in Tl_5Te_3 T_C as a function of applied pressure determined from the T_C of the internal Pb standard.

as well as with cell volume reduced by 1%, 2%, and 3% to simulate applied hydrostatic pressure. The cell volume was decreased by decreasing the *a* and *c* lattice parameters in a 1:3 ratio (i.e. *c* was decreased by three times the amount *a* was decreased) to reflect the empirical changes in lattice parameter upon doping with Sn. The band dispersion increased considerably with small changes in lattice parameter, as expected. There are no noticeable changes in the shape of individual bands which would suggest a change in bonding environment. The observed loss of superconductivity may be due to a decrease in the density of states at the Fermi level [6].

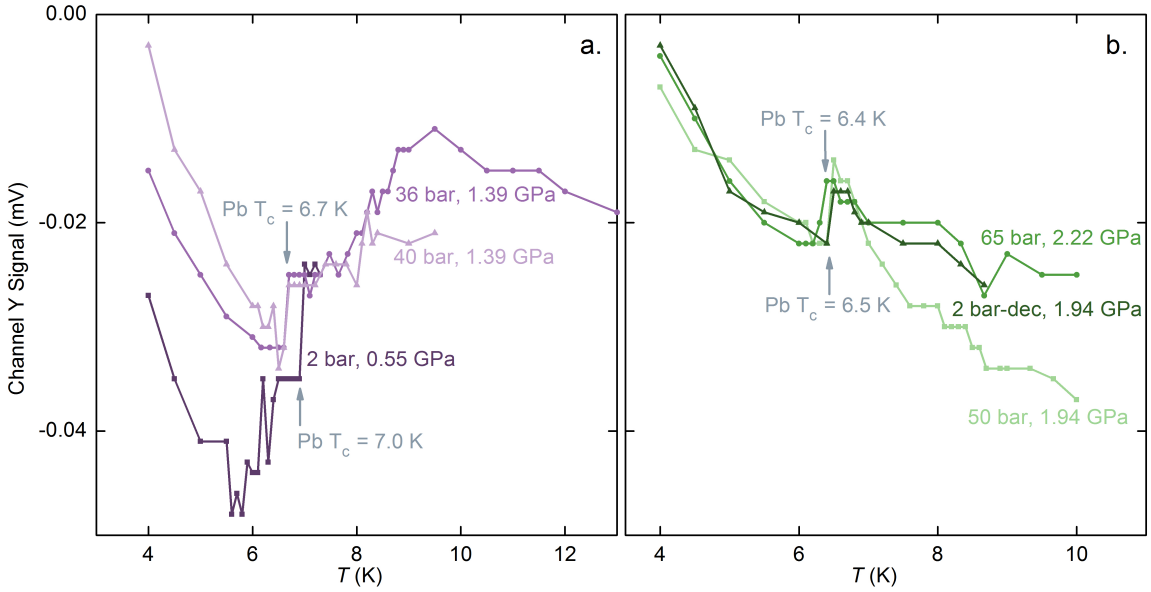

Figure 3.11: Magnetic susceptibility respone under applied pressure for one measurement on $Sr_2O_2Bi_2Se_3$ with a Pb internal standard. The lower (**a**) and higher (**b**) pressure data sets are separated into two panels for clarity to highlight the presence of an unusual slope near the Pb transition in **a** which is not visible in **b**. 2 bar-dec is the measurement taken when all but 2 bar of gas pressure was released from the membrane to allow the gasket to relax as much as possible.

3.5 $Sr_2O_2Bi_2Se_3$

As discussed in Chapter 2, $Sr_2O_2Bi_2Se_3$ is a small band gap semiconductor which is intrinsically electron doped due to selenium vacancies that result from vaporization of Se during synthesis. The crystal structure of $Sr_2O_2Bi_2Se_3$ is similar to that of the bismuth sulfide superconductors, but rather than 2D planes of BiS_5 square pyramids, it has 1D strips of $BiSe_4O$ square pyramids. Both iron arsenide SCs and cuprates SCs, which are 2D structues, have 1D analogues that superconduct under applied pressure. This provided motivation to study $Sr_2O_2Bi_2Se_3$ and others in the family under pressure as well.

The results of the pressure experiment on $Sr_2O_2Bi_2Se_3$ are shown in Figure 3.11 **a** and **b**. A Pb internal standard was used to measure pressure assuming dT_C/dP = -0.39 K/GPa [7]. There are two features in the data. The first is the prominent Pb SC transition at around T = 7 K and decreasing with pressure to T = 6.4 K, which is visible in all data sets. The second is the jagged slope that increases with increasing temperature and is only apparent in the lower pressure data shown in Figure 3.11 **a**. In the P = 0.55 GPa data set, in dark purple, the feature begins at $T = 5.8$ K and overlaps with the Pb T_c at $T = 7$ K. In the 1.39 GPa data sets, medium and light purple, corresponding to two different applied pressures and collected hours apart, the features begins just above the Pb transition at $T = 6.7$ K and stops at $T = 9$ K where it resumes the negative slope of a Curie tail.

Data collected at higher pressure do not show this feature at all, which could mean one of a few things. The first is that it was a fluke of the experiment, which seems unlikely as the feature persisted over time and showed at the same temperature during other measurements (not shown) collected at 1.39 GPa and 36 bar applied pressure. The second is that whatever physical property gave rise to the feature was terminated by the increase in pressure. The third is that the feature moved to a temperature that was out of range of the collected data, i.e. $T < 4$ or $T > 10$ K.

Without cleaner data, it is hard to make any real claims about what could cause the unusual slope that seems to change onset temperature with pressure. It is not out of the realm of possibility that it is caused by a Type II superconducting transition, which do not always show the discontinuous drop in susceptibility at T_c

seen in Type I superconductors. Other forms of magnetic order are unlikely given that $Sr_2O_2Bi_2Se_3$ contains no magnetic ions and showed no measurable magnetic response at ambient pressure when measured with the Quantum Design ACMS option.

References

[1] Yejun Feng, D. M. Silevitch, and T. F. Rosenbaum. "A compact bellows-driven diamond anvil cell for high-pressure, low-temperature magnetic measurements". In: *Review of Scientific Instruments* 85.3 (2014), p. 033901. ISSN: 0034-6748. DOI: 10.1063/1.4867078.

[2] Kristian Fossheim and Asle Sudbo. *Superconductivity: Physics and Applications*. Wiley, 2005. ISBN: 978-0-470-84452-6.

[3] J. S. Schilling, J. Diederichs, S. Klotz, and R. Sieburger. "Ac Susceptibility Studies of Superconducting Properties Under High Hydrostatic Pressure". en. In: *Magnetic Susceptibility of Superconductors and Other Spin Systems*. Springer, Boston, MA, 1991, pp. 107–128. ISBN: 978-1-4899-2381-3 978-1-4899-2379-0. DOI: 10.1007/978-1-4899-2379-0_5.

[4] K. E. Arpino, D. C. Wallace, Y. F. Nie, T. Birol, P. D. C. King, S. Chatterjee, M. Uchida, S. M. Koohpayeh, J.-J. Wen, K. Page, C. J. Fennie, K. M. Shen, and T. M. McQueen. "Evidence for Topologically Protected Surface States and a Superconducting Phase in $Tl_4Tl_{1-x}Sn_xTe_3$ Using Photoemission, Specific Heat, and Magnetization Measurements, and Density Functional Theory". In: *Phys. Rev. Lett.* 112.1 (2014), p. 017002. DOI: 10.1103/PhysRevLett.112.017002.

[5] K. E. Arpino, B. D. Wasser, and T. M. McQueen. "Superconducting dome and crossover to an insulating state in $[Tl_4]Tl_{1=x}Sn_xTe_3$". In: *APL Materials* 3.4 (2015), p. 041507. ISSN: 2166-532X. DOI: 10.1063/1.4913392.

[6] B. Lorenz and C. W. Chu. "High Pressure Effects on Superconductivity". In: *arXiv:cond-mat/0410367* (2005), pp. 459–497. DOI: 10.1007/3-540-27294-1_12.

[7] M. J. Clark and T. F. Smith. “Pressure dependence of T_C for lead”. en. In: *J Low Temp Phys* 32.3-4 (1978), pp. 495–503. ISSN: 0022-2291, 1573-7357. DOI: 10.1007/BF00117966.

Chapter 4

Crystal growth by design in Cu_2OSeO_3

Cu_2OSeO_3 is a material that is best known in physics because of its rare combination of magnetic and electric properties: it is one of the only known insulating materials to harbor skyrmion magnetic ordering. There are many scientists pursuing a deeper understanding of skyrmion physics, and Cu_2OSeO_3 provides a unique environment in which to study those physics, but growing large single crystals that are free of impurities is, as in many cases, challenging and requires a nuanced understanding of the its chemistry under crystal growth conditions[1–6]. Under the growth conditions discussed in this chapter, Cu_2OSeO_3 forms large (mm-scale) crystals with clearly defined faces. The form of the crystals was used to understand the extract information about the surface energy of a few relevant crystallographic planes using a Wulff construction [7].

Cu_2OSeO_3 exists in a family of materials including $CuSeO_3$ and $Cu_4O(SeO_3)_3$, which all differ in the ratio of CuO:SeO_2 and are formed under very similar growth

conditions [8–11]. The similarity in formula and synthesis method posed a challenge to growing pure single crystals of just the desired Cu_2OSeO_3 phase, since the phases could intermix during the growth with small changes in the growth conditions (i.e. as the vapor-phase species change ratio following condensation, etc).

4.1 Crystal Forms and Surface Energy

As crystals grow, they take a form that allows them to minimize their free energy in the growth environment. A solid particle nucleating out of a medium has a higher energy at the interface between the particle and the medium. The free energy of a particle with interfacial area A becomes

$$G = G_0 + A\gamma \tag{4.1}$$

where G is Gibbs free energy, G_0 is the free energy assuming the whole particle has properties of the bulk material, and γ is the interface energy [12]. Interface energy arises due to the termination of bonds at the surface, leaving undercoordinated atoms in a high energy state. Each broken bond can be thought of as contributing positive free energy to the system, such that planes with more dangling bonds have higher surface energy than planes with fewer dangling bonds. In a face centered cubic structure of an elemental metal such as Cu, the closest packed plane 1 1 1 contains the fewest dangling bonds per unit area, with just 3 of the 12 Cu-Cu bonds broken by the (1 1 1) plane. The surface area based on broken bonds

then increases from (1 1 1) to (1 0 0) to (1 1 0).

In general, the surface energy of a plane increases as the angle between the plane and the closest packed plane increases due to the number of broken bonds. If each broken bond contributes a positive energy $\epsilon/2$ to the free energy, then the energy is given by

$$E = (\cos(\theta) + \sin(|\theta|))\epsilon/(2a) \tag{4.2}$$

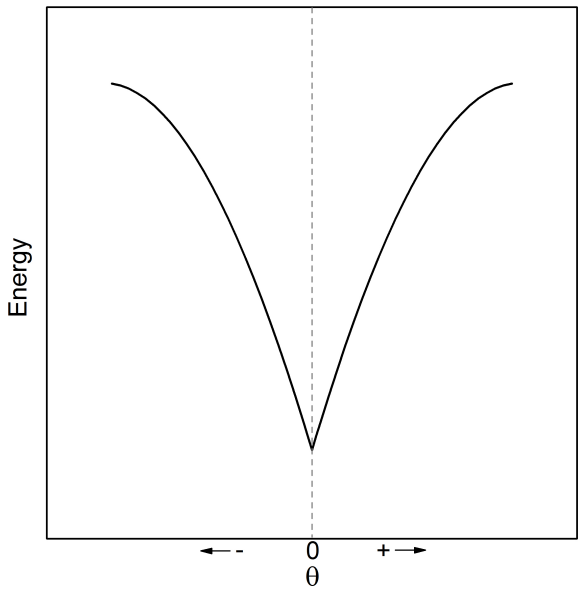

Figure 4.1: Surface energy based on Equation 4.2

where a is the unit length for the closest packed plane. The energy is at a minimum at $\theta = 0$ and increases with angle, as shown in Figure 4.1. Each low-index plane is also located at a minimum in E(θ), since they are also reasonably close packed and contain fewer broken bonds per unit area than high-index planes [12]. The interface energy term γ has a similar form, though the minimum at $\theta = 0$

is less pronounced as a result of entropic effects, as discussed later.

The total surface energy of a crystal is the sum of surface energy of each plane that defines the crystal shape, which is the product of each plane's area A and interface energy γ: $\sum_n \gamma_n A_n$. At equilibrium this sum is at a minimum in free energy. Figure 4.2 shows a 2D γ plot looking at the (1 0 0) plane of a cubic crystal, where the γ is shown in blue. A vector drawn from the origin of the plot to a point, P, on the surface represents the interface energy (γ_P) of that specific crystallographic plane perpendicular to the direction of γ_P. A plane drawn perpendicular to the γ vector is the corresponding Wulff plane. The innermost area defined by the Wulff planes forms the Wulff construction, which will naturally be the area enclosed by planes formed at the minima in the γ plot. The Wulff construction relates the equilibrium crystal shape to the relative surface energies of the constituent planes [12, 13].

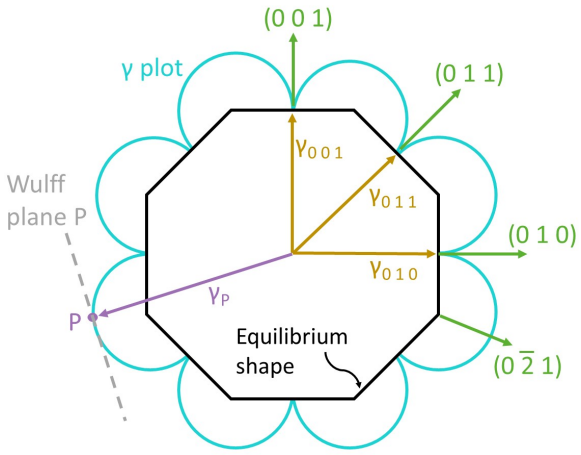

Figure 4.2: A possible gamma plot in the plane of (1 0 0) of a cubic crystal where the surface energy for (0 0 1) and (1 1 0) are the same.

This approach makes a few assumptions that do not always hold for real

systems. In particular, it assumes that all bonds are equal in energy and that entropy and volume are constant. Changes in volume affect the free energy, though below the melting point changes in volume for many solids are small relative to other effects. The entropy of surface atoms is higher than for atoms in the bulk, since they have more freedom of movement allowed by the reduction in number of bonds, and the entropy of the surface can be increased further by the formation of defects. This partially offsets the unfavorable energy gain associated with the formation of a surface, especially at higher temperatures. Additionally, surfaces will undergo reconstruction to minimize energy through the formation of new bonds between surface atoms, as well as adsorb species from the nucleation medium[14].

It is often very difficult or impossible to predict the method of surface reconstruction and adsorption, limiting the usefulness of a simple model for determination absolute or relative surface energy. However, well-formed crystals may have easily distinguishable faces, which necessarily represent a minimum in the free energy, at least under the conditions of the growth. This can be used to back out information about the energy of crystallographic planes and gain an understanding of relative bond energies in a system using the form of a crystal.

4.2 Chemical vapor transport method

Cu_2OSeO_3 crystals have been grown previously by the chemical vapor transport (CVT) method using a variety of transport agents and temperature gradients. The addition of a seed crystal in conjunction with CVT was shown in the present work

to increase the size and quality of the crystals. Seeded CVT is a technique that has rarely been used in the literature and had not previously been discussed in depth.

CVT relies on the vaporization of reactant material in a hot zone of the reaction vessel and migration of vapor phase species across a temperature gradient followed by controlled deposition into a colder zone of the vessel. There are many parameters, both controllable and uncontrollable, that affect the outcome of a CVT growth. Because of the complexity of CVT growth, the growth conditions require careful tuning and attention to detail.

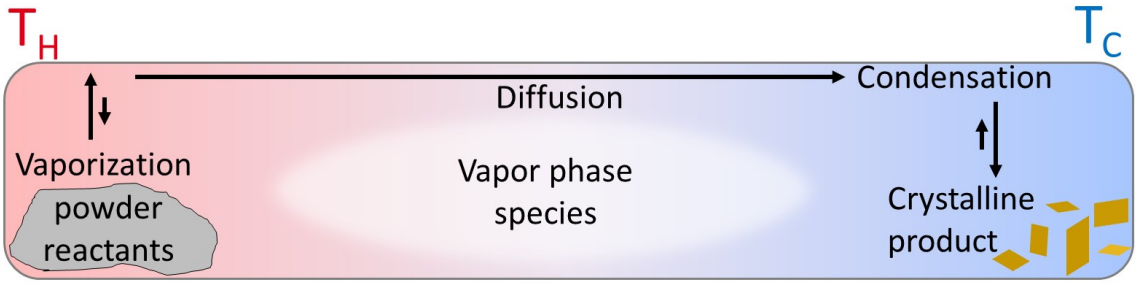

Figure 4.3: update with hot zone and cold zone labels

A typical CVT growth is done in a two- or three-zone tube furnace with each zone controlled independently. The growth vessel is set up as shown in Figure 4.3, and is long enough to cross at least two furnace zones to provide a distinct temperature gradient ($\Delta T = T_H - T_C$) which enables separation of the reactant and product species[15, 16]. For materials that self-transport, the only controllable factors that need to be tuned are the hot zone and cold zone temperatures, and through them the gradient. The hot zone temperature must be high enough to vaporize the starting materials, which may be either reactant components of the product or pre-formed powder of the pure product.

The cold zone temperature should be low enough to condense the vapor phase species, but not so low that the vapor species condense rapidly. Rapid condensation can result in nucleation of many small particles scattered around the cold zone of the vessel, rather than encouraging nucleation at one site and further condensation on the developed nucleus. In this case, the species may also condense as small, randomly oriented grains, rather than ordered crystal planes due to the kinetic limitation of diffusion of atoms across the particle surface. Rapid condensation may also prevent stoichiometric reaction between the vapor species to form the desired product.

In addition to the constraints on T_H and T_C imposed by the physical properties of the reactants, products, and vapor phase, T_H and T_C must also be chosen to provide an ideal temperature gradient. A large gradient will result in more convection within the tube, which may have an effect similar to stirring a solution. The increased gas flow within the tube can assist in re-evaporating small nucleated particles in the cold zone, encouraging growth of one single crystal over many small crystals[15, 16].

Transport agents (TA) are necessary when the starting material does not have a high enough vapor pressure (on the order of $P > 10$ mTorr in typical evacuated silica ampoule) to have a significant amount of material in the vapor phase for reasonable hot zone temperatures. TAs must have high vapor pressure or form high vapor pressure species upon reaction with the growth starting materials. The TA also must be able to interact with the starting materials to get them into the vapor phase, comparable to dissolving reactants in a solvent. This usually means

forming a volatile, metastable complex which will readily decompose into or react to form the desired product upon condensation.

The results of CVT growths can be improved dramatically with the addition of a seed crystal. The seed crystal has to be large enough to retain its outer form as the reaction vessel reaches temperature and the transport agent begins to act upon the materials inside. Vapor phase species tend to condense preferentially onto the seed, which naturally presents more favorable interactions than the only other available surface, which is the wall of the reaction vessel. The effects of including a seed on both the mechanism of CVT crystal growth and the results of the growth in the Cu_2OSeO_3 system are discussed in the section to follow.

4.3 Seeded Chemical Vapor Transport Growth of Cu_2OSeO_3

The following section reports the crystal growth and analysis of Cu_2OSeO_3 crystals. This work was co-written by the following authors and published under the following citation:

Crystal Growth & Design, **2017**, 17 (9), pp 4944-4948

DOI: 10.1021/acs.cgd.7b00879

Jessica R. Panella[1], Benjamin A. Trump[1], Guy G. Marcus[2] Tyrel M. McQueen[1,2,3,*]

[1]Department of Chemistry, The Johns Hopkins University, Baltimore, MD 21218, USA

[2]Institute for Quantum Matter, Department of Physics, The Johns Hopkins University, Baltimore, MD 21218, USA

[3]Department of Materials Science and Engineering, The Johns Hopkins University, Baltimore, MD 21218, USA

*Corresponding author

4.3.1 Abstract

We present an optimized seeded chemical vapor transport method for the growth of Cu_2OSeO_3 that allows for chemical control in a system with many stable phases to selectively produce large phase-pure single crystals. This method is shown to consistently produce single crystals in the range of 120 to 180 mg. A Wulff construction model of a representative crystal shows that the minimum energy surface is {1 1 0}, followed by {1 0 0}. Analysis of the lowest index planes revealed that cleavage of Se-O bonds has a large energy cost, leading to an overall high surface energy. The seeded chemical vapor transport demonstrated here shows promise for large single crystal growth of other functional materials such as Weyl semimetals, frustrated magnets, and superconductors.

4.3.2 Introduction

Investigation of magnetic materials is frequently limited by an inability to obtain sufficiently large, phase-pure single crystals. This is especially true for materials containing anisotropic magnetism, geometric magnetic frustration, or ferrimagnetism. A unique example of this is Cu_2OSeO_3, which has been studied heavily in recent years [1–6]. Already a rare example of an insulating, noncentrosymmetric ferrimagnet [2], the production of single crystals was essential for the discovery of a magnetic skyrmion lattice [3, 17], in which a collection of localized spins form a regular pattern of vortex-like structures.

The cubic Cu_2OSeO_3 crystallizes in a distorted pyrochlore structure with Cu_4O

and SeO_3 units. Three Cu^{2+} in each tetrahedron are ferromagnetically aligned and the remaining Cu^{2+} is anti-parallel to the others, forming a net spin-1 entity [2, 18]. This ordering is the result of both symmetric and antisymmetric magnetic exchange interactions. While the ground state magnetic ordering is ferrimagnetic, there is a region of parameter space for which helical spin textures emerge due to the spin-orbit coupling derived antisymmetric exchange, or Dzyaloshinskii-Moriya, interaction leading to a magnetic skyrmion lattice [19, 20]. Cu_2OSeO_3 is the only known insulating skyrmion material, which makes it a promising candidate for the realization of voltage-driven skyrmion-based devices and for use as a substrate material in thin film work.

Cu_2OSeO_3 crystals sufficient for these experiments have previously been grown by chemical vapor transport (CVT), which uses a vapor phase transport agent to facilitate gas phase diffusion of one or more of the species involved in the growth across a controlled temperature gradient [1, 2, 21, 22]. Typical transport agents include H_2, HCl, Cl_2, I_2, and $TeCl_4$, which react with one or more of the species involved with the growth to produce high vapor pressure species with high mobility [23, 24]. Nucleation in CVT typically occurs along the wall of the reaction vessel, and can result in many small crystals if many nucleation sites are present. Adding a seed crystal to the cool end of the gradient promotes nucleation on the seed, encouraging the growth of one large crystal. There are few examples of seeded CVT in the literature, with the main ones being the growth of transparent ZnO and IR-sensitive $Hg_{0.8}Cd_{0.2}Te$ [25, 26].

Recent reports have used source temperatures of 610 °C and 607 °C and deposition temperatures of 500 °C and 527 °C, using HCl gas as the transport agent [1, 22, 27]. The seeded CVT method reported herein improves the phase selectivity over previously reported methods via carefully chosen source and deposition temperatures, and the addition of a seed crystal dramatically increases the average size of the grown crystals. The result is the ability to consistently produce large (~150 mg), high purity, extremely well-faceted crystals. The size and quality of crystals grown by seeded CVT makes them well-suited for use as substrates due to the well-defined facets, and aids in the ability to align them for measurements such as terahertz spectroscopy, inelastic neutron scattering, and thermal transport [6, 28]. This work also expands on the little-explored area of seeded chemical vapor transport crystal growth, demonstrating the usefulness of this technique.

4.3.3 Methods

4.3.3.1 Materials

CuO (Alfa Aesar, 99.995%) and NH_4Cl (Sigma-Aldrich, ACS Grade) were used as received. SeO_2 (Alfa Aesar, 99.99%) was purified by sublimation under flowing oxygen at 325 °C per Ref. [29] to avoid off-stoichiometry and dangerously high pressures. The oxygen flow was directed through a drying tube filled with Drierite then bubbled through concentrated nitric acid (BDH, ACS Grade) before passing over the as-received, pink SeO_2. The resulting snow-white SeO_2 needle-like crystals were transferred to an argon-filled glovebox. Care should be taken when handling SeO_2 due to its extreme toxicity.

4.3.3.2 Synthesis of Cu_2OSeO_3 Powder

Polycrystalline Cu_2OSeO_3 was synthesized by direct solid state reaction of the oxides, in a 2:1 molar ratio of CuO to SeO_2, following Bos *et al.* [2]. The oxide precursors were ground thoroughly in an argon-filled glovebox and 5-20 g were sealed in an evacuated fused silica ampoule. The reaction mixture was ramped to 600 °C at a rate of 100 °C/hr, held at temperature for 12 hrs, then the reaction tube was quenched in water. The resulting product was ground in air and reheated until the product was a uniform, olive green color upon grinding, usually three times.

4.3.3.3 Seed Crystal Growth

Single crystals were grown by the chemical vapor transport method using NH_4Cl as the transport agent [1, 5]. A one gram charge of Cu_2OSeO_3 powder was sealed in an evacuated fused silica ampoule along with 0.4 mg/cm^3 NH_4Cl, which was added in an argon-filled glovebox. The tube was positioned between the first two zones of a three-zone tube furnace. The source and deposition zones were ramped at 100 °C/hr to 640 °C and 530 °C, respectively. The temperature accuracy of each zone was verified using an external, NIST calibration-traceable thermocouple. This temperature gradient was maintained for 6 weeks. The source zone was cooled to room temperature approximately 7 hrs before the deposition zone to allow inversion of the temperature gradient and force vapor phases to condense opposite the crystals. Crystals were rinsed with Type I, deionized H_2O and ethanol once the growth finished to remove any remaining NH_4Cl.

4.3.3.4 Seeded CVT Growth

A crystal from an unseeded growth, weighing 10 mg $\leq m \leq$ 20 mg, was chosen for use as a seed crystal for a seeded growth. Any obvious twinned or conjoined portion was cleaved off prior to use as a seed. Cu_2OSeO_3 powder and NH_4Cl were added to one end of a fused silica tube as before, taking care to keep the powder off of the tube walls. The tube was necked in the middle, the seed crystal was added, and the tube was sealed under vacuum. The same heating cycle was used for the seeded growth. The tube set up and temperature gradient are shown in Fig. 4.4(a). The results of roughly 36 unseeded and 38 seeded growths are reported here.

4.3.3.5 Characterization

Back-reflection X-ray Laue diffraction was used to identify crystal faces and crystalline quality. Laue images were taken using a Multiwire Laboratories MWL 110 real-time back reflection Laue camera with a tungsten source operating sub-K_α at 10 kV and 10 mA. Powder X-ray diffraction (XRD) of ground single crystals was used to confirm phase purity using a Bruker D8 Focus operating with a Cu K_α ($K_{\alpha 1}$ = 1.5406 Å) radiation with a LynxEye position sensitive detector. Additionally, magnetization was used to confirm phase purity and reproducibility of physical properties. Magnetization data was collected on a Quantum Design Physical Properties Measurement System using the ACMS dc option. Temperature-dependent magnetization was measured with an applied field of μ_0H = 18 Oe, and field-dependent magnetization was measured at T = 2 K and T = 60 K over the field range μ_0H = 0 to 70000 Oe.

Structure images were generated using VESTA [30], and Wulff constructions were generated using WinXMorph [31]. QLaue was used to simulate the Laue diffraction pattern [32].

4.3.4 Results and Discussion

A schematic diagram of the seeded CVT set up is shown in Fig. 4.4(a), with the charge and transport agent shown on the source end and a single seed crystal on the deposition end. The large, glossy, dark green crystals grown by seeded CVT, are shown in Fig. 4.4(c) with the inset showing a small crystal set on a reflective sheet to highlight the color of the material. Each growth produces roughly 100-150 mg of crystals (10-15% yield), irrespective of the mass of the charge, either as one large (~4x4x4mm) crystal or several smaller crystals. Using seed crystals larger than ~20 mg did not additionally benefit the growth, while significantly smaller seeds could not initiate nucleation, likely because they were consumed by the transport agent during furnace warming. The masses of crystals grown by a similar number of unseeded and seeded growths are summarized in the histogram in Fig. 4.5. The histogram clearly shows a bimodal distribution in crystal sizes, with seeded growths (green) consistently yielding much larger crystals. Unseeded growths (grey) produced many more crystals, as the overall yield by mass is the same despite much smaller sizes. Crystals weighing less than 10 mg were excluded for clarity.

The CuO-SeO_2 system has several species that form under very similar thermodynamic conditions and differ in the ratio of CuO:SeO_2, namely $CuSeO_3$ (1:1),

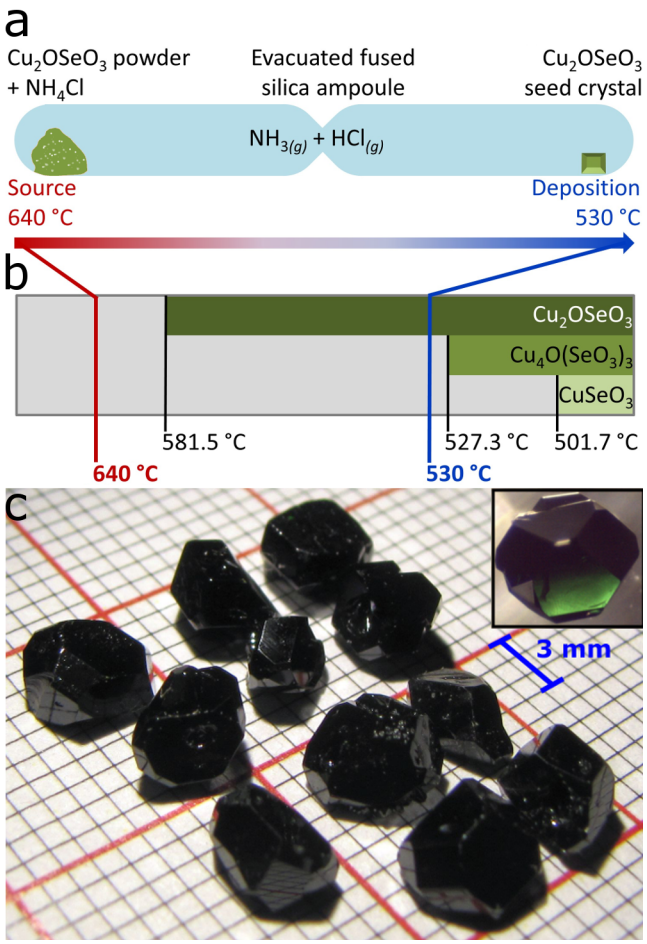

Figure 4.4: Seeded CVT Diagram and Resultant Crystals. (a) A diagram of the seeded CVT growth set-up. (b) A graphic detailing the temperatures below which the three primary CuO-SeO_2 phases are stable and their relation to the growth temperatures. (c) A collection of large Cu_2OSeO_3 crystals grown by the seeded CVT method, displaying smooth, mirror-like facets. The inset shows a small crystal set on a reflective sheet to highlight the color of the material.

$Cu_4O(SeO_3)_3$ (4/3:1), and Cu_2OSeO_3 (2:1) [8, 9]. That they differ primarily in the ratio of two species makes phase selection based on stoichiometry difficult, as direct control of the ratio of the vapor phase species is nearly impossible. Careful tuning of the reaction temperature provides conditions more favorable for the

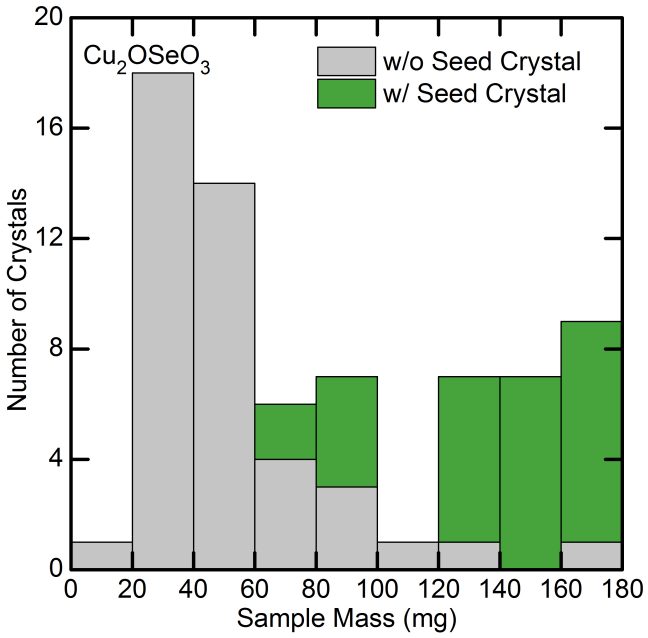

Figure 4.5: Histogram of Crystal Sizes. A histogram showing the number of crystals having a given mass for about 36 unseeded and 38 seeded growths, with the bimodal distribution demonstrating the advantage of the seeded growth (green) over unseeded growth (gray) for obtaining large single crystals.

formation of Cu_2OSeO_3 over related species, as detailed below.

The transport agent, $NH_4Cl_{(s)}$, sublimes at around T = 340 °C, yielding $NH_{3(g)}$ and $HCl_{(g)}$. At T > 581.5 °C, well below the source temperature (640 °C), Cu_2OSeO_3 decomposes into $CuO_{(s)}$ and $SeO_{2(g)}$ [10, 11]. Given the high vapor pressure of SeO_2 at elevated temperatures, we propose that SeO_2 self-transports, while $CuO_{(s)}$ reacts with $HCl_{(g)}$ to form volatile Cu-containing species that transport[29]. Nucleation at the deposition end continually removes vapor phase species, a process which is in dynamic equilibrium with the vaporization at the source end. Our results are explained if the high source zone temperature increases the rate of reaction between $CuO_{(s)}$ and $HCl_{(g)}$ to achieve a higher ratio of CuO:SeO_2, closer to the

ideal 2:1 ratio, which helps prevent formation of $CuSeO_3$. The deposition zone temperature, 530 °C, was chosen to be just higher than the decomposition temperature of the most commonly observed contaminant, $Cu_4O(SeO_3)_3$, which decomposes at $T \geq 527.3$ °C [11]. This helps prevent concurrent growth of $Cu_4O(SeO_3)_3$ and produces high purity unseeded and seeded crystals alike. This is in contrast to previous growths of Cu_2OSeO_3, which used deposition temperatures below the decomposition of $Cu_4O(SeO_3)_3$ and significantly lower source temperatures for an overall smaller temperature gradient [1, 22, 27]. Fig. 4.4(b) summarizes the stability of $CuSeO_3$, $Cu_4O(SeO_3)_3$, and Cu_2OSeO_3 with respect to temperature, highlighting the importance of the deposition zone temperature for phase selectivity.

Furthermore, the use of a seed crystal helps prevent unwanted excess nucleation along the tube wall by locally depleting the concentration of gas-phase species as they deposit on the seed crystal. The seed crystal also presents a more favorable substrate for deposition than silica. The large temperature gradient (110 °C) creates turbulence within the tube, effectively limiting the ability of small, undesired nuclei from growing to a stable size. Additionally, since the seed already has the appropriate 2:1 ratio of $CuO:SeO_2$, further growth will maintain the stoichiometry, producing one large Cu_2OSeO_3 crystal.

The crystallinity of seeded CVT grown samples is demonstrated via the Laue XRD pattern shown in Fig. 4.6, oriented in the [1 1 0] direction. Diffraction spots close to the center are exceptionally sharp, exemplifying the excellent crystallinity of these crystals. Streaking seen in spots farther from the center is due to experimental broadening caused by the broad spectrum x-ray source of the MWL

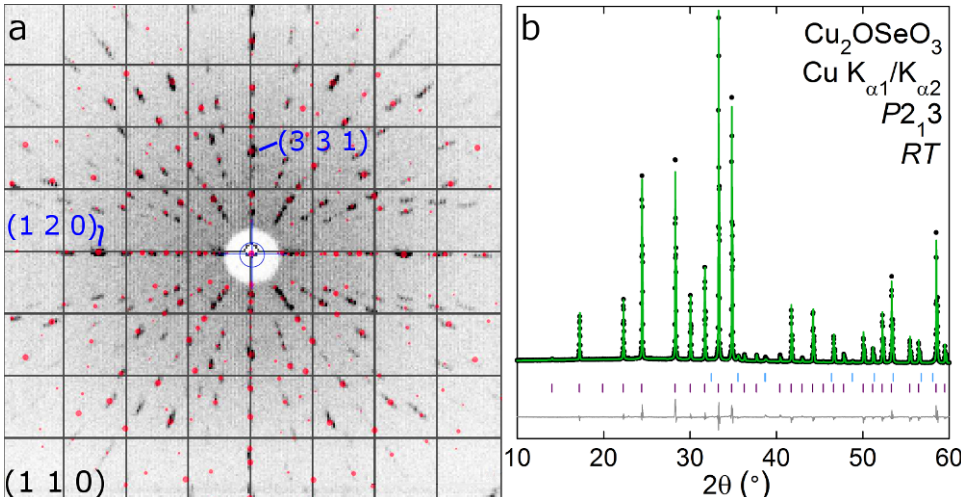

Figure 4.6: Single Crystal Laue XRD Pattern. (a) An experimental diffraction image taken looking at the (1 1 0) plane with a calculated pattern overlaid. (b) A powder XRD pattern demonstrating phase purity. The data is shown in black, the calculated fit in green, and the difference in gray. The dark violet tick marks correspond to allowed Cu_2OSeO_3 peak positions, and the light blue ticks to CuO.

110. The experimental pattern shows no measurable mosaicity or twinning. The calculated pattern, shown in Fig. 4.6(b), closely matches the experimental data. Though the seeded CVT grown crystals were too large for bulk analysis using single crystal XRD, several were independently ground for powder XRD to verify that they contained no core impurities. No other ternary Cu-Se-O phases were present within the detection limit of the diffractometer, as shown in Fig. 4.6(b). Rietveld refinement of a calculated fit (green) to the experimental data (black) using only Cu_2OSeO_3 and CuO captures all of the visible peaks with an goodness of fit of 3.442. The small amount of CuO present in the powder XRD pattern is likely unreacted powder from the surface of the crystal from condensation of residual gas phase Cu species. Additionally, magnetization data (not shown) as a function

of temperature and field, both above and below T_N, was used to confirm purity, consistently yielding data identical to those in Refs. [2, 3, 17].

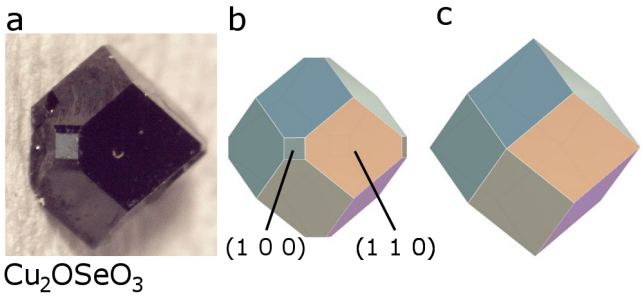

Figure 4.7: Crystal and Matching Wulff Construction (a) A representative crystal very near its equilibrium structure. (b) A Wulff construction matching the structure of the crystal. (c) Proposed crystal morphology in the absence of the influence of the tube wall.

In the case of Cu_2OSeO_3, the crystal morphology seems to be impacted by the crystals' adherence to the wall of reaction tube. Growth from the tube wall could result in additional strain on the crystal during growth, changing the energy balance between the crystal planes enough to affect the global morphology of the crystal, as strong interactions with growth environment is known to affect morphology [33, 34]. Alternatively, interactions with the tube wall may change the growth kinetics, resulting in different crystal shapes depending on which plane adheres to the tube wall and how close the crystal is to reaching equilibrium.

As an example of this effect, a well-formed seed crystal is shown in Fig. 4.7(a) alongside a corresponding Wulff construction in Fig. 4.7(b) that is defined by (1 1 0)- and (1 0 0)-type planes, and a similar construction that is defined by only (1 1 0)-type planes in Fig. 4.7(c). The crystal is almost an ideal rhombic dodecahedron, defined by primarily (1 1 0)-type faces, with one square (1 0 0)-type face truncating a single vertex. The vertex that is occupied by the (1 0 0)-type face sits very close to

the edge that adhered to the tube wall, while the other vertices that are situated farther away from the tube reach sharp points. Assuming that the crystal is in its equilibrium shape, then the lowest surface energy plane for the bulk, free-standing crystal, in the absence of the tube wall, is the (1 1 0), and all other planes are significantly higher in energy, which would render a form as shown in Fig. 4.7(c). However, for the portion of the crystal that is strongly interacting with the fused silica tube, the surface energy of (1 0 0)-type planes is much closer to the surface energy of (1 1 0)-type planes, resulting in the growth of a (1 0 0)-defined facet. If the effect of the tube wall is kinetic rather than thermodynamic, then Fig. 4.7(c) is the equilibrium shape and further growth would result in the disappearance of the (1 0 0) face.

4.3.5 Analysis of Crystals via Wulff Construction

Information regarding relative surface energy of crystals with easily identifiable facets, as seen in seeded-CVT-grown Cu_2OSeO_3 crystals, can be extracted using the principle of surface energy minimization via a Wulff construction. Since the surface energy of a crystallographic plane is assumed to be the product of its interface energy term γ and its area A, as discussed in Section 4.1,and the surface is at an energetic minimum, then the ratio of the interface energy terms for the visible planes can be determined from the ratio of their surface area. A Wulff construction can be used to visualize the crystal form in relation to γ by generating a generic Wulff construction based on the point symmetry of the crystal system, and adjusting the parameters to match the form of a grown crystal.

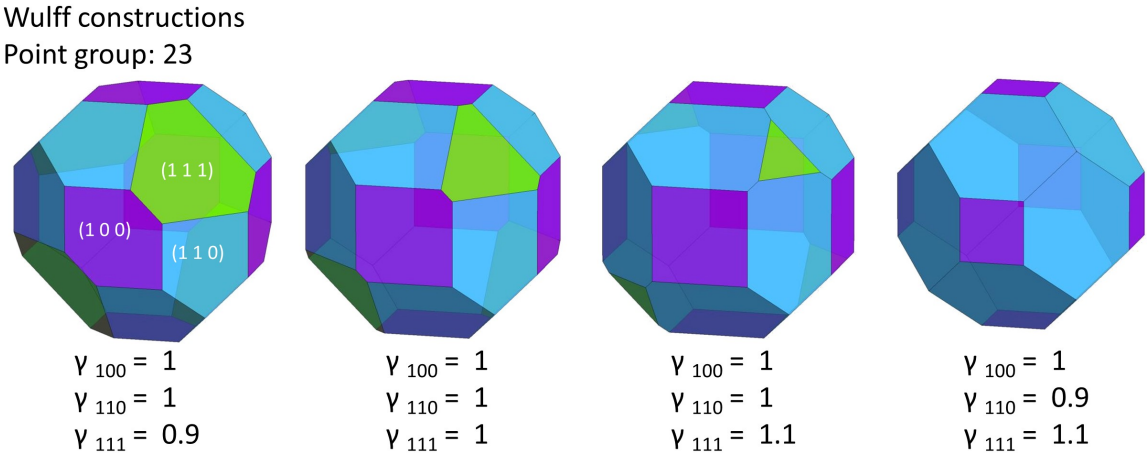

Figure 4.8: Four Wulff constructions with $\bar{4}$3m with different ratios of γ for the three included planes.

Figure 4.8 shows four Wulff constructions in the $\bar{4}$3m point group with different ratios of γ [35]. As γ for a plane increases, the surface area of that plane gets smaller. If γ for one plane is too large relative to one of the other planes, it can no longer form a minimum energy surface, and its surface area is reduced to zero. Using a Wulff construction matched to a crystal form, the ratio of γ for the visible planes yields relative surface energies. Chemical intuition can link the relative surface energies to the chemistry and bond energies present in the associated planes.

This method assumes that the crystal used for comparison had reached equilibrium before its growth was halted. If that is not the case, then the shape is affected by the growth kinetics of the planes, and minimum energy cannot be assumed. This is one of the limitations of extracting information about surface energies from crystal forms. Additionally, the form represents the minimum energy under growth conditions, which are often quite different from ambient conditions, at least in terms of temperature, and often in terms of environmental chemistry as

well.

Using the Wulff construction in Fig. 4.7(b), the ratio of surface energies in the strongly interacting region of the crystal is 1.26:1 (1 0 0):(1 1 0). This ratio qualitatively matches what is observed by visual inspection of the crystals, which are all affected by fused silica growth tube. Most of the crystals have large (1 1 0)-type faces and smaller (1 0 0)-type faces. Occasionally, other low-index planes, such as (1 1 1), will be displayed, which is probably determined by the orientation of the crystals during the nucleation process.

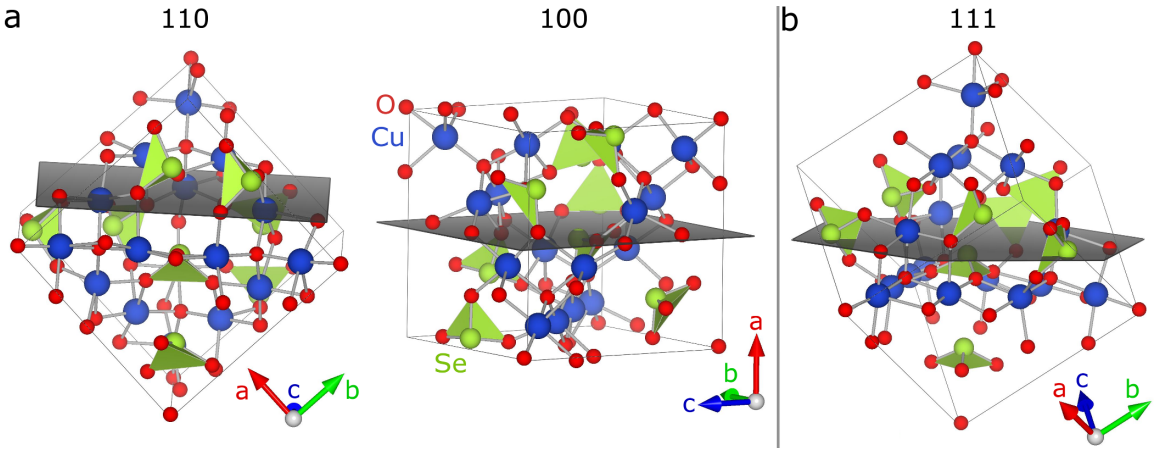

Figure 4.9: Structure with Low Index Planes. (a) Both the (1 1 0)- and (1 0 0)-type planes are shown at a position within the cell where all SeO_3 polyhedra are either fully above or fully below the plane. (b) The (1 1 1) is placed to minimize the number of SeO_3 bonds broken, but it still bisects multiple SeO_3 polyhedra.

In the absence of strong environmental effects, the lattice planes have characteristic surface energies that are affected by a number of system-dependent chemical and interface factors, such as lattice relaxation, bond termination, and surface reconstruction processes. While all systems experience some degree of relaxation or reconstruction at interfaces, an examination of the crystal structure of

Cu_2OSeO_3 yields insight into the relationship between bond energy and surface energy: namely that the two predicted lowest energy planes, the (1 1 0) and the (1 0 0), can cleave the lattice without breaking any Se-O bonds. The next lowest index plane, the (1 1 1), must either break Se-O bonds or cleave the densely-packed layers of Cu-O polyhedra.

While any dangling bond is reactive and high energy, the bond dissociation energy of an Se-O bond is 430(6) kJ/mol as compared to 287(11) kJ/mol for a Cu-O bond, implying that a surface containing a broken Se-O bond would be much higher in energy than a surface containing only broken Cu-O bonds [36]. Fig. 4.9 shows the structure of Cu_2OSeO_3 with each of the three lowest index planes placed to minimize the effect on the rigid SeO_3 units. Both the (1 1 0) and (1 0 0) planes shown in Fig. 4.9(a) are placed a narrow region in the structure that does not contain any SeO_3, demonstrated by the face that the green SeO_3 polyhedra are all fully above or fully below the black crystal planes. The (1 1 1) plane in Fig. 4.9(b) intersects multiple SeO_3 polyhedra, even when placed to minimize Se-O bond cleavage.

Based on observations of the shape of the many crystals produced by both seeded and unseeded CVT, the (1 1 0) and (1 0 0) are both low energy surfaces, indicating that bond cleavage is likely a strong factor in determining the surface energies in this system, with the Se-O bond cleavage being highly unfavorable. Given that neither the (1 1 0) or (1 0 0) planes necessarily break Se-O bonds, other factors, such as Cu-O bond cleavage and surface reconstruction, likely determine which has the least surface energy. An understanding of surface behavior in the

Cu_2OSeO_3 system is important to further studies in thin film and interface physics.

4.3.6 Conclusion

The seeded CVT method reported here optimizes crystal growth conditions for species selectivity and for producing large Cu_2OSeO_3 single crystals based on an understanding of both the vapor phase chemistry and equilibrium thermodynamics. Careful selection of source and deposition zone temperatures provides conditions that are unfavorable for competing Cu-Se-O species, while the use of a seed crystals inhibits excessive nucleation and reinforces the 2:1 $CuO:SeO_2$ ratio to encourage growth of large, single-phase Cu_2OSeO_3 crystals. Seeded CVT produces crystals that frequently weigh in excess of 100 mg and have exceptionally well-defined faces and clean edges. Crystals grown by seeded CVT are of sufficient quality for a plethora of measurements and techniques, from inelastic neutron scattering to use as substrate material for thin film work. Furthermore, the recognizable dodecahedral morphology of the crystals gives insight into the relative surface energies of the underlying crystal structure and extrinsic factors affecting those energies. The techniques and chemical insight reported herein are applicable to numerous electronically and magnetically interesting systems currently grown by traditional, unseeded CVT, such as Weyl semimetals WTe_2, $MoTe_2$, $ZrTe_5$, TaP, NbP, superconductor FeSe, and spin-liquid candidate $FeSc_2S_4$ [37–42].

4.3.7 Acknowledgments

This research was supported by the Research Corporation for Science Advancement (Cottrell Scholar Award) and NSF, Division of Materials Research, Solid State Chemistry, CAREER Grant under Award DMR-1253562. Partial funding for this work was provided by the Johns Hopkins University Catalyst Fund. GGM acknowledges generous support from the NSF-GRFP, Grant No. DGE-1232825.

For Table of Contents Use Only

Title: Seeded Chemical Vapor Transport Growth of Cu_2OSeO_3

Authors: Jessica R. Panella, Benjamin A. Trump, Guy G. Marcus, and Tyrel M. McQueen

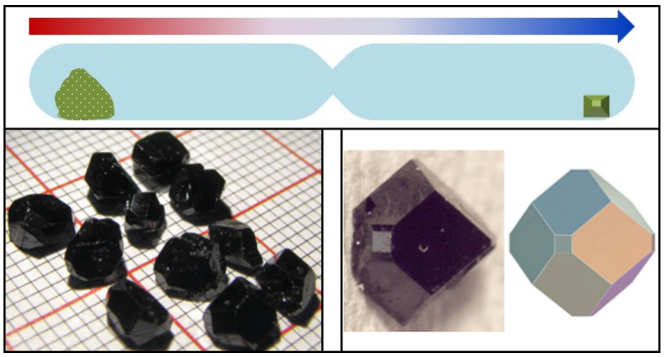

We present an optimized seeded chemical vapor transport growth of large (>100 mg) single crystals of phase pure Cu_2OSeO_3. Relative surface energies of crystallographic planes are analyzed using a Wulff construction, revealing the {1 1 0} and {1 0 0} to be the lowest energy surfaces. Factors affecting phase purity and crystal morphology are discussed in the context of gas phase chemistry and thermodynamics.

References

[1] M. Belesi, I. Rousochatzakis, H. C. Wu, H. Berger, I. V. Shvets, F. Mila, and J. P Ansermet. "Ferrimagnetism of the magnetoelectric compound Cu_2OSeO_3 probed by ^{77}Se NMR". In: *Phys. Rev. B* 82.9 (2010), p. 094422. DOI: 10.1103/PhysRevB.82.094422.

[2] Jan-Willem G. Bos, Claire V. Colin, and Thomas T. M. Palstra. "Magnetoelectric coupling in the cubic ferrimagnet Cu_2OSeO_3". In: *Phys. Rev. B* 78.9 (2008), p. 094416. DOI: 10.1103/PhysRevB.78.094416.

[3] S. Seki, X. Z. Yu, S. Ishiwata, and Y. Tokura. "Observation of Skyrmions in a Multiferroic Material". en. In: *Science* 336.6078 (2012), pp. 198–201. ISSN: 0036-8075, 1095-9203. DOI: 10.1126/science.1214143.

[4] Oleg Janson, Ioannis Rousochatzakis, Alexander A. Tsirlin, Marilena Belesi, Andrei A. Leonov, Ulrich K. Rößler, Jeroen van den Brink, and Helge Rosner. "The quantum nature of skyrmions and half-skyrmions in Cu_2OSeO_3". en. In: *Nat. Commun.* 5 (2014), p. 5376. ISSN: 2041-1723. DOI: 10.1038/ncomms6376.

[5] P. Y. Portnichenko, J. Romhányi, Y. A. Onykiienko, A. Henschel, M. Schmidt, A. S. Cameron, M. A. Surmach, J. A. Lim, J. T. Park, A. Schneidewind, D. L. Abernathy, H. Rosner, Jeroen van den Brink, and D. S. Inosov. "Magnon spectrum of the helimagnetic insulator Cu_2OSeO_3". en. In: *Nat. Commun.* 7 (2016), p. 10725. ISSN: 2041-1723. DOI: 10.1038/ncomms10725.

[6] N. J. Laurita, G. G. Marcus, B. A. Trump, J. Kindervater, M. B. Stone, T. M. McQueen, C. L. Broholm, and N. P. Armitage. "Low-energy magnon dynamics and magneto-optics of the skyrmionic Mott insulator Cu_2OSeO_3". In: *Phys. Rev. B* 95.23 (2017), p. 235155. DOI: 10.1103/PhysRevB.95.235155.

[7] Jessica R. Panella, Benjamin A. Trump, Guy G. Marcus, and Tyrel M. McQueen. "Seeded Chemical Vapor Transport Growth of Cu_2OSeO_3". In: *Crystal Growth & Design* 17.9 (2017), pp. 4944–4948. ISSN: 1528-7483. DOI: 10.1021/acs.cgd.7b00879.

[8] Herta Effenberger and Franz Pertlik. "Die Kristallstrukturen der Kupfer(II)-oxo-selenite $Cu_2O(SeO_3)$ (kubisch und monoklin) und $Cu_4O(SeO_3)_3$ (monoklin und triklin)". de. In: *Monatsh. Chem.* 117.8-9 (1986), pp. 887–896. ISSN: 0026-9247, 1434-4475. DOI: 10.1007/BF00811258.

[9] Georges Meunier and Michel Bertaud. "Constantes cristallographiques de $CuSe_2O_5$, $CuSeO_3$ et Cu_2SeO_4". In: *J. Appl. Crystallogr.* 9 (1976), pp. 364–366.

[10] B. Papánková and H. Langfelderová. "The relationship between the structures of Cu(II) complexes and their chemical transformations". en. In: *J. of Therm. Anal.* 35.7 (1989), pp. 2347–2358. ISSN: 0022-5215, 1572-8943. DOI: 10.1007/BF01911899.

[11] E. L. Fokina, E. V. Klimova, M. V. Charykova, V. G. Krivovichev, N. V. Platonova, V. V. Semenova, and W. Depmeier. "The thermodynamics of arsenates, selenites, and sulfates in the oxidation zone of sulfide ores: VIII. Field of thermal stability of synthetic analog of chalcomenite, its dehydration and dissociation". en. In: *Geol. Ore Deposits* 56.7 (2014), pp. 538–545. ISSN: 1075-7015, 1555-6476. DOI: 10.1134/S1075701514070058.

[12] David A. Porter, Kenneth E. Easterling, and Mohamed Sherif. *Phase Transformations in Metals and Alloys, Third Edition*. English. 3 edition. Boca Raton, FL: CRC Press, 2009. ISBN: 978-1-4200-6210-6.

[13] G. Wulff. "Zur Frage der Geschwindigkeit des Wachsthums und der Auflösung der Krystallflächen". In: *Z. Kristallogr. Cryst. Mater.* 34.1-6 (1901), pp. 449–530. ISSN: 2196-7105. DOI: 10.1524/zkri.1901.34.1.449.

[14] K. Oura, M. Katayama, A. V. Zotov, V. G. Lifshits, and A. A. Saranin. "Atomic Structure of Clean Surfaces". en. In: *Surface Science*. Advanced Texts in Physics. Springer, Berlin, Heidelberg, 2003, pp. 171–194. ISBN: 978-3-642-05606-2 978-3-662-05179-5. DOI: 10.1007/978-3-662-05179-5_8.

[15] Binnewies Michael, Glaum Robert, Schmidt Marcus, and Schmidt Peer. "Chemical Vapor Transport Reactions – A Historical Review". In: *Zeitschrift für anorganische und allgemeine Chemie* 639.2 (2013), pp. 219–229. ISSN: 0044-2313. DOI: 10.1002/zaac.201300048.

[16] Peer Schmidt, Michael Binnewies, Robert Glaum, and Marcus Schmidt. "Chemical Vapor Transport Reactions–Methods, Materials, Modeling". en. In: *Advanced Topics on Crystal Growth* (2013). DOI: 10.5772/55547.

[17] T. Adams, A. Chacon, M. Wagner, A. Bauer, G. Brandl, B. Pedersen, H. Berger, P. Lemmens, and C. Pfleiderer. "Long-Wavelength Helimagnetic Order and Skyrmion Lattice Phase in Cu_2OSeO_3". In: *Phys. Rev. Lett.* 108.23 (2012), p. 237204. DOI: 10.1103/PhysRevLett.108.237204.

[18] Judit Romhányi, Jeroen van den Brink, and Ioannis Rousochatzakis. "Entangled tetrahedron ground state and excitations of the magnetoelectric skyrmion material Cu_2OSeO_3". In: *Phys. Rev. B* 90.14 (2014), p. 140404. DOI: 10.1103/PhysRevB.90.140404.

[19] T.H.R. Skyrme. "A unified field theory of mesons and baryons". en. In: *Nucl. Phys.* 31 (1962), pp. 556–569. ISSN: 00295582. DOI: 10.1016/0029-5582(62)90775-7.

[20] S. Mühlbauer, B. Binz, F. Jonietz, C. Pfleiderer, A. Rosch, A. Neubauer, R. Georgii, and P. Böni. "Skyrmion Lattice in a Chiral Magnet". en. In: *Science* 323.5916 (2009), pp. 915–919. ISSN: 0036-8075, 1095-9203. DOI: 10.1126/science.1166767.

[21] J. S. White, I. Levatić, A. A. Omrani, N. Egetenmeyer, K. Prša, I. Živković, J. L. Gavilano, J. Kohlbrecher, M. Bartkowiak, H. Berger, and H. M. Rønnow. "Electric field control of the skyrmion lattice in Cu 2 OSeO 3". en. In: *J. Phys.: Condens. Matter* 24.43 (2012), p. 432201. ISSN: 0953-8984. DOI: 10.1088/0953-8984/24/43/432201.

[22] K. H. Miller, X. S. Xu., H. Berger, E. S. Knowles, D. J. Arenas, M. W. Meisel, and D. B. Tanner. "Magnetodielectric coupling of infrared phonons in single-crystal Cu_2OSeO_3". In: *Phys. Rev. B* 82.14 (2010), p. 144107. DOI: 10.1103/PhysRevB.82.144107.

[23] J. Mercier. "Recent developments in chemical vapor transport in closed tubes". In: *J. Cryst. Growth* 56.2 (1982), pp. 235–244. ISSN: 0022-0248. DOI: 10.1016/0022-0248(82)90439-0.

[24] Michael Binnewies, Robert Glaum, Marcus Schmidt, and Peer Schmidt. "Chemical Vapor Transport Reactions — A Historical Review". en. In: *Z. Anorg. Allg. Chem.* 639.2 (2013), pp. 219–229. ISSN: 1521-3749. DOI: 10.1002/zaac.201300048.

[25] Paweł Skupiński, Krzysztof Grasza, Andrzej Mycielski, Wojciech Paszkowicz, Elżbieta Łusakowska, Emil Tymicki, Rafał Jakieła, and Bartłomiej Witkowski. "Seeded growth of bulk ZnO by chemical vapor transport". en. In: *Phys. Status Solidi A* 247.6 (2010), pp. 1457–1459. ISSN: 03701972, 15213951. DOI: 10.1002/pssb.200983232.

[26] Heribert Wiedemeier and Guangheng Wu. "Bulk growth of $Hg_{0.8}Cd_{0.2}Te$ single crystals by a combined CVT-seeding technique". en. In: *J. Electron. Mater.* 20.11 (1991), pp. 891–898. ISSN: 0361-5235, 1543-186X. DOI: 10.1007/BF02816028.

[27] V. Dyadkin. "Chirality of structure and magnetism in the magnetoelectric compound Cu_2OSeO_3". In: *Phys. Rev. B* 89.14 (2014). DOI: 10.1103/PhysRevB.89.140409.

[28] N. Prasai, B. A. Trump, G. G. Marcus, A. Akopyan, S. X. Huang, T. M. McQueen, and J. L. Cohn. "Ballistic magnon heat conduction and possible Poiseuille flow in the helimagnetic insulator Cu_2OSeO_3". In: *Phys. Rev. B* 95.22 (2017), p. 224407. DOI: 10.1103/PhysRevB.95.224407.

[29] G. R. Waitkins and C. W. Clark. "Selenium Dioxide: Preparation, Properties, and Use as Oxidizing Agent." In: *Chem. Rev.* 36.3 (1945), pp. 235–289. ISSN: 0009-2665. DOI: 10.1021/cr60115a001.

[30] K. Momma and F. Izumi. "VESTA 3 for three-dimensional visualization of crystal, volumetric and morphology data". en. In: *J. Appl. Crystallogr.* 44.6 (2011), pp. 1272–1276. ISSN: 0021-8898. DOI: 10.1107/S0021889811038970.

[31] W. Kaminsky. "WinXMorph: a computer program to draw crystal morphology, growth sectors and cross sections with export files in VRML V2.0 utf8-virtual reality format". en. In: *J. Appl. Crystallogr.* 38.3 (2005), pp. 566–567. ISSN: 0021-8898. DOI: 10.1107/S0021889805012148.

[32] S. Wilkins. "QLaue". In: *https://svn.code.sf.net/p/qlaue/code/trunk* ().

[33] Xiang-Yang Liu and P. Bennema. "Morphology of crystals: Internal and external controlling factors". In: *Phys. Rev. B* 49.2 (1994), pp. 765–775. DOI: 10.1103/PhysRevB.49.765.

[34] Georgios D Barmparis, Zbigniew Lodziana, Nuria Lopez, and Ioannis N Remediakis. "Nanoparticle shapes by using Wulff constructions and first-principles calculations". In: *Beilstein J Nanotechnol* 6 (2015), pp. 361–368. ISSN: 2190-4286. DOI: 10.3762/bjnano.6.35.

[35] Rachel Zucker, Dominique Chatain, Ulrich Dahmen, Serge Hagège, and W. Carter. "New software tools for the calculation and display of isolated and attached interfacial-energy minimizing particle shapes". In: *Journal of Materials Science* 47.24 (2012), pp. 8290–8302. ISSN: 00222461. DOI: 10.1007/s10853-012-6739-x.

[36] Y. R. Luo. *Comprehensive Handbook of Chemical Bond Energies*. Boca Raton, FL: CRC Press, 2007.

[37] Mazhar N. Ali, Jun Xiong, Steven Flynn, Jing Tao, Quinn D. Gibson, Leslie M. Schoop, Tian Liang, Neel Haldolaarachchige, Max Hirschberger, N. P. Ong, and R. J. Cava. "Large, non-saturating magnetoresistance in WTe_2". en. In: *Nature* 514.7521 (2014), pp. 205–208. ISSN: 0028-0836. DOI: 10.1038/nature13763.

[38] Yanpeng Qi, Pavel G. Naumov, Mazhar N. Ali, Catherine R. Rajamathi, Oleg Barkalov, Michael Hanfland, Shu-Chun Wu, Chandra Shekhar, Yan Sun, Vicky Süß, Marcus Schmidt, Eckhard Pippel, Peter Werner, Reinald Hillebrand, Tobias Förster, Erik Kampertt, Walter Schnelle, Stuart Parkin, R. J. Cava, Claudia Felser, Binghai Yan, and Sergiy A. Medvedev. "Superconductivity in Weyl Semimetal Candidate $MoTe_2$". In: *Nat. Commun.* 7 (2016), p. 11038. ISSN: 2041-1723. DOI: 10.1038/ncomms11038.

[39] Deepak Sapkota, Rupam Mukherjee, and David Mandrus. "Single Crystal Growth, Resistivity, and Electronic Structure of the Weyl Semimetals NbP and TaP". en. In: *Crystals* 6.12 (2016), p. 160. DOI: 10.3390/cryst6120160.

[40] V. Tsurkan, L. Prodan, V. Felea, I. Filippova, V. Kravtsov, A. Günther, S. Widmann, H.-A. Krug von Nidda, J. Deisenhofer, and A. Loidl. "Structure, magnetic susceptibility and specific heat of the spin-orbital-liquid candidate $FeSc_2S_4$: Influence of Fe off-stoichiometry". In: *arXiv:1704.05275 [cond-mat]* (2017).

[41] Y. Hara, K. Takase, A. Yamasaki, H. Sato, N. Miyakawa, N. Umeyama, and S. I. Ikeda. "Structural and physical properties of FeSe crystals fabricated by the chemical vapor transport method". In: *Physica C*. Proceedings of the 9th International Conference on Materials and Mechanisms of Superconductivity 470, Supplement 1 (2010), S313–S314. ISSN: 0921-4534. DOI: 10.1016/j.physc.2010.02.021.

[42] Yang-Yang Lv, Fan Zhang, Bin-Bin Zhang, Bin Pang, Shu-Hua Yao, Y. B. Chen, Liwang Ye, Jian Zhou, Shan-Tao Zhang, and Yan-Feng Chen. "Microstructure, growth mechanism and anisotropic resistivity of quasi-one-dimensional $ZrTe_5$ crystal". In: *J. of Cryst. Growth*. SI: CRYS_ECCG5 457 (2017), pp. 250–254. ISSN: 0022-0248. DOI: 10.1016/j.jcrysgro.2016.04.042.

Chapter 5

Conclusion and Outlook

The goal of this work was to understand more about the fundamental structural components that are necessary for a material to host superconductivity. While the search for new superconductors is still ongoing, three new quarternary oxides containing low-dimensional bismuth selenide strips were discovered. All three materials were shown to be small band gap semiconductors where the electronic properties are dependent on the composition, which varies from sample to sample due to the high vapor pressure of Se and the high synthesis temperature. In the case of $Sr_2O_2Bi_2Se_3$, some samples show temperature-dependent resistivity that is characteristic of an insulating material while others show more metallic character, suggesting that the material may have an insulator to metal transition at a certain composition.

Further studies on the electronic properties of the $A_2O_2B_2Se_3$ materials will focus on making samples with consistent composition, which may be possible using positive argon pressure in the synthesis tube or by adding excess Se, physically

separated from the reactants, to provide positive Se vapor pressure to counteract vaporization from the reactants. Once samples can be made consistent, then controlled doping can be used to control the size of the band gap. Since the measured gap for the materials is between 0.1 and 1 eV, and likely a little higher without intrinsic doping, they may be useful as photovoltaic materials. Samples of varying composition (mixing Sr/Ba, and Bi/Sb) will be made and their temperature-dependent resistivity will be measured, and promising samples (i.e. with band gap of around 1 eV and measurable resistivity from T = 2 to 300 K), will be measured using the photoconductivity instrument.

In terms of structure, the $A_2O_2B_2Se_3$ materials were shown to be one-dimensional structural analogues of the well-known bismuth sulfide (and more recently, bismuth selenide) superconductors. Other one-dimensional analogues, such as $BaFe_2S_3$ and $Sr_{0.4}Ca_{13.6}Cu_{24}O_{41.84}$, have been shown to superconduct under pressure [1, 2]. In both $BaFe_2S_3$ and $Sr_{0.4}Ca_{13.6}Cu_{24}O_{41.84}$, the magnetic structure of the normal state material may influence the transition to the superconducting state under pressure. However, the $A_2O_2B_2Se_3$ materials are all entirely non-magnetic. Whether they do or do not superconduct under the same conditions as the other analogue materials may be an important data point in the ever-growing database of knowledge regarding the poorly-understood relationship between structure and superconductivity.

In the quest to extend the measurement capabilities of the McQueen lab into the high pressure regime, an instrument, BNK3R, was built with the capability of measuring magnetic susceptibility of a sample inside a diamond anvil cell. So

far, measurements using BNK3R have been limited due to low signal-to-noise ratio. The immediate future of BNK3R lies in optimizing the instrument configuration and data collection program to make the most of the lock-in's signal filtering and low-voltage sensitivity. The first step to doing this is to counteract the arbitrary phase offset of the AC signal by adjusting the phase manually on the lock-in amplifier. A few brief experiments measuring a small Pb sample around the superconducting transition using a series of different frequencies should help to empirically determine what frequency gives the best resolution, since both inductive and capacitive reactance are frequency dependent. Finally, a new compensation coil set will be designed which has a much higher inductance and a variable capacitor will be added in series. Ability to tune the inductive and capacitive components independently will allow for better overall compensation of the imaginary component of the circuit's impedance.

With a few small adjustments to the wiring lay-out and practice with technique, the diamond anvil cell can also be modified to allow for electronic transport measurements. Combined with BNK3R, this would allow for a full suite of pressure- and temperature-dependent measurements including $\rho(T, P)$, magnetoresistance, Hall effect measurements, and AC M(T) and M(H). Once the instrument design has been, work begins on measuring the backlog of samples that show promise for superconductivity under pressure. At the top of the list are Weyl semimetal candidate $LaCuSb_2$, electron-doped quantum spin-liquid candidate $ZnLi_xCu_3(OH)_6Cl_2$, and cluster magnet Nb_3Cl_8.

Analysis of CVT-grown Cu_2OSeO_3 crystals using a Wulff construction revealed

information about the factors affecting the surface energy of crystallographic planes in Cu_2OSeO_3. The use of a seed crystal in the reaction vessel increased the mean crystal size by roughly a factor of two, in addition to improving purity. This added to the rare example of seeded-CVT in general and was the first example of the use of this powerful technique to grow crystals of a skyrmion material. Given the importance of surface effects as well as the need for smooth facets for deposition experiments common to the study of Cu_2OSeO_3 magnetic properties, the demonstration of the utility of seeded-CVT is likely to gain a much-needed foothold in the skyrmion community.

References

[1] Hiroki Takahashi, Akira Sugimoto, Yusuke Nambu, Touru Yamauchi, Yasuyuki Hirata, Takateru Kawakami, Maxim Avdeev, Kazuyuki Matsubayashi, Fei Du, Chizuru Kawashima, Hideto Soeda, Satoshi Nakano, Yoshiya Uwatoko, Yutaka Ueda, Taku J. Sato, and Kenya Ohgushi. "Pressure-induced superconductivity in the iron-based ladder material $BaFe_2S_3$". en. In: *Nat. Mater.* 14.10 (2015), pp. 1008–1012. ISSN: 1476-1122. DOI: 10.1038/nmat4351.

[2] Masatomo Uehara, Takashi Nagata, Jun Akimitsu, Hiroki Takahashi, Nobuo Môri, and Kyoichi Kinoshita. "Superconductivity in the Ladder Material $Sr_{0.4}Ca_{13.6}Cu_{24}O_{41.84}$". In: *J. Phys. Soc. Jpn.* 65.9 (1996), pp. 2764–2767. ISSN: 0031-9015. DOI: 10.1143/JPSJ.65.2764.

Appendix A

The following pages show the front panel and block diagram (as three separate panels) for the BNK3R Control program written in LabView.

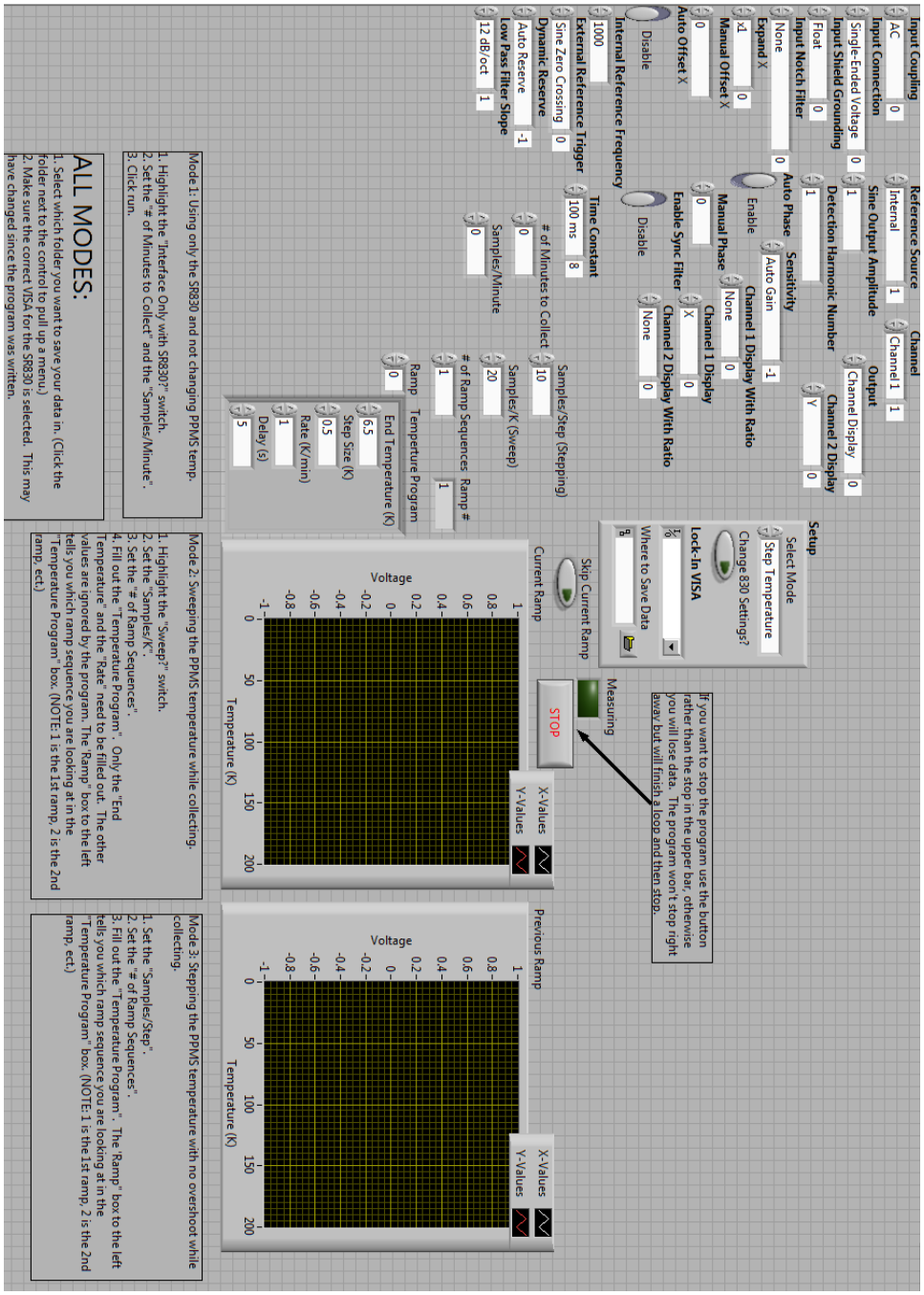

Figure 1: Program front panel

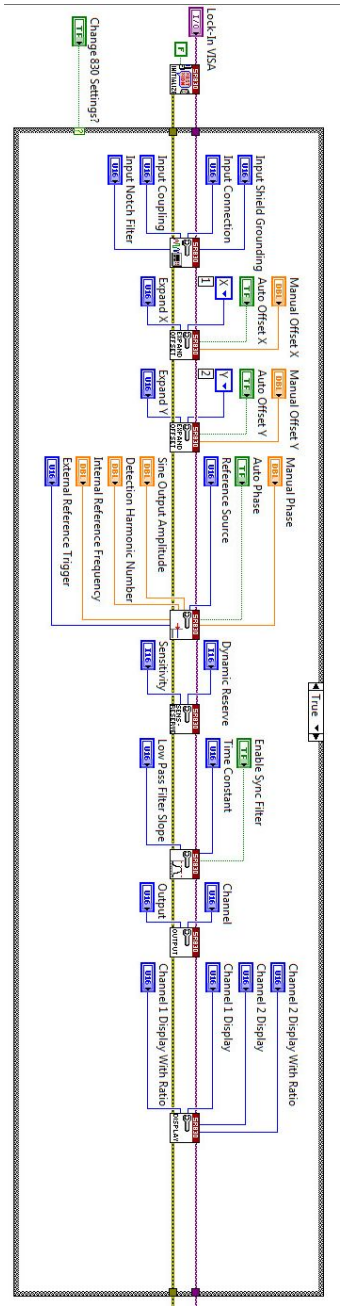

Figure 2: Block diagram Panel 1

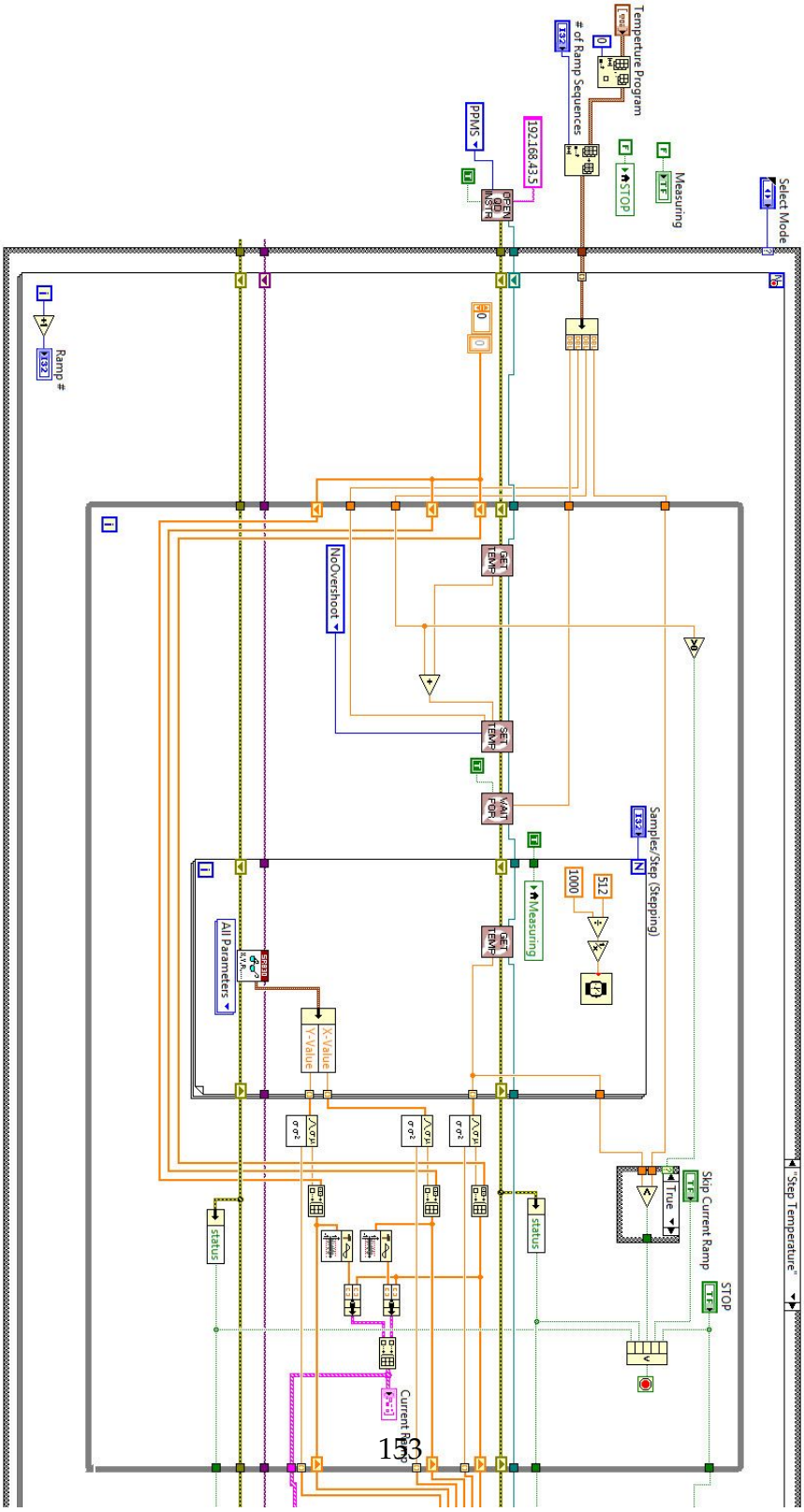

Figure 3: Block diagram Panel 2

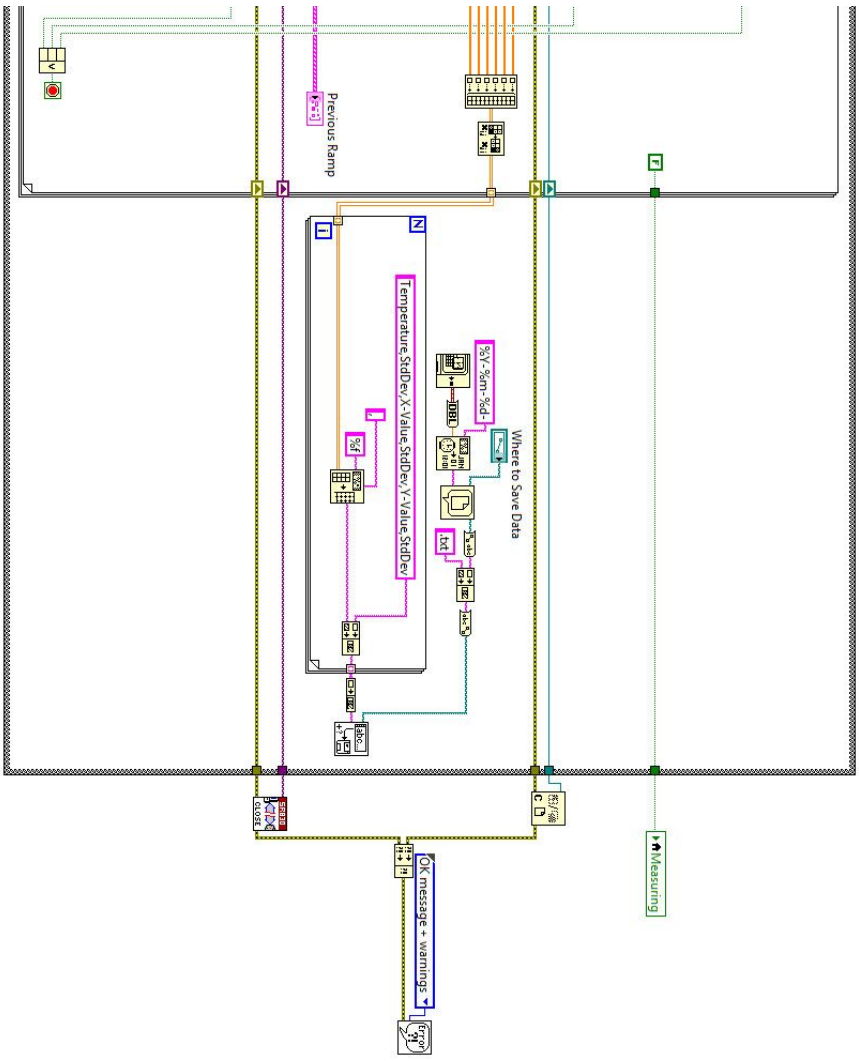

Figure 4: Block diagram Panel 3

Jessica Panella, Ph.D.

909 W University, Apt 105 (601) 463-0558
Baltimore, MD 21210 jpanella@jhu.edu

EDUCATION

Johns Hopkins University	**Ph.D.** Materials Chemistry	*Expected: Spring 2018*
Johns Hopkins University	**M.A.** Materials Chemistry	*Class of 2015*
The University of Southern Mississippi	**B.Sc.** Chemistry	*Class of 2013*

EXPERIENCE

McQueen Group Graduate Researcher Baltimore, MD
Johns Hopkins University *August 2013- Present*

- Developed advanced synthetic techniques to produce novel solid-state materials to elucidate structure-property relationships and exotic electronic behavior
- Designed new fitting for PPMS helium dewar port to recapture boil-off gas during procedural helium fills to dramatically reduce yearly helium loss
- Designed and rebuilt laboratory gas flow systems to accommodate a wide variety of reaction environments to adapt to rapidly changing research projects
- Served as "on call" primary for laboratory equipment, including vacuum pumps, two x-ray diffractometers, cryostat, helium reliquefier, and argon gloveboxes
- Highly proficient in materials characterization techniques: powder x-ray diffraction, AC magnetic susceptibility and DC magnetization, temperature dependent four-probe resistivity and thermal transport, and heat capacity
- Solved the structure of a new compound through the combined technique of simulated annealing and Rietveld refinement of x-ray diffraction data

Hopkins Extreme Materials Institute Graduate Researcher Baltimore, MD
Johns Hopkins University *August 2016- Present*

- Designed, built, demonstrated functionality of an instrument for measuring AC magnetic susceptibility inside of a diamond anvil pressure cell to measure magnetic properties at cryogenic temperatures under extreme pressure
- Designed and machined a tunable compensation coil mover to negate the large background from the excitation field and allow amplification of nanovolt scale signals
- Designed an effective system to isolate the sensitive external components of the susceptibility instrument from stray electronic noise while maintaining versatility to accommodate different experimental set-ups
- Systematically checked key parameters such as coil set resistances, signal shape and frequency, and cryostat pressure, to identify problems in the system, determine the causes, and implement corrections
- Analyzed cell components to determine the behavior of the cell during a pressure run to identify potential problems that could lead to future failure, such as asymmetric gasket stress or cracks in the anvils or seats, and take preventative action

AWARDS AND PROFESSIONAL ASSOCIATIONS

Hopkins Extreme Materials Institute Graduate Student	*2016*
Owen Award and Fellowship, JHU	*2013-2016*
Outstanding Senior Award - College of Science and Technology, USM	*2013*

PUBLICATIONS

J. Panella, B.A. Trump, G.G. Marcus, T.M. McQueen, "Seeded Chemical Vapor Transport Growth of Cu_2OSeO_3" *Cryst. Growth Des.* **17**, 4944-8 (2017).

T.T. Tran, **J. Panella**, J. Chamorro, J.R. Morey, T.M. McQueen, "Designing Indirect-Direct Bandgap Transitions in Double Perovskites" *Mater. Horiz.* **4**, 688-93 (2017).

J. Panella, J. Chamorro, T.M. McQueen, "Synthesis and Structure of Three New Oxychalcogenides: $A_2O_2Bi_2Se_3$ (A = Sr, Ba) and $Sr_2O_2Sb_2Se_3$" *Chem. Mater.* **28**, 890-5 (2016).